Design, Synthesis and Characterization of Biocompatible Quantum Dots for Application in Biophysics

Dissertation

zur Erlangung des akademischen Grades Dr. rer. nat.
der Fakultät für Naturwissenschaften
der Univertität Ulm

Vorgelegt von
Dipl.-Chem. Vladimir V. Breus
aus Kazan/Russland

January 2008

Contents

List of Figures

List of Abbreviations

General Abbreviations

LED	light-emitting diode
FRET	fluorescence resonance energy transfer
APD	avalanche photodiode
TIRFM	total internal reflection fluorescence microscopy
AFM	atomic force microscopy
FWHM	full width at half maximum
ML	monolayer
TEM	transmission electron microscopy
PCH	photon counting histogram

Chemicals

TOPO	trioctylphosphine oxide
HDA	hexadecylamine
TOP	trioctylphosphine
ODA	octadecylamine
ODE	1-octadecene
TDPA	tetradecylphosphonic acid
MPA	3-mercaptopropionic acid
EDC	1-ethyl-3-(3-dimethylaminopropyl) carbodiimide
OA	oleic acid
OLA	oleylamine
MUA	11-mercaptoundecanoic acid
TMAHP	tetramethylaminehydroxide pentahydrate
PVA	polyvinyl alcohol
PI	propidium iodide

Introduction

Quantum Dots

After the discovery of the first low-dimensional heterostructures with confinement of the charge carriers in one dimension, known as two-dimensional (2D) structures or quantum wells, in the 1970s [1], scientists began to search for the possibility of further reducing the confinement to two and eventually all three dimensions. This led to one-dimensional (1D) and zero-dimensional (0D) structures, also called quantum wires and quantum dots, respectively. In quantum dots, the confinement of electrical carriers in all three-dimensions results in atom-like discrete density of states; they were thus described as artificial atoms. This quantum confinement property made them very interesting for fundamental physical studies. In 1993, free-standing, colloidal semiconductor nanoparticles were synthesized for the first time [2], and showed the physical properties of quantum dots. Since then, the interest of both experimental and theoretical scientists to explore the potential technological applications quantum dots has intensively grown. Compared to fluorescent organic molecules, quantum dots are much more photostable and their absorption and emission energies are easily tuned by size which is, in turn, controlled during their synthesis. These advantages have evoked enormous interest among biophysicists and life-science researchers to use quantum dots as an alternative to organic dyes for a number of biological applications. In 1998 quantum dots were first successfully conjugated to a biomolecule while retaining the functionality of the latter and were internalized into live cells [3, 4].

Even though quantum dots have potential advantages over conventional organic dyes for applications in the life sciences, each of the established approaches towards obtaining water-solubilized quantum dots affects one or more of the essential constituents of biocompatibility, such as their small size and chemical stability. Moreover, the nonspecific interaction of quantum dots with proteins and cells, together with potential cytotoxicity effects complicates their use in biological applications [5, 6]. The reported fluorescence blinking behavior of quantum dots [7, 8, 9] could complicate their application in single-particle tracking experiments as well as other imaging applications. Therefore, the study and characterization of the key factors defining biocompatibility and the investigation of mechanism of the fluorescence blinking are important for the development of

new biocompatible coatings for nanoparticles and quantum dot bioconjugates.

Thesis Outline

The scope of this thesis is to characterize and understand the optical and chemical properties of different core-shell quantum dot preparations in terms of the effects of the shell and the ligand coating on the colloidal stability, absorption and photoluminescence spectra, quantum efficiency and fluorescence intermittency. On the basis of a good understanding of these properties, a new biocompatible ligand was developed to coat the particles, and the obtained functionalized quantum dots were characterized and optimized for fluorescence imaging applications.

This thesis consists of three major parts. Part I provides the necessary theoretical background on the structure, properties and synthesis of core-shell quantum dots, and gives a short overview of their applications in the life sciences.

Chapter 1 explains the basic principles of quantum dot fluorescence and gives a short overview of quantum dot structure.

Chapter 2 provides the necessary background on the synthesis of core quantum dots, explains the mechanism of nanoparticle growth and reviews several approaches to the synthesis of core/shell quantum dots.

Chapter 3 gives an introduction to the phenomenon of fluorescence intermittency in quantum dots and describes the variety of experimental data in literature.

Chapter 4 presents the main strategies towards the water-solubilization and functionalization of quantum dots, including the observations of fluorescence quenching induced by ligand exchange with thiolated molecules and the colloidal stability of aqueous quantum dot solutions.

Chapter 5 reviews the applications of quantum dots in life sciences, describes the main strategies for bioconjugation and characterizes the cytotoxicity of quantum dots.

Part II, **Chapter 6** provides a description of all experimental techniques used in the thesis for the synthesis and the characterization of quantum dots, and **Chapter 7** describes the fluorescence microscopy techniques used for single-molecule experiments.

Part III describes and discusses the experimental results.

Chapter 8 summarizes all the modifications made to the synthesis and capping procedures in order to optimize the properties of quantum dots and describes the effects of the various reaction conditions on the structure and properties of the resulting nanocrystals.

Chapter 9 contains an investigation of the effect of shell thickness on the fluorescence blinking of CdSe quantum dots. The mechanism of the observed behavior is described, and a microscopic explanation of the observed increase of quantum yield upon capping is given.

Chapter 10 presents an investigation of the conditions for and the kinetics of producing carboxylic acid-functionalized, water-soluble quantum dots and characterizes the fluorescence quenching properties observed upon using thiolated ligands for this functionalization. The photochemical stability of the carboxylated, water-soluble quantum dots is also discussed. Furthermore, it describes the surface exchange reaction with zwitterionic ligands used as an alternative to carboxylated ligands, comparing their properties in terms of colloidal stability and non-specific interaction with live cells.

Part I

Theoretical Basis

Chapter 1

Introduction to Quantum Dots

A quantum dot is a luminescent particle comparable in size with a 20 kDa protein. It is comprised of a 2 – 8 nm spherical crystalline core made from a direct-bandgap semiconductor material such as CdSe, CdTe or InAs (type I quantum dots) and an outer stabilizing layer of surfactants. A quantum dot possesses a much larger number of electrons in its valence band compared to the system of conjugated π-orbitals in a fluorescent organic dye. This electronic system increases the absorption cross section and the crystal structure makes quantum dots extremely stable against photobleaching ($>10^8$ emitted photons). For instance, an average CdSe nanocrystal is $\sim$20$\times$ brighter and 100$\times$ more photostable than the organic dye rhodamine [3].

1.1 Principles of Quantum Dot Fluorescence

1.1.1 Quantum Confinement

In contrast to a bulk semiconductor, the energy bands of a quantum dot can no longer be treated as continuous due to the effect of *quantum confinement*. The size of a quantum dot is smaller than the exciton Bohr diameter (the distance separating the excited electron and hole wavefunctions (exciton) of a bulk semiconductor). Therefore, the exciton is confined to a smaller size. As an effect, the band gap energy is higher than in the bulk material, and the continuous energy bands are split into discrete energy levels (Figure **1.1(A)**). These atomic-like energy levels of a quantum dot can be assigned in the absorption spectrum (Figure **1.1(B)**). The first absorption peak corresponds to the transition between the ground state and the lowest excited electron state, 1S(h) – 1S(e). Upon irradiation, the electron is excited to the 1S(e) state, leaving a hole in the valence band. Then the electron relaxes back down to valence band, recombines with the hole and emits a photon. Depending on the excitation energy, the electron can be excited to the lowest 1S(e) or to a higher state. Thus, a quantum dot can be

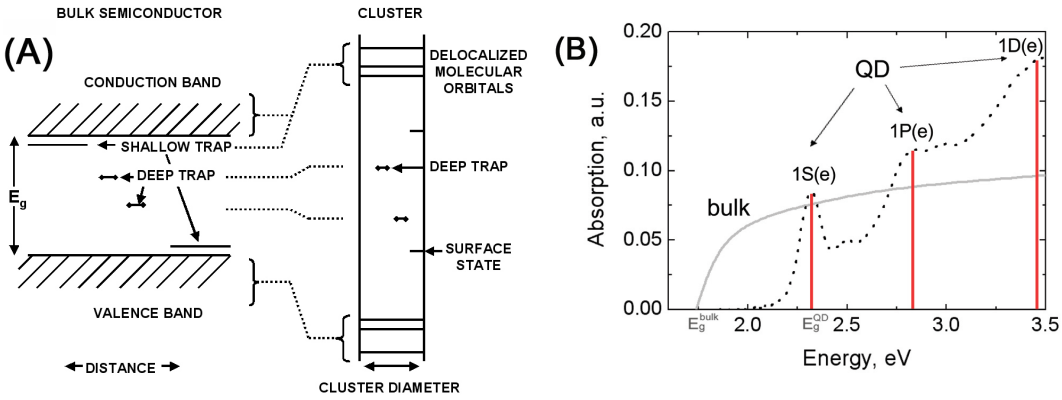

Figure 1.1: (A) Spatial electronic state correlation diagram for bulk semiconductors and semiconductor nanocrystals. Adapted from [10]. (B) Absorption spectra of CdSe quantum dots: a schematic representation of discrete atomic-like energy levels of a quantum dot (in red) and ensemble spectrum measured with a UV-Vis spectrometer (dotted line) in comparison with the continuous spectrum of bulk CdSe ($E_g^{bulk} = 1.74$ eV).

excited with energies higher than its first absorption peak. The small secondary peaks next to 1S, 1P, etc., in the absorption spectra (Figure **1.1(B)**, dotted line) are due to crystal field splitting and will be discussed later.

Transitions between excited electron states occur extremely fast, for example, electrons excited to 1P(e) will relax down to 1S(e) within 300 fs [11]. Similarly, the hole relaxes to the $1S_{3/2}$ state and, then, they recombine radiatively. Therefore, for a given quantum dot, the emission wavelength is independent of the excitation wavelength, and quantum dots have only a narrow peak in the emission spectrum (Figure **1.2(B)**), and several peaks in the absorption spectrum (Figure **1.2(A)**). The broad excitation range and narrow emission makes quantum dots a very attractive tool for multicolor imaging using a single illumination source.

Due to point defects inside the crystal and dangling bonds on the surface, some additional states may be present within the band gap of a semiconductor. These defect states are divided into *deep* and *shallow traps* (Figure **1.1(A)**). Deep traps are localized at a lattice site defect and appear in the middle of the band gap, as shown in Figure **1.1(A)** [10]. Shallow traps originate from surface defects and dangling bonds, can be delocalized over several unit cells and lie within a few millielectronvolts of the corresponding band edge (Figure **1.1(A)**) [10]. As nanocrystal size decreases, shallow traps will respond to small size before deep traps and shift to higher energy (Figure **1.1(A)**). When the crystal size becomes comparable to the radius at which the mobile charge orbits the trap, the distinction between shallow traps and the excitonic states ceases (Figure **1.1(A)**) [10]. Deep traps appear as a secondary de-focused peak in the

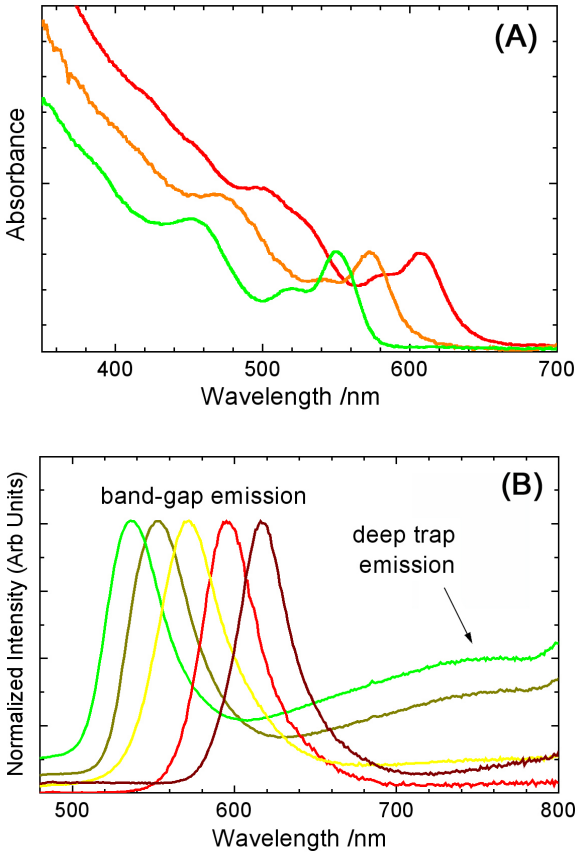

Figure 1.2: (A) Absorption and (B) emission spectra of CdSe quantum dots of different sizes.

emission spectrum of quantum dots (Figure **1.2(B)**), whereas the emission from shallow traps is difficult to distinguish from band gap emission.

1.1.2 Size-Dependent Optical Properties of Quantum Dots

Absorption and emission peak maxima of quantum dots are size-dependent (Figure **1.2(A,B)**). In a smaller quantum dot, the exciton is confined to a smaller size, which increases the energy of the first excitonic transition and results in higher absorption and emission energies. This effect makes it possible to obtain fluorescent markers with desirable optical properties. For instance, PbS quantum dots emit in the near-infrared [12], while GaN and ZnO nanoparticles are UV-fluorescent [13, 14]. For many applications, particularly in biophysics, the visible spectral range is preferred. By varying the size of CdSe quantum dots (from 1.6 to 6.8 nm), it is possible to tune the emission maximum over the whole visible range (Figure **1.3**).

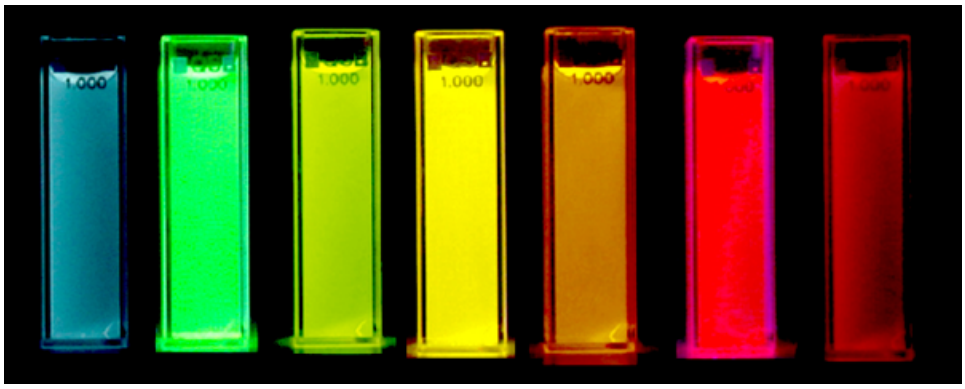

Figure 1.3: Photograph of toluene solutions of CdSe quantum dots of different sizes under excitation from a UV-lamp at 366 nm.

The *quantum yield* is a measure of the photoluminescence efficiency of a quantum dot. It is the ratio of the number of photons emitted to the number of photons absorbed by the nanoparticle. Quantum yields are usually measured in nano- or micromolar concentrated solutions and referred to as bulk quantum yields. To determine the absorption coefficient of a single particle is extremely difficult. Therefore, the single-particle quantum yield can only be estimated.

1.2 Structure of CdSe Quantum Dots

In general, a CdSe quantum dot can be presented as a structure of four distinct regions. The first region is the passivation layer, a monolayer of tightly packed organic amphiphile surfactants, such as the most widely-used trioctylphosphine oxide (TOPO) and hexadecylamine (HDA) (Figure **1.4(A)**). The second region is comprised of surface atoms either bound to the headgroup of the passivating surfactant or with unbound dangling bonds. The third region encompasses the top layer of nanocrystal, which is prone to reconstruction. Finally, the fourth region, the core of nanocrystal, is minimally affected by surface interactions and preserves the lattice structure of a bulk semiconductor crystal [15].

1.2.1 Crystallographic Characterization

Like the bulk material, CdSe nanocrystals can grow in both hexagonal (*wurtzite*) and cubic (*zinc blende*) symmetries. CdSe quantum dots prepared by pyrolysis using conventional stabilizers, such as TOPO and HDA (see Section **2.1**) display the wurtzite structure with a three-fold rotation axis $C_{3\nu}$ and are highly crystalline with less than one fault per crystallite [2, 17, 18] (Figure **1.5**). The combined analysis of high-resolution electron microscopy and resonance Raman spectroscopy data reveals that nanocrystals are faceted rather than purely spherical

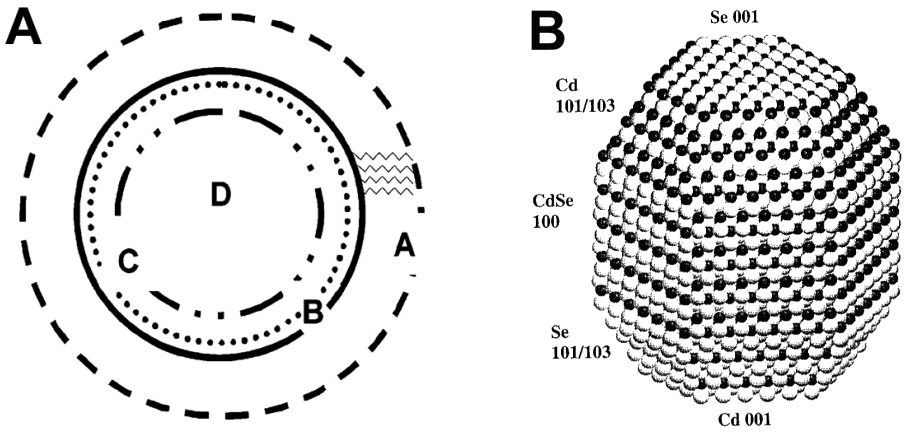

Figure 1.4: (A) *a* - Organic passivating layer. *b* - Cd or Se atoms at surface. *c* - Second layer from surface. *d* - Nanoparticle core in wurtzite symmetry. Reprinted from [15]. (B) Model of a stoichiometric, wurtzite CdSe nanocrystal obtained from an analysis of high resolution transmission electron microscopy images. Reprinted from [16].

[19] (Figure **1.4(B)**). When other techniques are used, for example microwave-assisted heating, quantum dots can also be obtained in zinc blende symmetry [20].

The absorbance spectra of wurtzite and zinc blende CdSe quantum dots (Figure **1.6**) have one distinctive feature contains additional secondary peaks, due to the effect of crystal field splitting as a result of crystal anisotropy [19].

1.2.2 Surface Characterization

For CdSe quantum dots stabilized only with TOPO, ∼70% of the nanocrystal surface is Cd, while 30% is Se, independently of the initial Cd to Se ratio in starting material [16]. This ratio can be explained by the superior passivating ability of TOPO for Cd atoms [16]. XPS surface analysis revealed that, on the surface of the nanocrystal, Cd atoms are coordinated to TOPO, while the majority of the Se surface atoms are unbound as prepared and can be oxidized upon exposure of quantum dots to air, forming a SeO_2 film, which leads to the aggregation of nanoparticles [21].

Quantum dots stabilized with both TOPO and HDA exhibit higher photoluminescence efficiencies in comparison with systems stabilized with TOPO only [17]. Such an effect was explained by the additional passivation of the quantum dot surface provided by alkylamines [17].

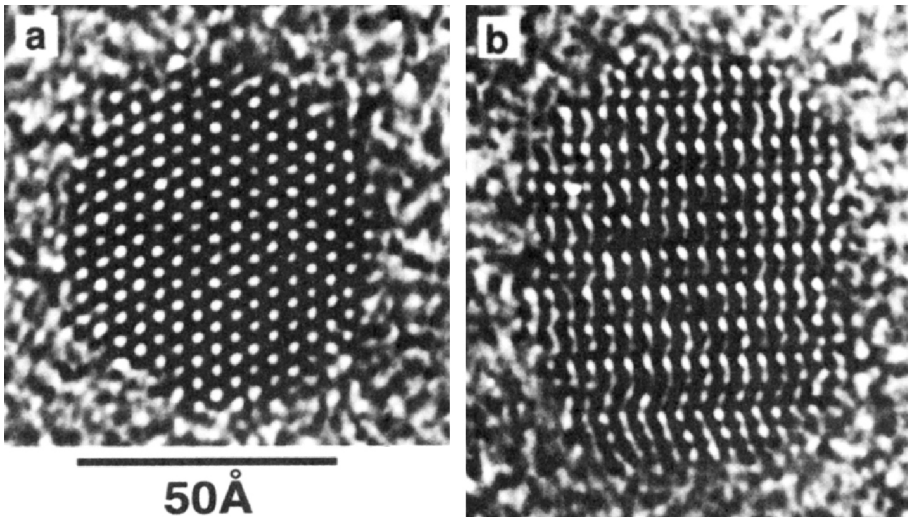

Figure 1.5: High resolution electron micrographs of CdSe nanocrystals viewed along the (A) [001] and (B) [010] zone axes. Reprinted from [19].

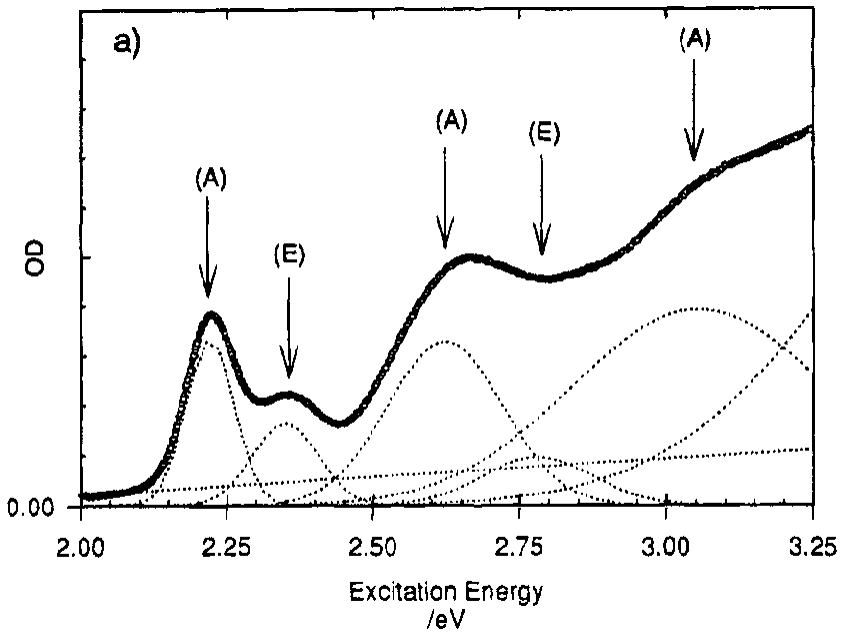

Figure 1.6: Absorption spectra of CdSe quantum dots grown in wurtzite symmetry. Reprinted from [19].

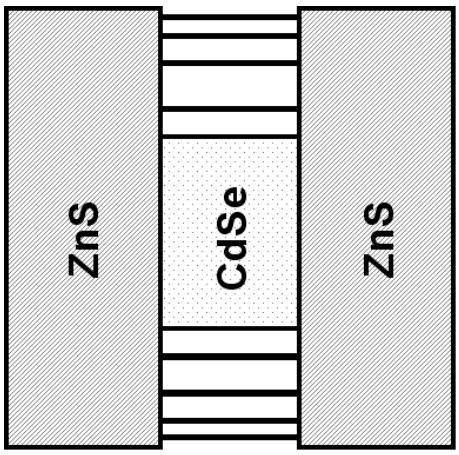

Figure 1.7: Band gap energy diagram of ZnS-capped CdSe quantum dots, $E_g^{CdSe} = 1.74$ eV, $E_g^{ZnS} = 3.66$ eV.

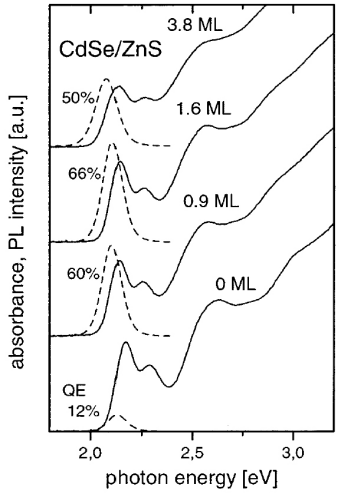

Figure 1.8: Absorption and emission spectra of CdSe nanocrystals before and after capping with ZnS shells of different thicknesses (in monolayers, ML). Reprinted from [17].

1.3 Core/Shell Quantum Dots

The quantum yield of a quantum dot is strongly dependent on the presence of defects in the crystalline core and dangling bonds on the surface of nanoparticle [22, 23]. These conditions induce non-radiative recombination of electron and hole, so that emission does not occur. In order to suppress such effects and increase the photoluminescence efficiency, quantum dots can be overcoated with another semiconductor material with higher band gap energy, which confines the electron and hole wavefunctions away from the surface, thereby increasing the radiative recombination and thus the quantum yield [24, 25]. For instance, capping with ZnS is able to increase the quantum yield of CdSe nanocrystals from 10 – 20% up to 60 – 70% (Figure **1.7**) [26]. Upon capping, the quantum yield increases up to a critical number of monolayers and then starts to decrease (Figure **1.8**) [26]. As the shell thickness approaches the core size, the core lattice no longer templates the growth of the shell, and the shell lattice dominates over the core, causing lattice strain and increasing the number of possible defects on the core/shell boundary and inside the shell. Figure **1.8** illustrates the shift of the absorption and emission spectra to lower energies upon capping. This shift has been observed for different core/shell materials. It is explained by a partial tunnelling of the electron wavefunction of the core into the shell [25].

Another function of the shell is to enable subsequent chemical modification (e.g., for solubilization or conjugation with biomolecules) without affecting the optical properties of the core.

Chapter 2

Synthesis of Quantum Dots

2.1 CdSe Quantum Dots: Evolution of Organometallic Synthesis

Among all luminescent semiconductor nanoparticles, CdSe is one of the most studied and widely-used materials for quantum dots. The main advantages of CdSe quantum dots are their ease of fabrication and their variable optical properties, as they are tunable over the whole visible range, which is preferable for many applications. For the preparation of CdSe nanoparticles, the original high-temperature organometallic synthesis, first developed by *Murray* and *Bawendi* in 1993 [2], remains the most common technique. This reproducible method, following a few minor improvements [17, 26] allows one to obtain quantum dots with photoluminescent efficiencies of 10 – 30% and size dispersion of about 5 – 10% [27]. Nucleation occurs at temperatures around 280 – 300°C upon fast injection of selenium into a solution of cadmium, which is stabilized by surfactants in reverse micelles. Originally, TOPO was used as the stabilizer for cadmium and trioctylphosphine (TOP) for selenium precursors [2]. Later it was found that the use of HDA as an additional coordinational component improves the quantum yield and size distribution of CdSe nanoparticles [17]. In more recent studies, HDA was replaced with octadecylamine (ODA), and the reaction system was completed with the addition of non-coordinating, non-polar low volatility solvent 1-octadecene (ODE) [28].

A few cadmium precursors, alternative to the dimethyl cadmium introduced by *Murray* and *Bawendi* [2], have been used since. It was shown that dimethyl cadmium in TOPO can decompose at high temperature generating insoluble metallic precipitate. It was thus suggested to use cadmium oxide complexed with tetradecylphosphonic acid (TDPA) instead [30].

Other synthesis improvements developed to suppress environmental factors such as the addition of the dehydrating agent anhydrous triethylorthoformate [31] or degassing of the reaction mixture [30] were also found to slightly increase

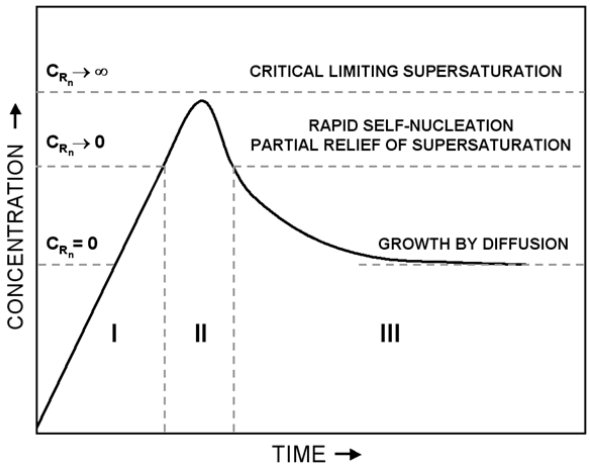

Figure 2.1: Schematic representation of the concentration of molecularly dissolved sulfur before and after nucleation as a function of time. Adapted from [29].

the quantum yield of CdSe nanoparticles.

2.2 Mechanism of Crystallization of CdSe Quantum Dots

There are two major stages of the formation of monodisperse colloids according to studies by *La Mer* and *Dinegar*: a) fast discrete nucleation and b) slower, controlled growth of nuclei into crystals [29]. Their theory was explained on the basis of the preparation of a monodisperse sulfur hydrosol by slow decomposition of dilute sodium thiosulfate in dilute hydrochloric acid. The reaction yields a molecularly dissolved sulfur. The colloids formation is schematically depicted in Figure **2.1**. The concentration of sulfur increases during stage I, up to a critical concentration at which self-nucleation occurs producing droplets of supercooled liquid lambda sulfur. During stage II, the presence of nuclei in the system partially relieves supersaturation and the rate of nucleation drops almost immediately to zero (Figure **2.1**). At nucleation rate $R_n \approx 0$, molecular sulfur is still present in solution and, therefore, further growth of the existing nuclei is possible by diffusion of sulfur to the formed nuclei, stage III (Figure **2.1**). Supersaturation can also be achieved by varying different parameters such as solubility, temperature, etc. [29].

In the case of quantum dots, stage II is extremely narrow (Figure **2.2**) [32]. At high temperature, rapid injection of selenium partially relieves the cadmium supersaturation and the nuclei form extremely quickly. If no further precursors are added to the system, no further nucleation occurs and the particles grow from the existing nuclei (Figure **2.2**) [32]. Therefore, the initial size distribution

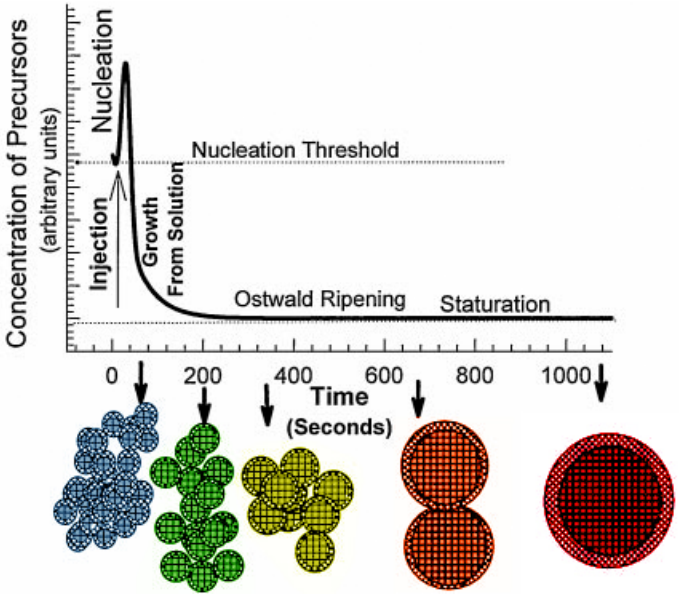

Figure 2.2: Cartoon depicting the stages of nucleation and growth for the preparation of monodisperse nanocrystals in the framework of the La Mer model. As nanocrystals grow with time, a size series of nanocrystals may be isolated by periodically removing aliquots from the reaction vessel. Adapted from [32].

is determined by the time of the nucleation stage, i.e., the injection rate of Se.

Many systems exhibit a second growth phase, in which small particles can be recomposed into larger structures, in order to compensate for their high surface energy [34, 35]. This process, *Ostwald ripening*, can be used as an efficient method for the preparation of quantum dots of larger sizes (Figure **2.2**).

In order to further characterize the mechanism of quantum dots temporal evolution during synthesis, the nucleation and growth of CdSe nanocrystals were studied in situ by recording the absorption spectra during the reaction within millisecond resolution [33]. Quantum dots were synthesized from cadmium oxide in TOPO/HDA mixture by injection of the TOP-Se complex at 280°C as described above. For this specific reaction, shown in Figure **2.3** (left), 4 ms were enough for the formation of a small amount of particles with diameters of 1.75 nm [33]. After 2 more seconds, new nuclei ceased to appear and the subsequent growth of nanoparticles was possible only from the ones that had already formed and free precursors in solution (Figure **2.3** (middle - upper graph inset)). In the following 130 s the amount of particles as well as the concentration of free cadmium precursor decreased (Figure **2.3** (middle)). Between 130 and 670 s (Figure **2.3** (middle)), a stationary phase was observed, during which the number of particles, concentration of free cadmium and size remained constant. Overall, the observations demonstrated four major stages of the entire crystallization process: 1 - *Initial stage*, equivalent to the nucleation stage in the classical study, where

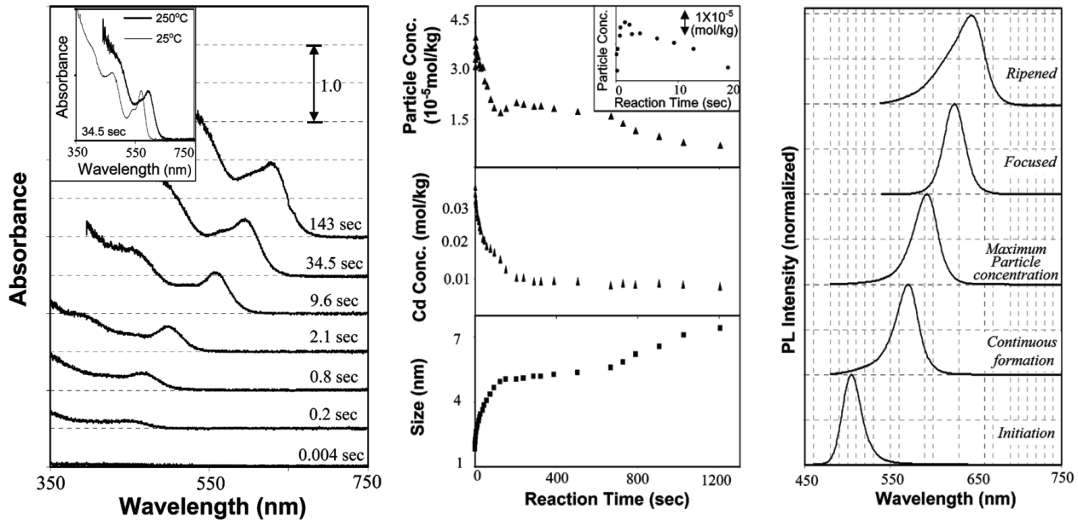

Figure 2.3: (Left) In situ recorded UV-vis absorption spectra of CdSe nanocrystals at 250^{o}C. A comparison of absorption spectra at different temperatures is shown on the inset; (Middle) Temporal evolution of the size and concentration of the CdSe nanocrystals, and the concentration of cadmium monomers in the solution for the reaction shown on the left Figure; (Right) Temporal evolution of the PL spectrum of the nanocrystals for the same reaction. Reprinted from [33].

small nuclei are formed in solution; 2 - *Focusing of the size distribution*, where the emission peak reverts to a symmetric shape while the concentration of particles drops significantly (Figure **2.3** (middle and right)); 3 - *Stable stage*; and 4 - *Ostwald ripening*, where defocusing of the size distribution is observed (Figure **2.3** (right)).

2.3 Alternative CdSe Synthesis Techniques

Apart from the high-temperature organometallic synthesis, other methods were developed for the preparation of CdSe quantum dots, including slow room-temperature synthesis [36], photo-assisted synthesis of CdSe from cadmium nitrate and 1,1-dimethylselenourea precursors under illumination for up to 3 h using a pulsed Nd:YAG laser at 532 nm [37], synthesis of very small CdSe quantum dots (1.4 - 2.2 nm in diameter) in aqueous solutions using mercaptoalcohols and mercaptoacids as stabilizers [38], and facile sonochemical synthesis of CdSe quantum dots and capping with ZnS by sonication at room temperature [39].

From the variety of described synthesis techniques for quantum dots, high temperature organometallic synthesis is considered to be most reproducible and efficient method to obtain highly luminescent, monodisperse quantum dots.

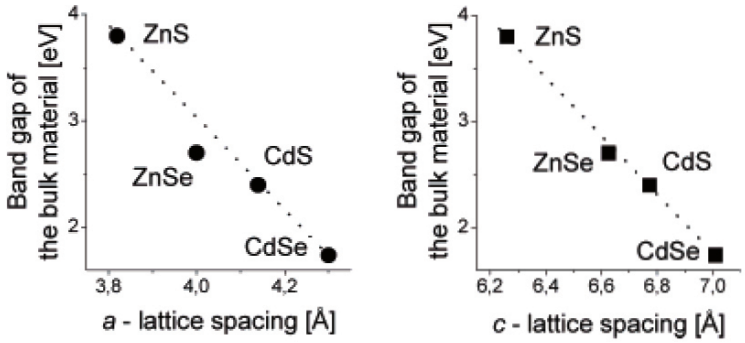

Figure 2.4: Relationship between band gap energy and lattice parameter of bulk wurtzite phase CdSe, ZnSe, CdS and ZnS. Reprinted from [40].

2.4 Core/Shell Quantum Dots

The choice of shell material is usually based on two main criteria - a larger band gap and similar lattice parameters. CdS, ZnSe and ZnS are the most common capping materials for CdSe quantum dots. The relation between band gap energy and lattice constants of each shell material compared to CdSe is shown in Figure **2.4** [40]. Because of similar lattice constants, CdS should produce less lattice defects and mismatches in the shell, however, the band gap energy of ZnS is significantly higher than that of CdS and ZnSe (Figure **2.4**), which provides more efficient confinement of electron and hole wavefunctions inside the nanocrystal and therefore increases the photoluminescence efficiency of ZnS-capped CdSe quantum dots [40].

2.4.1 Traditional Capping Method

The traditional capping method was developed by *Hines et al.* in 1996 using dimethyl zinc and hexamethyldisilathiane in trioctylphosphine solution to grow a ZnS shell on CdSe quantum dots [26]. The mixed solution of zinc and sulfur ions in trioctylphosphine was added in a few portions to the reaction mixture containing CdSe quantum dots in trioctylphosphine at 300°C [26]. It was later modified by using additional amine surfactants for both synthesis of CdSe and the capping with ZnS at 220°C [17]. The temperature of injection of zinc and sulfur ions was also considered to be critical for the formation of individual ZnS particles and alloys [17].

2.4.2 Alternative Capping Method: SILAR

In addition to the traditional method, a new technique was recently introduced to cap CdSe quantum dots termed *Successive ion layer adsorption and reaction* (*SILAR*) [28]. It allows one to grow the shell a single monolayer at a time by

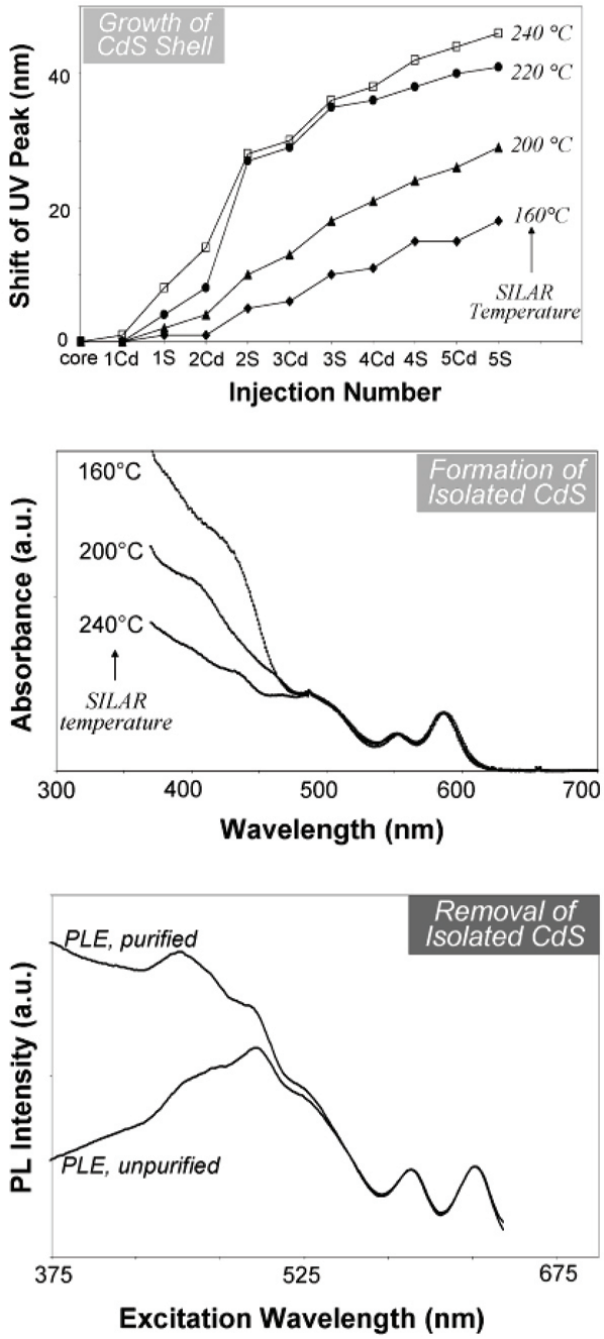

Figure 2.5: (Top) The red-shift of the first absorption peak of CdSe quantum dots upon growth of a CdS shell after each injection is plotted for different reaction temperatures; (middle) formation of individual CdS particles at lower temperatures; (bottom) photoluminescence excitation spectra (monitored at 650 nm) of CdSe/CdS nanocrystals before and after the removal of individual CdS particles. Reprinted from [28].

separate injections of the shell components one after another [28]. This procedure enables more controlled shell growth with the size distribution of nanoparticles maintained even after capping with five monolayers of CdS [28].

The SILAR synthesis for CdSe/CdS, described by *Li et al.*, was carried out in a carefully degassed octadecylamine-octadecene mixture without the traditionally used trioctylphosphine oxide [28]. The reaction temperature played a critical role for the proper shell growth. Figure **2.5** shows that the CdS shell growth on CdSe nanoparticles occurred more effectively at higher temperatures, which can be concluded from the larger peak shift in the adsorption spectrum upon capping. The use of lower temperatures (from 160 to 220°C) in this system leads to the formation of individual CdS particles, which can be assigned by the increase in the absorption at 300 – 400 nm (Figure **2.5**). However, at temperatures above 260°C it was difficult to prevent Ostwald ripening of the capped quantum dots [28].

Chapter 3

Fluorescence Intermittency of Quantum Dots

For individual light-emitting entities, whether these are organic dye molecules [41], fluorescent protein molecules [42, 43] or nanoparticles [44, 7], an interesting phenomenon is observed, which is completely obscured in ensemble measurements, *fluorescent intermittency*, also called *flickering* or *blinking*. The exact mechanism of blinking varies from species to species but, in general, involves transitions to non-emissive, metastable states (Figure **3.1(A)**). Blinking of quantum dots restricts some of their applications as devices in nanotechnology or in the life sciences. To devise strategies to minimize or even suppress blinking completely, it is important that its physical mechanism be well understood.

3.1 Studies of the Blinking Phenomenon

3.1.1 "*on*"and "*off*" states

Blinking can be conveniently studied by recording a fluorescence emission time trajectory, i.e., the emission intensity of single, immobilized quantum dots, as a function of time (Figure **3.1(B)**). An intensity threshold is set to determine the periods in which the quantum dots are in their "*on*" and "*off*" states. From these data, distributions of time periods spent in either of the two states are calculated for a particular quantum dot ensemble. It has been suggested that an "*off*" state is transiently created if electron is ejected from the particle, leaving behind a charged quantum dot [9]. Any excitons formed during this time recombine by a irradiative Auger process, which has a lifetime of 1 – 100 ps, which strongly depends on the quantum dot size [45], compared to the ∼10 ns radiative lifetime. Measurements of quantum dot charging upon laser illumination were reported by *Krauss* and *Brus* using electrostatic force microscopy [46, 47]. The "*off*" to "*on*" transition was also found to be accompanied by spectral diffusion of the quantum

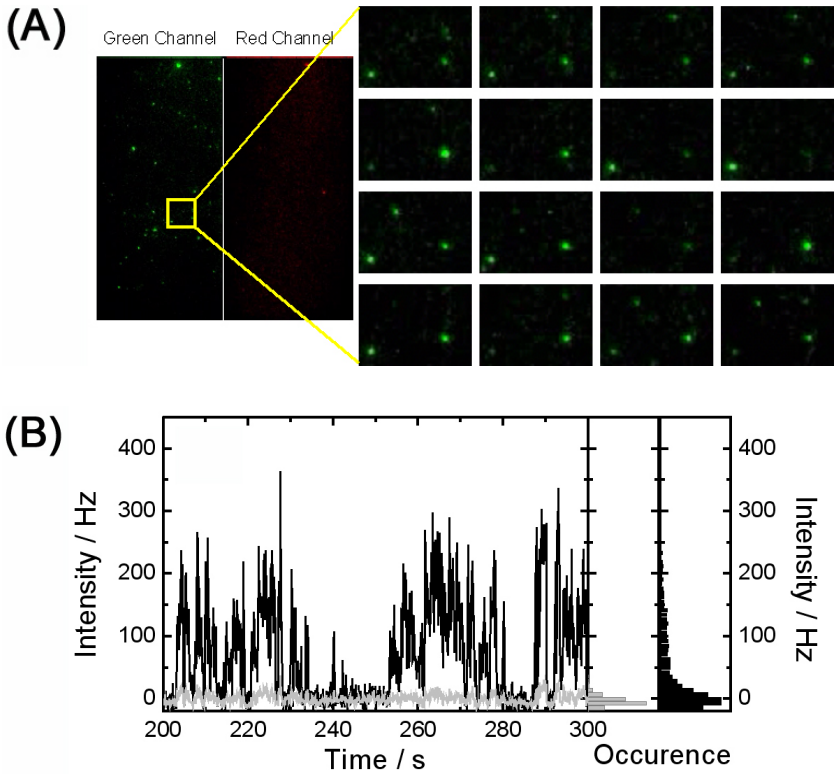

Figure 3.1: (A) 16 consecutive frames from the blinking obtained from the movie recorded by TIRFM. (B) *Black* - typical fluorescence time trajectory of a single quantum dot with 100 ms binning. *Grey* - local background calculated from a set of pixels immediately surrounding the single quantum dot spot.

dot emission due to a redistribution of the local electric field following blinking [48].

3.1.2 Mechanism of Blinking: Proposed Models

The shapes of the probability distribution functions of "*on*" and "*off*" times have become a source of much debate in recent years. Various models have been proposed to explain them. The initial theory of photo-ionization leading to the dark state predicted exponential probability densities for the duration of both "*on*" and "*off*" times [9]. However, for the "*off*" times, power-law dependencies have been reported, extending over several orders of magnitude in time (Figure **3.2(C,D)**) [7, 44, 49, 50, 51]. These observations were explained by an ensemble of trap states with wide distributions in energy and distance. For the probability densities of "*on*" times, the experimental findings have been conflicting. Power-law behavior has been observed by some [51, 8], others report power-law behavior with a cutoff tail at long times, as shown in Figure **3.2(A,B)** [7], whereas *Verberk*

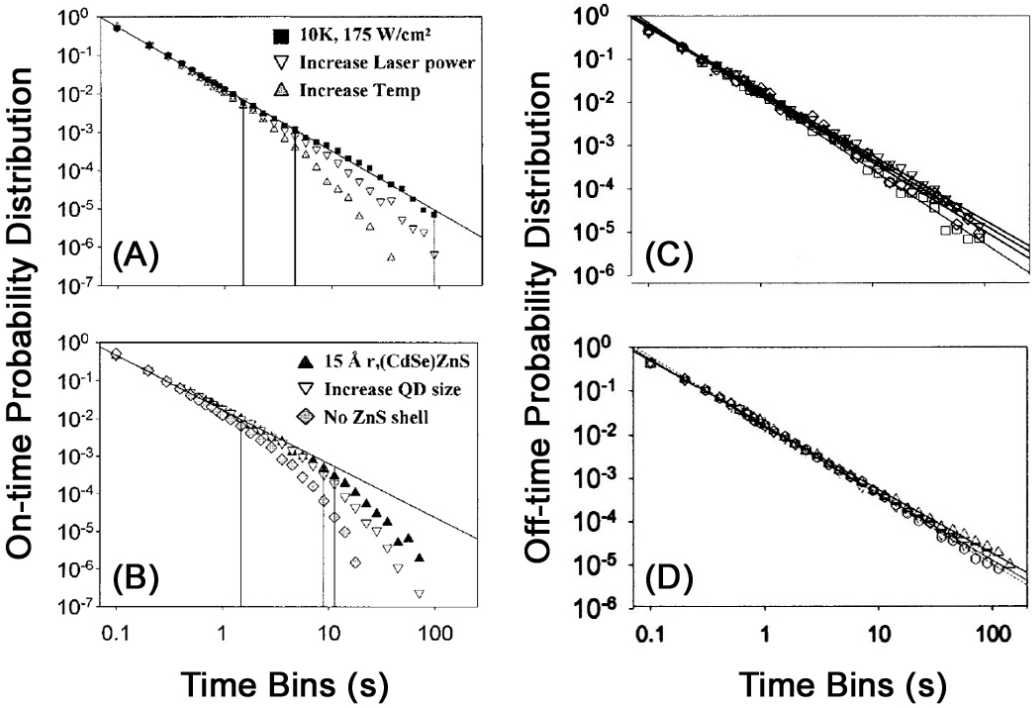

Figure 3.2: (A) Average *"on"*-time probability distribution for 25-Å radius CdSe(ZnS) quantum dot at 300 K and 175 W/cm^2 (▲), 10 K and 700 W/cm^2 (▽), and 10 K and 175 W/cm^2 (■). The straight line is a best-fit line with exponent ∼1.6. (B) Average *"on"*-time probability distribution for 15-Å radius CdSe(ZnS) quantum dot (▲) and 25-Å radius CdSe(ZnS) quantum dot (▽) and 25-Å radius CdSe quantum dot (◆) at RT, 100 W/cm^2. The vertical lines correspond to truncation points where the power-law behavior is estimated to end. (C) Average *"off"*-time probability distribution for 25-Å radius CdSe(ZnS) quantum dot at 300 K (▽), 10 K (△), 30 K (◇), and 70 K (□). The α values are 1.41, 1.51, 1.37, and 1.45, respectively. (D) Average *"off"*-time probability distributions for CdSe(ZnS) quantum dot of radius 15 Å, (▽) and 25-Å radius CdSe(ZnS) quantum dot (◇) and 25-Å radius CdSe quantum dot (△) at RT. The α values are 1.54, 1.59, and 1.47, respectively. Reprinted from [7].

et al. [52] have observed a single-exponential distribution for uncapped CdS quantum dots and a power law for capped CdS quantum dots. *Verberk et al.* [52] postulated that three states are present for the capped CdS, *(i)* the normal emitting state, *(ii)* a positively charged particle state in which the electron has been ejected from the particle into an external trap, leaving the hole to quench any emission by Auger processes (charged and non-emitting), and *(iii)* a state in which the electron remains ejected, but the hole is localized in an internal trap at the surface of the shell (charged but emitting). It was argued that Coulomb blockade effects would prevent further electron ejection, thereby causing long

"*on*" times.

More recently, *Zhang et al.* [53] analyzed fluorescence time traces of streptavidin-coated commercial CdSe-ZnS quantum dots and reported a continuous distribution of emissive states of different intensity and fluorescence lifetime. *Pelton et al.* [54] observed that the power spectral density of quantum dot blinking is identical whether in solution or immobilized on glass slides, suggesting that the blinking mechanism is not sensitive to the environment. This result sheds doubt on models that involve trapping of electrons in structurally and energetically heterogeneous external states in the vicinity of the quantum dot.

At the same time, a theoretical model, in which the trap states rendering the quantum dot to an "*off*" state reside only in the core and shell [55], was shown to be able to adequately fit the experimental data of *Shimizu et al* [7]. A surface-trapping model was also reported by *Tang* and *Marcus* [56], and recently, *Frantsuzov* and *Marcus* [57] presented a mechanism for quantum dot blinking that does not involve long-lived electron traps, but rather hole trapping in surface states, accompanied by electron excitation within the conduction band by an Auger mechanism.

Chapter 4

Functionalization of Quantum Dots

Following the various developed techniques described in Chapter **2** it is now relatively easy to synthesize high-quality colloidal quantum dots in organic solvents with quantum yields between 20 and 50% or even higher [17, 58, 22]. For applications in the life sciences, quantum dots have to be transferred to aqueous media, but methods to render them water-soluble are much less established and are often irreproducible. It is also important to achieve biocompatibility of the quantum dot surface, resistant to non-specific interaction with biological objects. In 1998, water-solubilization was first achieved and quantum dots were conjugated to proteins [4, 3]. Since then, a broad variety of methods have been proposed to produce water-soluble quantum dots. However, a universal approach that would match all the criteria for application of quantum dots in the life sciences, i.e., excellent optical properties, small size, chemical stability and biocompatibility, has not yet been found.

4.1 Types of Functionalization

There are two main strategies towards water-solubilization of quantum dots. The first approach is encapsulation of quantum dots inside amphiphilic polymers [59], organic dendrons [60] or phospholipid micelles [61], preserving their initial hydrophobic surfactants. Another method is to change the ligand environment around the nanoparticles by replacement of the initial hydrophobic surfactants in which they are synthesized with various mono- and bifunctional molecules such as mercaptoacids [62, 4, 5, 63, 30], water-soluble phosphine oxide ligands [64], pyridine [65] or mercaptopropyltris(methyloxy)silane, with subsequent silanization of the quantum dot surface [66]. In each case one or more of the following properties are affected: total size of the nanoparticle, photoluminescence efficiency, chemical and photochemical stability. In general, silanization and polymer encapsulation

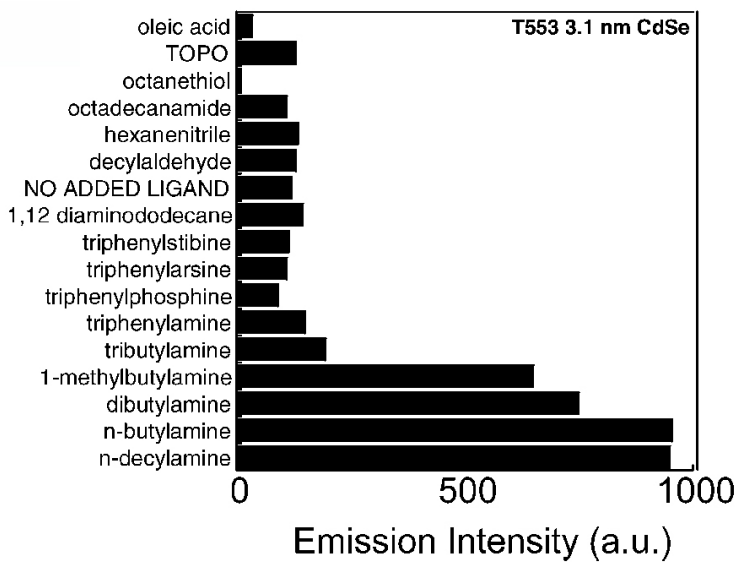

Figure 4.1: Fluorescence intensities of 3.1 nm CdSe nanocrystals in chloroform 22 h after addition of 5 mM of various ligands. [CdSe] = 1 μM, excitation wavelength was 450 nm. Reprinted from [67].

provide stability and preserve the initial quantum yield at the expense of total quantum dot size. Mercaptoalkylacids maintain a small total size of the nanoparticle, which is an extremely important parameter for many biological applications, usually decreasing the quantum yield and chemical stability. However, they also offer the advantage of relative ease of preparation using commercially available, inexpensive reagents.

4.2 Fluorescence Quenching of Quantum Dots

A large number of compounds and functional groups can interfere with the emission of quantum dots, inhibiting it or reducing its intensity by various non-radiative pathways. It has been reported that the addition of octanethiol, triphenylphosphine, triphenylarsine and oleic acid to TOPO/HDA-coated CdSe quantum dots dramatically reduced the emission intensity of the nanoparticles, whereas treatment of the same nanoparticle preparation with different alkylamines increased the photoluminescent efficiency (Figure **4.1**) [67]. This quenching effect is especially important since many ligands used to render quantum dots water-soluble contain thiol, carboxylic or phenyl groups.

4.2.1 Mechanisms of Quenching

Depending on the mechanism, quenching can be divided into two types: *static* and *dynamic*. Static quenching occurs by formation of a stable complex between fluorophore and quencher. Dynamic quenching does not assume complex formation and, therefore, is determined by the diffusion of quencher and fluorophore. Fluorescence quenching is usually described by the *Stern-Volmer* equation [68]:

$$\frac{I_0}{I} = 1 + K_{SV}[Q] \tag{4.1}$$

where I_0 is the fluorescence intensity without quencher, I is the fluorescence intensity with quencher, K_{SV} is the Stern-Volmer coefficient and $[Q]$ is the concentration of the quencher. This model describes a linear dependence of I_0/I on $[Q]$ due to the presence of a single quenching pathway. If multiple quenching sites are present, the dependence of I_0/I on $[Q]$ is given by [68]:

$$I_0/I = \Big[\sum_{i=0}^{n} \frac{f_i}{(1 + K_{SVi}[Q])}\Big]^{-1}. \tag{4.2}$$

Here, f_i is the fractional contribution of the i^{th} pathway to the total fluorescence. K_{SVi} is the Stern-Volmer coefficient for a given quenching pathway.

4.2.2 Thiol Quenchers

It has often been reported that ligand exchange of CdSe and CdSe/ZnS quantum dots with thiolated compounds results in a reduction of the quantum yield [3, 62, 69]. Thiol groups function as hole acceptor, inhibiting radiative recombination, upon approach to the surface of a quantum dot. For quantum dots, the detailed mechanism of thiol quenching has not yet been thoroughly studied. In fact, it is not clearly established which factors define the rate of quenching or which thiolated molecules are stronger quenchers.

4.3 Functionalization of Quantum Dots with Thiolated Ligands

The easiest, cheapest and probably the most widely used ligands to prepare water-soluble, biocompatible quantum dots are mercaptoalkyl acids [3, 69, 62]. The thiol moiety binds to the surface of a quantum dot, replacing the initial TOPO (bound via a phosphine oxide group) and HDA (bound via an amine group) ligands. When deprotonated, the carboxylate groups on the outside of the quantum dots renders the quantum dot water-soluble.

The extent of ligand exchange depends largely on the reaction conditions, time of exchange and surface chemistry. *Kuno et al.* showed that overnight exchange

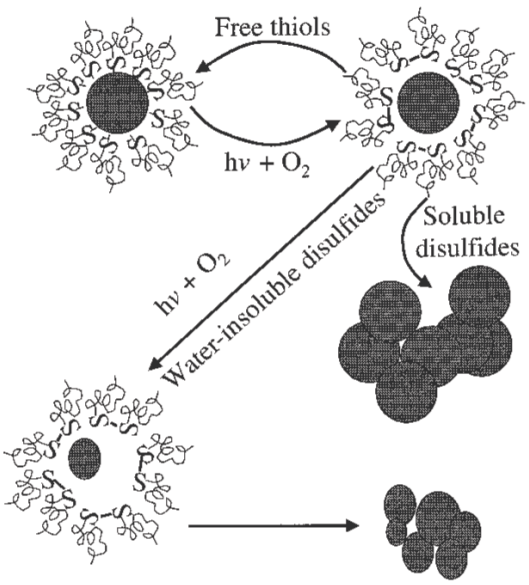

Figure 4.2: Mechanisms for the photochemical instability of thiol-coated CdSe nanocrystals. Reprinted from ref [62].

of TOP/TOPO-stabilized CdSe quantum dots with organic thiols in pure ligand solutions without additional solvent, left about 9-10% of TOPO on the surface [65]. For the functionalization of identically prepared CdSe quantum dots with 11-mercaptoundecanoic acid, overnight stirring in methanol at 65°C under argon flow is reported to provide complete replacement of the initial surfactants [62]. Surface exchange of CdSe quantum dots, initially stabilized by hexadecylamine (HDA), with 2,4-difluorothiophenol completely replaced HDA even after 5-10 min at 60°C [15]. The observed effect can be explained by the higher surface passivation ability of TOPO, compared to HDA [16].

4.4 Chemical Stability of Thiol-Coated Quantum Dots

Another important constituent of biocompatibility is the chemical stability of the functionalized quantum dots. Under the influence of external conditions, the ligands can be desorbed from the surface of quantum dots causing their aggregation. Ligand exchange with thiolalkyl acids normally provides sufficient solubility of quantum dots in aqueous solutions, but may, however, become unstable over time [62, 22].

Aldana et al. [62] have found that 2-mercaptopropionic acid (MPA) bound to the quantum dot surface undergoes photocatalytic oxidation upon long exposure to light and forms intermolecular disulfide bonds, promoting aggregation of

quantum dots [62]. It was proposed that the formation of disulfide bonds between two adjacent thiolated ligands on the surface of the quantum dot was initiated by the photogenerated holes in a nanocrystal becoming trapped on the thiol groups bound to their surface [62]. The resulting disulfides can drift away from the surface if they are soluble in aqueous media, or form a micelle-like structure around the quantum dots and keep it soluble until the nanoparticles oxidize and eventually precipitate (Figure **4.2**). The photochemical oxidation of quantum dots took place only after almost all surface thiols were converted to disulfides, so it was assumed that nanocrystal functioned as catalyst for the oxidation of surface thiols, while the surface thiols functioned as photooxidation scavengers [62].

Chapter 5

Application of Quantum Dots in the Life Sciences

Almost two decades ago, colloidal quantum dots were developed and used mainly for optical and electronic applications, such as designing nanoscale light-emitting diodes (LED) [70, 71] or semiconductor-based lasers [72]. In 1998, they were successfully conjugated to proteins and used for cellular imaging [3, 4]. Since then, new possibilities of quantum dots have been discovered and their application in the life sciences have been intensely investigated.

5.1 Bioconjugation of Quantum Dots

There are three major approaches for the bioconjugation of quantum dots: *(1)* peptide bond formation between carboxyl-functionalized quantum dots and amines on the surface of proteins using 1-ethyl-3-(3-dimethylaminopropyl) carbodiimide (EDC); *(2)* direct binding of thiolated peptides to the surface of quantum dots; and *(3)* adsorption or electrostatic assembly of engineered proteins onto charged surfaces of quantum dots [73].

The bioconjugation of quantum dots via peptide bond formation requires the activation of carboxyl groups on the nanoparticle, for example, with EDC (Figure **5.1**). EDC reacts with carboxylic acids to create an active-ester intermediate. In the presence of an amine nucleophile, a peptide bond is formed with the release of an isourea by-product (Figure **5.1**) [74]. The EDC-carboxylic acid reaction occurs effectively up to pH 7.5 without significant loss of yield, although the pH range for optimal binding is between 4.7 and 6 [74]. Moreover, the poor solubility of mercaptoacids in neutral and especially acidic buffers may cause the aggregation at higher concentrations of carboxyl-functionalized quantum dots [73]. However, the use of small quantum dot concentrations at high quantum dot-to-protein ratio and subsequent purification by gel filtration or dialysis allows one to obtain 1:1 quantum dot-protein conjugates [3, 74].

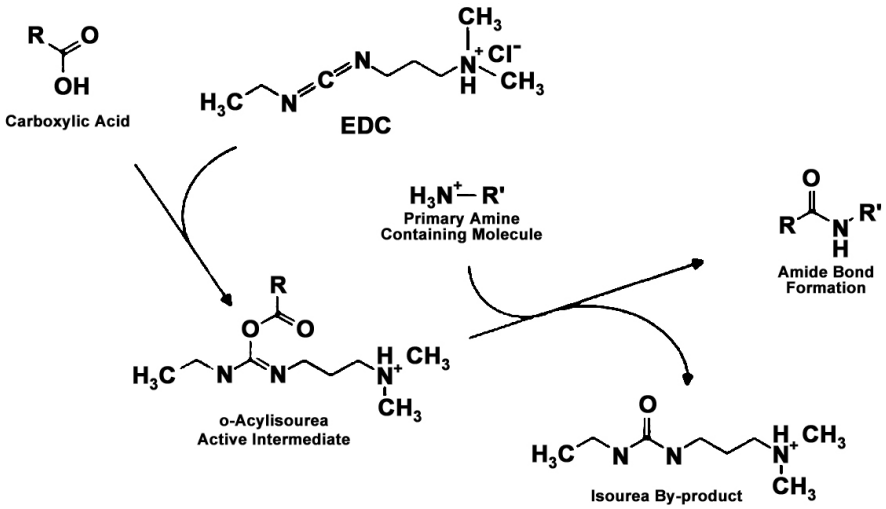

Figure 5.1: 1-ethyl-3-(3-dimethylaminopropyl) carbodiimide (EDC) reacts with carboxylic acids to create an active-ester intermediate. In the presence of an amine nucleophile, an amide bond is formed with release of an isourea by-product. Adapted from [74].

Direct attachment of thiolated biomolecules, such as phytochelatin-related peptides, to the surface of quantum dots allows one to construct rather stable biocompatible quantum dot conjugates by overcoating the nanoparticle surface [73, 75]. However, this approach increases the overall size of the quantum dot and does not simplify the strategy for specific one-to-one labelling.

Another conjugation scheme is based on electrostatic self-assembly of engineered proteins with positively charged domains on negatively-charged carboxyl-functionalized quantum dots [69]. However, this strategy may result in a heterogenous protein orientation on the quantum dots surface and the inability to control protein-to-quantum dot ratio and aggregation. Therefore, an additional purification step should be considered in order to obtain one-to-one protein-quantum dot conjugates [73, 69].

5.2 Solubility and Aggregation of Functionalized Quantum Dots

For biological applications, quantum dots are usually functionalized with bifunctional charged ligands, providing hydrophilicity to the nanoparticles. The mercaptoacid-coated quantum dots are fully soluble in distilled water (pH = 5 – 6) only upon addition of a strong base for deprotonation of the carboxylic acid groups [76]. At neutral pH, used for a number of buffers and cell culture

media, mercaptoacid-coated quantum dots are only partially deprotonated (e.g., 11-mercaptoundecanoic acid, with $pK_a = 6.5$), which may cause aggregation [77].

5.3 Förster Resonance Energy Transfer (FRET)

Single molecule FRET measurements of dye-labeled biomolecules diffusing through a confocal volume are widely used in studies of conformational and binding dynamics [78, 79, 80]. This method has the advantage of simple sample preparation and homogeneous, native-like solution environments. However, the observation time is limited to the diffusion time of the molecule through the femtoliter confocal volume (about a millisecond), and results are only meaningful when averaged over many molecules. In order to probe true single-molecule events for longer than a millisecond, immobilization of the biomolecule is required – sometimes even directly on a functionalized coverglass surface.

An example of this strategy was shown following helix-coil transitions of single two-stranded peptide immobilized on amino functionalized glass [81]. For this relatively simple system, the interacting effect of the surface was evident from the broader distribution of FRET distances of biomolecules on a surface than in solution. For more complex, marginally stable systems, this interaction could prove very damaging. A more friendly, less interacting system is to trap the single protein molecule into an immobilized lipid vesicle [82].

However, even with immobilization on a surface, many longer timescale processes cannot be followed using single dye molecules due to rapid photobleaching of the probe, which affects the data analysis and interpretation [78]. To study slow timescale changes in single biomolecules, quantum dots are a promising alternative but require a very carefully constructed conjugate. The stabilizing capping materials need to be small enough not to render the distance from the emitting core too large from the acceptor molecule to be outside the Förster distance, but large enough to avoid quantum dot aggregation.

FRET from quantum dot donors to dye labeled protein acceptors has been recently demonstrated at the ensemble level to highlight the ability of tuning the spectral overlap integral (and therefore the FRET efficiency) with quantum dot size [83, 84]. This approach was extended to using FRET as a method of dye photoactivation to modulate between fluorescent and non-fluorescent forms of the dye [85].

5.4 Single Particle Tracking

Single molecule techniques to follow processes in biophysics and life-science research have become very rewarding in recent years because they reveal intrinsic properties and heterogeneities of single molecules that are averaged out in en-

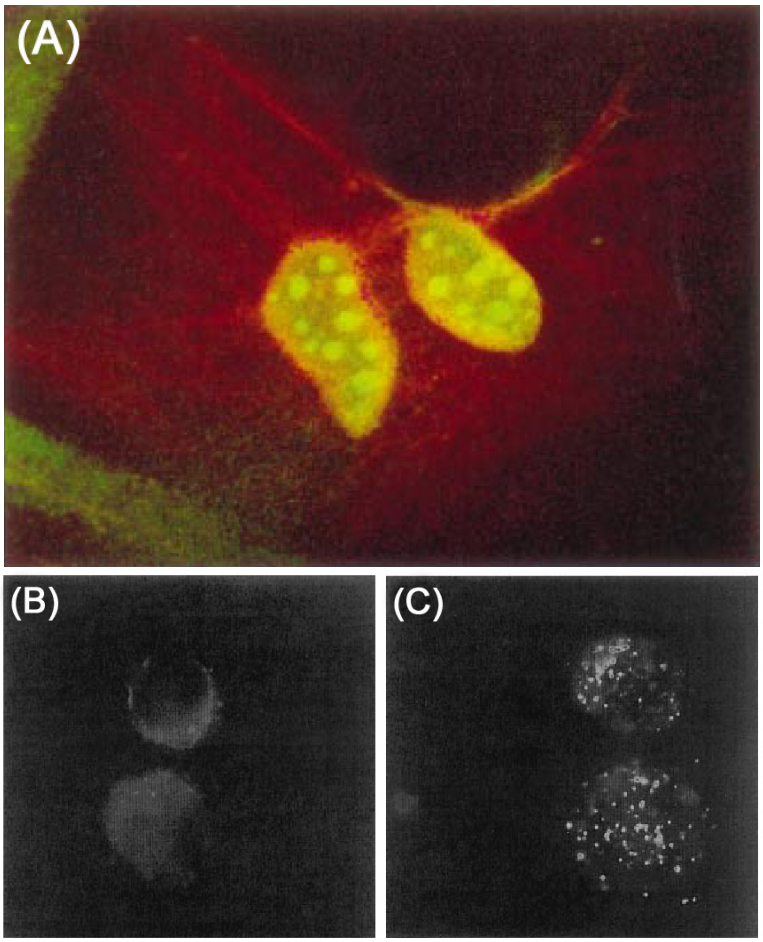

Figure 5.2: (A) Cross section of a dual-labeled mouse 3T3 fibroblasts examined with laser-scanning confocal microscope. A false-colored image was obtained with 363-nm excitation, with simultaneous two-channel detection. Image width: 84 μm. Reprinted from [4]. (B-C) Luminescence images of cultured HeLa cells that were incubated with (B) mercapto-QDs and (C) QD-transferrin conjugates. Cell diameter $\sim$10 μm. Reprinted from [3].

semble measurements, such as the diffusion of individual H-Ras molecules in the dorsal plasma membrane of live mouse cells [86]. The main advantage of quantum dots for single molecule tracking experiments is their excellent brightness and photostability which allows tracking over many minutes [6, 87]. Water-soluble quantum dots were recently used for tracking single glycine receptors in the synapses of neural cells [87], and single particle tracking of quantum dot-labeled membrane transport and receptor proteins expressed in excitatory and inhibitory neurons to determine their mobility [88].

5.5 Quantum Dots for Applications in Cells

The superior photostability and brightness of quantum dots can be used for applications in fluorescence microscopy. Advanced fluorescence microscopy techniques allow one to distinguish and track the movement of different fluorescent species. The application of quantum dots in cellular biophysics enables long-term experiments, which may help to achieve a more detailed understanding of the biochemical mechanisms of different cell lines. However, in order to use quantum dots for specific cellular labelling, it is important to investigate non-specific interaction of quantum dots with cells.

5.5.1 Labelling Cells Using Quantum Dots

The first cell labelling experiments with quantum dots were conducted by incubation of mouse 3T3 fibroblasts [4] and HeLa cells [3] with CdSe/ZnS quantum dots. To demonstrate the advantages of quantum dots, *Bruchez et al.* used smaller, green-emitting quantum dots to stain the nucleus and larger red-emitting nanoparticles functionalized with phalloidin-biotin to specifically label the F-actin filaments and illuminated them with a single light source (Figure **5.2(A)**) [4]. *Chan et al.* [3] have demonstrated specific internalization of transferrin-quantum dots bioconjugates to trypsin-treated HeLa cells by receptor-mediated endocytosis and almost no ingestion of quantum dots by cells in the absence of transferrin (Figure **5.2(B,C)**) [3].

5.5.2 Cytotoxicity of Quantum Dots

The most-widely used quantum dot system for applications in the life sciences utilizes Cd and Se ions, which are known to be highly toxic for cells. Therefore, the potential cytotoxicity should be considered. For many quantum dot preparations, incubation of cells with quantum dots dissolved in culture medium did not lead to detectable differences from untreated cells over a period of two or more weeks, even for quantum dots concentrations of 400 – 600 nM [75, 89, 90, 5, 91]. However, these observations seem to depend on the cell type and on the functionalization of quantum dots with stabilizing water-soluble ligand shell [77]. For primary hepatocyte cells, used as a liver model, *Derfus et al.* [5] reported significant cytotoxic effect of mercaptoacetic acid-coated CdSe quantum dots. The toxicity was found to result from surface oxidation through various pathways, and resulted in release of free cadmium ions, which caused cell death [5]. Surface coatings such as ZnS and BSA were shown to reduce the observed cytotoxicity [92, 5]. Moreover, results obtained by *Hoshino et al.* [63] indicate that the toxic effect of quantum dots on biological objects may be significantly suppressed by a dense, chemically stable ligand shell. Furthermore, CdSe/ZnS core/shell quantum dots functionalized with mercaptoacetic acid and peptides were tested

in vivo, by injection into the tail veins of mice, and no visible toxic effect were reported over the following 24 h [93].

Part II

Experiments

Chapter 6

Synthesis and Characterization of Quantum Dots

6.1 Chemical techniques

6.1.1 CdSe Quantum Dot Synthesis

Synthesis in TOPO/HDA

Our synthesis of CdSe nanoparticles was initially based on the original method introduced by *Murray* and *Bawendi* [2], incorporating the improvements developed by *Talapin et al.* [17] and *Peng and Peng* [30]. This method uses cadmium oxide as a precursor and a mixture of TOPO and HDA as a coordinating solvent. In a typical synthesis, CdO (0.80 mmol) and stearic acid (4.22 mmol) were heated to 190 – 210°C under an argon atmosphere until a clear, colorless solution was obtained, indicating that cadmium had dissociated from the oxide and complexed to the stearate ions. TOPO (8.66 mmol) and HDA (6.83 mmol) were then added to the reaction mixture and the temperature was further increased to 300°C. Once the temperature was reached, the heating was removed and a solution of Se (0.80 mmol) in 4 ml of TOP was quickly injected into the reaction mixture under rapid stirring, which led to immediate nucleation and growth of the nanoparticles. Aliquots were taken at 1 – 3 min time intervals and dispersed in cold toluene. In order to obtain large nanoparticles ($> \sim$4 nm), the temperature was slowly raised until the desired size was obtained.

Synthesis in OLA/OA

CdO (0.8 mmol) and oleic acid (2.5 mmol) were heated to 200°C under an argon atmosphere until a clear, colorless solution was obtained and oleylamine (12 mmol) were added. The mixture was further heated to 250°C with vigorous stirring, then the heating was removed and Se (0.80 mmol) in 4 ml of TOP was

quickly injected. Aliquots were taken over time and dissolved in cold toluene, yielding CdSe quantum dots of different sizes.

6.1.2 Capping with ZnS: Traditional Method

The amounts of Zn and S precursors needed for capping of CdSe of a given size were calculated by the increase in volume upon adding the required number of shell monolayers:

$$V_{ZnS} = \frac{4}{3}\pi(r_c + n \cdot r_m)^3 - \frac{4}{3}\pi r_c^3 \; ; \tag{6.1}$$

where r_c is the core radius, r_m is the thickness of one monolayer of ZnS (0.31 nm) and n is the desired number of monolayers. The necessary amount of Zn and S was calculated from this volume using the density of wurtzite ZnS (3.98 g/cm^3).

Capping in TOPO/HDA

The injection solution was prepared by dissolving equimolar amounts of diethylzinc (from a 1.1 M $Zn(C_2H_5)_2$ solution in toluene) and hexametyldisilathiane (HMDST) in TOP. The corresponding amount of uncapped CdSe quantum dots were mixed with 1.6 g of TOPO and 0.8 g of HDA in a three-neck flask and heated to 165 – 175°C. The zinc/sulfur injection solution was added dropwise to the reaction mixture while maintaining the temperature (dripping speed ∼10 min per monolayer). Aliquots were taken during the ZnS shell growth to be monitored by absorption and emission spectroscopy.

Capping in OLA/OA

The zinc injection solution was prepared by dissolving zinc stearate in a 1:5 mixture of oleic acid (OA) and oleylamine (OLA) at 100°C. Separately, the sulfur injection solution was prepared by the dissolving the elemental sulfur in OLA at room temperature.

In a typical overcoating reaction, 5 – 6 ml of OLA and 2 ml of OA were added to a toluene solution of CdSe quantum dots and the mixture was stirred and heated to 120°C for about 30 min in order to evaporate the toluene, then the temperature was raised to 165°C and the calculated amounts of zinc stearate and sulfur dissolved in OLA/OA were introduced by slow dripping (∼5 – 10 min per monolayer).

6.1.3 Capping with ZnS: SILAR method

The successive ion layer absorption and reaction method (SILAR) developed by *Peng et al.* [28] is based on the separate addition of shell components in an alternating fashion. The concentrations of both Zn^{2+} and S^{2-} ions were calculated

from the increase in volume of a nanoparticle with each monolayer and the density of the shell material, using the same formula as for the traditional method (Equation **6.1**). Typically, 0.3 M injection solutions were prepared from zinc stearate dissolved in 1-octadecene (ODE) at 200°C and elemental sulfur dissolved in ODE at 150°C. In the first step, a solution of CdSe quantum dots in toluene was mixed with 1.36 g of hexadecylamine and 5 g of 1-octadecene, and heated up to 100°C under argon flow. The mixture was carefully degassed under vacuum and left to stir for approximately 30 min. Then the temperature was further raised to 200°C and the calculated amount of the 0.3 M sulfur injection solution was added to the reaction mixture. To monitor the shell growth, aliquots were taken every 3 – 5 min after the injection for measurement by absorption spectroscopy. When no further changes were observed in the UV-Vis spectrum of two consecutive aliquots, the adsorption of ions was assumed to be complete. Typically, 10 – 15 min was required to grow one ion layer (half a monolayer). This procedure was then repeated for the Zn injection solution. After the desired amount of monolayers was achieved, the reaction was stopped, the solution was cooled down to room temperature and the product separated from the unreacted precursors by precipitation of the particles in a methanol-hexane solution and centrifugation at 10416 × g for 1 h. The unreacted ions remained dissolved in the solution. The pellet was separated from the solution and redissolved in chloroform.

6.1.4 Ligand Exchange with 11-Mercaptoundecanoic acid (MUA)

Ligand Exchange in Methanol

ZnS-capped CdSe quantum dots were functionalized with carboxylic groups by replacing the initial hydrophobic surfactants (TOPO and HDA) with 11-mercaptoundecanoic acid (MUA). The ligand exchange reaction was based on the procedure published by *Yu et al.* [94]. To a 20 mg solution of 11-MUA in 15 ml of methanol at pH 10.3 (adjusted with tetramethylammoniumhydroxide pentahydride (TMAHP)), 20 mg of quantum dots were added. The mixture was left refluxing and stirring at 70°C overnight under argon in the dark. The resulting solution was precipitated with ethyl acetate and ether and separated by centrifugation. The pellet was redissolved in methanol and the precipitation/centrifugation cycle was repeated two more times. In a modified procedure, larger amounts of MUA were taken for the exchange, 20 – 40 mg of MUA per 1 mg of quantum dots.

Ligand Exchange in 1,4-Dioxane

This procedure was originally developed by *Reiss et al.* [22]. 20 mg of capped quantum dots and 200 mg of MUA were dissolved in 4 ml of 1,4-dioxane. After

approximately 14 h of stirring at 60°C, quantum dots precipitated from the solution and were centrifuged. After washing several times with 1,4-dioxane, they were redispersed in water by the addition of ammonium hydroxide to a pH of ∼10.

Ligand Exchange in Methanol / 1,4-Dioxane (1:1)

A combination of two solvents, methanol and 1,4-dioxane, were also used for the ligand exchange. Six different MUA-to-quantum dot ratios were taken: 4, 20, 40, 80, 160 or 240 mg of 11-mercaptoundecanoic acid per mg of quantum dots. 0.5 mg of quantum dots and the corresponding amount of MUA were dissolved in 30 ml of a 1:1 methanol/dioxane solvent. The pH of the solution was adjusted to 12.5 – 13 with TMAHP. The flask was purged with N_2 and the temperature was raised to 70°C with stirring. Samples were taken from the reaction mixture at different time intervals in order to monitor the exchange. The exchanged particles were precipitated with ethyl acetate, the solution was centrifuged at 10416 × g for 45 mins and the resulting pellet was redissolved in methanol. After 3 cycles, the precipitated solid was redissolved in water. The quantum yield was calculated for each sample in order to monitor the extent of ligand exchange.

6.1.5 Ligand Exchange with *D*-Penicillamine

80 mg of *D*-penicillamine (DPA) was mixed with 30 ml of 2-propanol and the pH was adjusted to 12 – 13 with TMAHP. The mixture was sonicated for 1 min to obtain clear solution. Then 0.5 mg of TOPO/HDA-coated CdSe/ZnS quantum dots were added and the reaction mixture was left stirring at 70 – 80°C under a nitrogen atmosphere for 48 h (10 – 20 min for OLA-coated CdSe/ZnS quantum dots). Aliquots were taken every 6 h to monitor the extent of ligand exchange. After the reaction was stopped, the mixture was cooled to room temperature and the exchanged hydrophilic quantum dots were precipitated with ethyl acetate. The pellet was centrifuged out and redispersed in water.

6.1.6 Colloidal Stability of Water-Soluble CdSe/ZnS Quantum Dots

10-nM solutions of MUA-CdSe/ZnS and DPA-CdSe/ZnS quantum dots at different pH were prepared from 1 μM stock solutions by dissolving 10 μl of QDs in 990 μl of the corresponding buffer. The following buffers were used: pH 5.0, 100 mM sodium citrate/sodium phosphate buffer; pH 7.0, 100 mM sodium phosphate buffer; and pH 9.2, 100 mM sodium carbonate buffer. Water-soluble quantum dots were immobilized on poly-L-lysine-coated glass slides. To coat the glass slides, 20 μl of 0.01% poly-L-lysine in 100 mM PBS solution was added into a channel, formed by two glass cover slips and double-sided adhesive tape, and left

to react with the glass surface for 15 – 20 min. Then the channel was flushed with 18.2 MΩ·cm Millipore water several times. 20 μl of quantum dots in buffer was added to the channel and left for another 15 – 20 min. Subsequently, the channel was rinsed several times with the corresponding buffer.

6.2 Characterization of Quantum Dots

6.2.1 Quantum Yield

Absorption spectra were measured using a Cary 1E spectrometer (Varian, Palo Alto, CA) and emission spectra were measured on a Fluorolog II fluorometer (SPEX industries, Edison, NJ) equipped with a 450 W xenon lamp.

Quantum yield was calculated using the comparative method by *Williams et al.* [95], which involves the use of a standard sample with known quantum yield as a reference. The quantum yield Φ is obtained from the following equation,

$$\Phi = \Phi_R \frac{I}{I_R} \frac{OD_R}{OD} \frac{n^2}{n_R^2}, \tag{6.2}$$

where I is the integrated fluorescence intensity, OD is the optical density at 500 nm, and n is the refractive index of the solvent. The subscript R refers to the reference, rhodamine 6G in ethanol in our case. To avoid inner filter effects, dilute, optically thin samples (OD at 500 nm < 0.1) were used for all measurements.

6.2.2 TEM Characterization

Transmission electron microscopy was used for the characterization of particle size and shell thickness. Quantum dots were precipitated with methanol from crude solution, centrifuged at 10416 × g for 45 min and redissolved in toluene. After 3 cycles, the pellet was redispersed in chloroform and deposited onto 300-mesh carbon-coated copper grids (purchased from PLANO GmbH, Germany). The grids were investigated on a Philips EM-400 transmission electron microscope (Eindhoven, The Netherlands) at an accelerating voltage of 80 kV and on a FEI Titan 80-300 transmission electron microscope (Hillsboro, Oregon, USA) with C_s-corrector of objective lens at an accelerating voltage 300 kV.

6.2.3 AFM Characterization

Atomic force microscopy (AFM) was used to investigate the aggregation of MUA-coated quantum dot samples prepared using different solvent systems at the single-particle level. Dilute water-soluble quantum dots solutions (∼0.1 – 1 nM) were dried on a glass surface and topographic images were obtained on a *JPK*

NanoWizard® I AFM (JPK Instruments, Berlin, Germany) operating in tapping-mode using non-coated cantilevers with a silicon backside (NSC36/No Al, Micro-Mash, distributed by Anfatec Instruments AG, Oelsnitz, Germany).

6.2.4 Luminescence Quenching

Quenching experiments were performed at 25°C in a SPEX fluorimeter by measuring emission spectra between 510 and 750 nm with excitation at 500 nm. Various thiolated compounds and their non-thiolated analogues were used as quenching agents, including mercaptoacetic acid (MAA), acetic acid (AA), β-mercaptoethanol (BME), ethanol (EtOH), mercaptobenzoic acid (MBA) and 11-mercaptoundecanoic acid (MUA). First, the integrated luminescence intensity of the quantum dot sample without quencher was determined. Then the quencher from a concentrated aqueous stock solution was added to obtain a series of spectra with varying quencher concentrations. The spectra were corrected for dilution, and I_0/I was calculated at each quencher concentration, where I_0 and I are the luminescence intensities without and with quencher, respectively.

6.2.5 Chemical Stability of Water-Soluble Quantum Dots

For the investigation of chemical (colloidal) stability, two identical samples of water-soluble quantum dots were stored in cuvettes under two different conditions – in the dark and exposed to constant room light. Absorption spectra of both samples were measured every day for the first week and every 3 – 5 days for a month.

Chapter 7

Fluorescence Microscopy Techniques

7.1 Total Internal Reflection Fluorescence Microscopy

Total internal reflection fluorescence microscopy (TIRFM) allows a thin region of specimen near the surface (< 300 nm) to be observed. This method was developed in 1981 by Daniel Axelrod at the University of Michigan in order to image the thin section of immobilized cells close to the surface [96].

Total internal reflection of the excitation beam occurs at the interface between two media, where the light travels from a medium with a higher refractive index to one with a lower refractive index. When light reaches this interface at the critical angle θ_c, it is refracted parallel to the interface. At larger angles it is reflected entirely back into the first medium (total internal reflection) and the reflected light generates an electromagnetic field adjacent to the interface into the lower-index medium, identical in frequency to the excitation light. This evanescent field decays exponentially in intensity with distance from the interface, the z direction, which decays to zero within 100 – 300 nm (Figure **7.1(A)**). Thus, TIRFM allows one to observe approximately 10-fold thinner regions compared to scanning confocal fluorescence microscopy techniques and, by avoiding excitation of fluorophores in the bulk of the specimen, offers very high signal-to-noise ratios for samples immobilized on a surface.

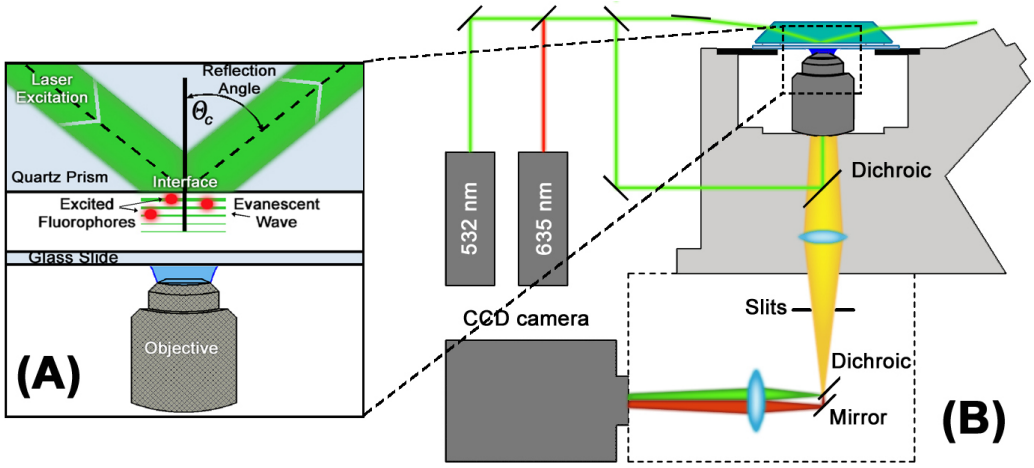

Figure 7.1: (A) Principle of total internal reflection; (B) Schematic of prism-type TIRFM setup.

7.1.1 Experimental Setup

Sample Cell Description

The "sandwich" used as the sample cell for TIRFM experiments consists of a ~20 × 20 mm^2 quartz prism (Aachner Quartz-Glas Technologie Heinrich, Aachen, Germany) fixed on a 24 × 32 mm^2 glass slide (Menzel-Gläser, Braunschweig, Germany) with two strips of ~200 μm double-sided adhesive tape, forming a narrow channel (2 – 3 mm) between the prism and glass slide (Figure **7.2**).

Microscope Configuration

We used a *prism-type* configuration for the TIRF microscope with excitation from a Nd:YAG laser (Uniwave Technology Co Ltd, Shanghai, China) operating at 532 nm. In the prism configuration of TIRFM, a laser beam strikes the lateral face of the prism, which is placed on top of the "sandwich" (Figure **7.2**) and the beam incidence angle is adjusted to above the critical angle. The fluorescence from the specimen immobilized on the prism surface is collected by a high numerical aperture objective focused on this interface and detected by an intensified CCD camera (Figure **7.1(B)**). The setup is designed for two-color excitation and/or two-color detection using dichroic mirrors as described in Figure **7.1(B)**.

7.1.2 Applications

TIRFM was used for the investigation of fluorescence intermittency of core/shell quantum dots immobilized in a PMMA film on the prism surface.

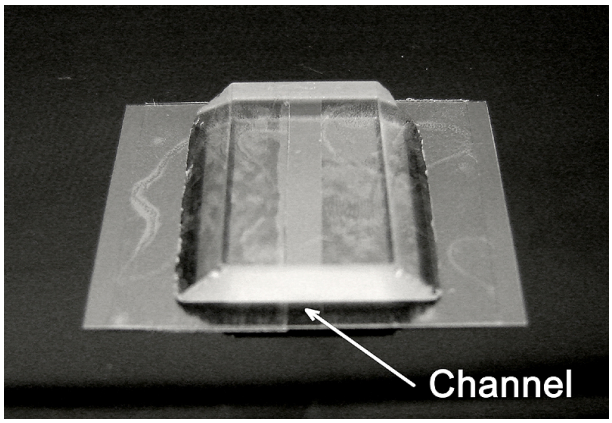

Figure 7.2: Photograph of a typical "sandwich" used for the TIRFM experiments.

Sample Preparation

Quantum dot solutions were diluted in toluene to picomolar concentrations, and mixed in a 1 : 1 ratio with 4% (mass/volume) poly(methylmethacrylate) (PMMA) in 2-butanone. The solutions were then spin cast onto quartz prisms at 2000 rpm, and "sandwiches" were made as it shown in Figure **7.2**. The channels in the obtained "sandwiches" were filled with water.

Trace Analysis

In order to obtain good statistics, we measured four to five areas of 80 μm $\times$ 80 μm for each sample for several hundred seconds each. A typical intensity time trace (with 100 ms time binning), with an intensity histogram in the right frame, is shown in Figure **7.3**. The background intensity was determined locally around each particle; it follows a Poissonian distribution, a discrete probability distribution that expresses the probability of a number of events occurring in a fixed period of time if these events occur with a constant average rate (mean intensity) and independently of the time since the last event. For our data, a Poissonian distribution of the background intensity has a standard deviation σ $\sim$25 Hz (Figure **7.3**). A threshold separating "*on*" states from "*off*" states is set to multiples of σ to ensure that background noise does not generate any false short "*on*" events. For thresholds between 2σ and 4σ, no effect on the blinking statistics was found, since the emission intensity frequency of quantum dots in the "*on*" state in our experiments is 200 – 400 Hz, far greater than the background noise. For all subsequent analyses, the threshold was set to 70 Hz (Figure **7.3**). Furthermore, the spot shapes were analyzed to ensure that only single quantum dots (no larger than their point spread function), well separated from neighboring spots, were included in the analysis.

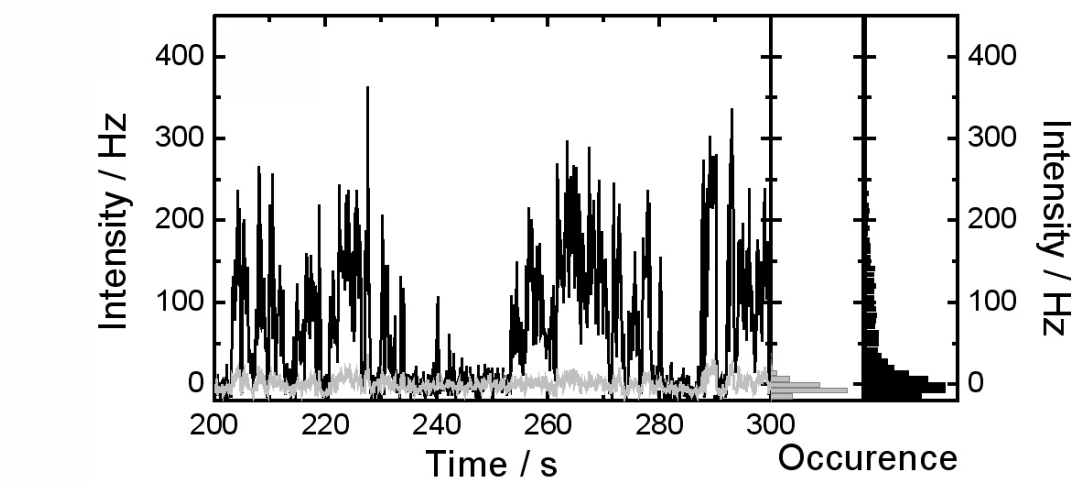

Figure 7.3: Typical fluorescence time trajectory of a single quantum dot with 100 ms binning (black line). Local background calculated from a set of pixels immediately surrounding the single quantum dot spot (grey line).

7.2 Scanning Confocal Fluorescence Microscopy

Confocal microscopy was developed by Marvin Minsky in 1957 (patent granted 1961) [97]. The method allows one to eliminate out-of-focus light very effectively, reducing the detection volume and significantly increasing the signal-to-noise ratio. A confocal system, consisting of a point excitation source, dichroic mirror, objective lens, detection pinhole and detector is shown in Figure **7.4(A)**. Light from a point source is reflected by a dichroic mirror and focused by a lens onto a sample. The sample is excited not only in the focal plane **(b)**, but also between planes **(a)** and **(c)**, which define the sample borders (Figure **7.4(A)**). In order to collect the signal exclusively from the focal plane **(b)**, a pinhole is inserted in the detection path, which removes the out-of-focus emission.

7.2.1 Experimental Setup

Sample Cell Description

A "sandwich" sample cell was used for the scanning confocal fluorescence microscopy experiments, which consisted of a 20 × 20 mm^2 glass slide (Menzel-Gläser, Braunschweig, Germany) fixed on a 24 × 32 mm^2 glass slide (Menzel-Gläser, Braunschweig, Germany) with two strips of ∼200 μm double-sided adhesive tape, forming a ∼3 – 4 mm wide channel between the upper and lower glass slides, as shown in Figure **7.5**.

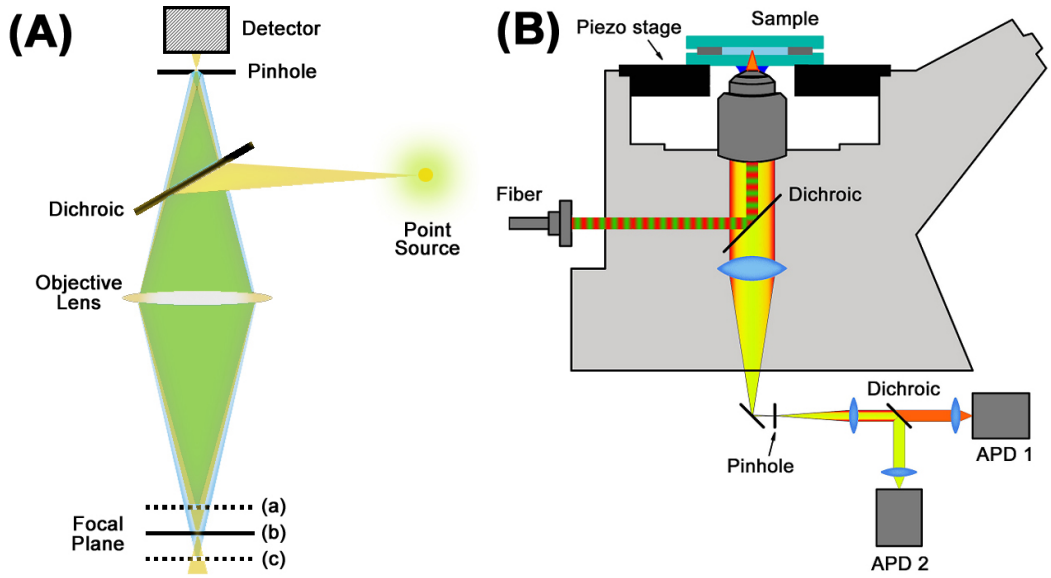

Figure 7.4: (A) Principle of a confocal system, consisting of a point excitation source, dichroic mirror, objective lens, detection pinhole and detector. (B) Schematic of a two-channel ultrasensitive scanning confocal fluorescence microscope.

Microscope Configuration

Green and/or red laser beams are delivered to the microscope through fiber optics and reflected by a dichroic mirror into the objective lens, which focuses the beam onto the sample (Figure **7.4(B)**). The emission from the sample is collected by the same objective lens, transmitted through the dichroic mirror and focused onto the pinhole. Then, it is divided in two spectral channels by a dichroic mirror and detected by two separate avalanche photodiode (APD) detectors, APD-1 and APD-2.

For the single-quantum dot experiments we used an Ar^+-ion laser (Spectra-Physics, Mountain View, CA) operating at 514 nm. Pulsed laser sources were required for the determination of the fluorescence lifetimes of water-soluble quantum dots for the fluorescence quenching studies. For these experiments, a mode-locked NG:YAG laser operating at 532 nm with a 40 MHz repetition rate was used (Time-Bandwidth Products GE-100, Zürich, Switzerland).

7.2.2 Applications of Scanning Confocal Fluorescence Microscopy

We used ultrasensitive scanning confocal fluorescence microscopy for the investigation of the aggregation state of quantum dots, for the analysis of luminescence lifetimes of quantum dots, and for studies of non-specific interaction of water-

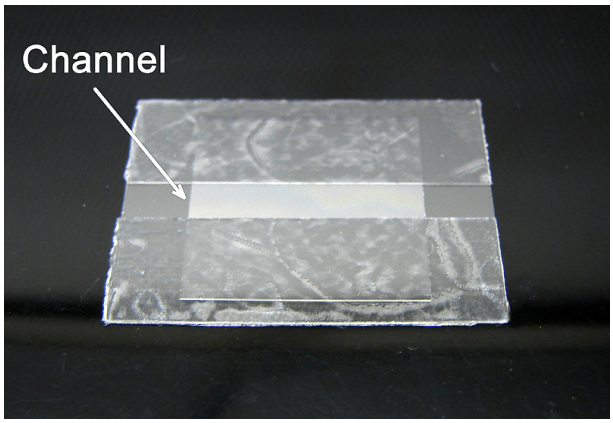

Figure 7.5: A photograph of the typical "sandwich" used for the experiments on the Scanning Confocal Fluorescence Microscope.

soluble quantum dots with Mono Mac 6 cells.

Sample Preparation

For the investigation of the aggregation of MUA-coated quantum dots on the single-particle level, a dilute aqueous quantum dot solution was mixed with polyvinyl alcohol (PVA) and spin-cast onto a 24 × 32 mm^2 glass slide (Figure **7.5**). The glass slide with the immobilized quantum dots was then used in the "sandwich" preparation as a lower half, exposing the immobilized quantum dots to the channel filled with water.

For the studies of non-specific interaction of water-soluble quantum dots to cells, the corresponding concentrations of water-soluble quantum dots were filled into the channel, with cells immobilized on the lower glass slide of the "sandwich" shown in Figure **7.5**.

Cell Culture and Viability

Human monocytic cell line Mono Mac 6 was obtained from DSMZ, the German Collection of Microorganisms and Cell Cultures (Braunschweig, Germany). The cells were cultured in suspension in advanced RPMI 1640 medium (Invitrogen) supplemented with 10% fetal calf serum (FCS) and 1% penicillin/streptomycin/*L*-glutamine (PSG). To ensure cell viability during and after completion of confocal fluorescence microscopy experiments, we added 75 nmol/L propidium iodide (Molecular Probes, Eugene, OR, USA), which does not penetrate into the cells when they are viable. As a positive control, subsequent permeabilization with 0.1% Triton X-100 (Sigma-Aldrich, Taufkirchen, Germany) yielded bright nuclear staining due to the integration of propidium iodide into nuclear DNA.

Part III

Results and Discussion

Chapter 8

Synthesis and Modification of Core/Shell Quantum Dots

8.1 Synthesis of CdSe Quantum Dots

For the synthesis of uncapped CdSe quantum dots, the methods proposed by *Peng et al.* [30] and *Talapin et al.* [17] were combined. CdO was used as cadmium precursor, while selenium was used in elemental form. The CdO was first heated in a stearic acid melt at 190 – 210°C until the solution became transparent, indicating the dissociation of Cd^{2+} from the oxide, stabilized by stearate. Then an equimolar mixture of TOPO and HDA was added to the reaction volume and the temperature was further increased to 260 – 310°C where TOPO/HDA formed inverse micelles around the cadmium ions. Then the heating was removed and Se complexed to TOP (TOPSe) was swiftly injected into the reaction mixture with rapid stirring.

The temperature of Se injection was critical for the size, size distribution and photoluminescence efficiency of resulting quantum dots. Fast injection at 310°C allowed one to obtain higher quantum yield and more homogenous growth of CdSe nanoparticles as a result of faster nucleation of CdSe at higher temperatures. Temperatures of 260 – 280°C led to the formation of smaller quantum dots.

After injection, aliquots were taken at different time intervals and dispersed in cool (∼20°C) toluene in order to terminate growth, resulting in CdSe quantum dots of different emission colors. Without further temperature increase, CdSe nanoparticles grew to approximately 4 nm, corresponding to "yellow" emitting quantum dots, with peak emission at ∼590 nm. "Red"-emitting quantum dots, with maxima above 600 nm, were only possible to obtain via *Ostwald ripening* in which the reaction vessel is heated to 350°C and stirred for 1 – 2 h.

The synthesis of CdSe quantum dots was found to be highly dependent on the presence of air and humidity and, therefore, was performed under anaerobic conditions. Both argon and nitrogen atmospheres were tested, and argon was found

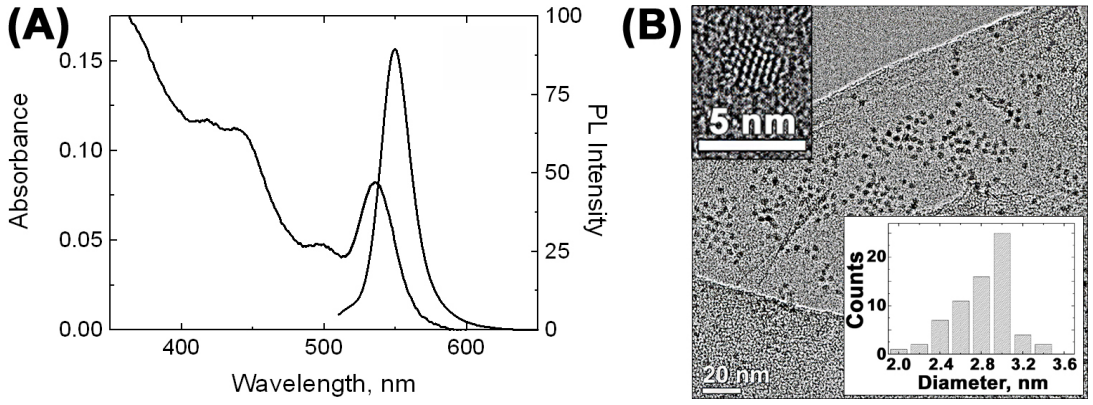

Figure 8.1: (A) Absorption and emission spectra of TOPO/HDA-stabilized CdSe quantum dots with maxima at 542 nm and 556 nm (excitation at 500 nm), respectively. $FWHM_{PL}$ = 25.1 nm; Φ = 11.1%, Stokes shift Δ = 57.8 meV. (B) High resolution TEM micrograph of the same quantum dot batch. Average particle diameter ∼2.9 nm. Hexagonal wurtzite symmetry of a CdSe nanocrystal in the [001] direction (inset).

to be suitable for the synthesis at all temperatures. However, the less expensive approach using nitrogen led to the formation of a dark green precipitate at temperature above 290 – 300°C, possibly corresponding to cadmium nitride complex formation. This factor limited the injection temperature to 280°C when using nitrogen, leading to smaller, lower-quality quantum dots. For most syntheses, argon was used as the inert atmosphere rather than nitrogen.

The approach described above allowed us to reproducibly obtain monodisperse TOPO/HDA-stabilized CdSe quantum dots with photoluminescence efficiencies of 10 – 20% (Figure **8.1(A)**). High resolution electron microscopy of "green" quantum dots with emission peak maximum at 556 nm showed a spherical shape of the nanoparticles, with an average diameter of 2.9 nm (Figure **8.1(B)**). The crystal structure of the nanocrystals appeared to be wurtzite (Figure **8.1(B)** inset), which is in agreement with other data published for quantum dots synthesized using similar methods [2, 17, 18]. Other evidence of hexagonal lattice structure is the presence of secondary peaks in absorption spectra of TOPO/HDA-stabilized quantum dots, which is due to the crystal field splitting effect as a result of crystal anisotropy [19]. Crystal-field splitting is generally observed in wurtzite CdSe [98]. For different syntheses of TOPO/HDA-stabilized CdSe quantum dots with diameter ∼2.8 nm, the splitting between main and secondary peaks varied from about 175 to 181 meV, corresponding to the $1S_{3/2}$ to 1S(e) transition, and from 142 to 197 meV the $1S_{3/2}$ to 1P(e) transition. Results published by *Shiang et al.* showed a 125-meV splitting between the main and secondary absorption peaks for a 3.2-nm wurtzite TOPO-stabilized CdSe quantum dot.

In subsequent attempts to establish a reliable method to obtain quantum dots

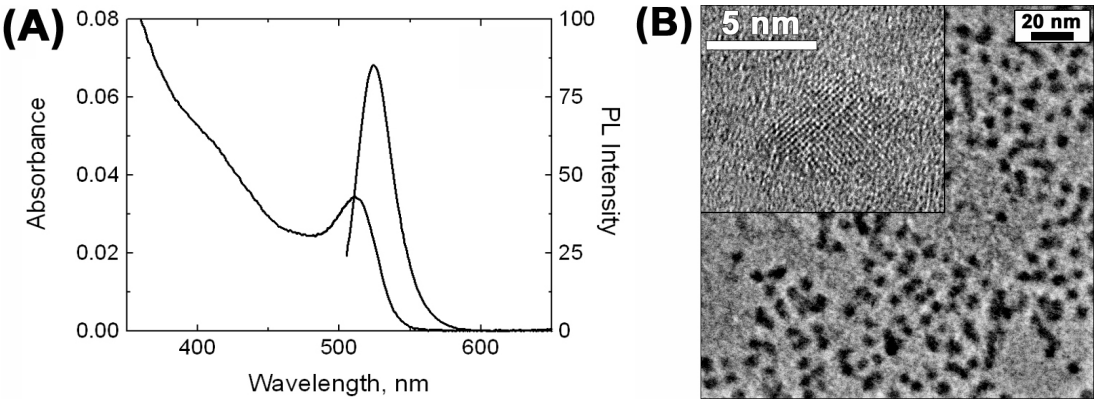

Figure 8.2: (A) Absorption and emission spectra of OLA-stabilized CdSe quantum dots with maxima at 511 nm and 524 nm (excitation at 500 nm) respectively. $FWHM_{PL}$ = 30.3 nm; Φ = 25.4%, Stokes shift Δ = 60.2 meV. (B) TEM micrograph of OLA-stabilized CdSe nanoparticles with emission maximum at 524 nm. High resolution electron micrograph showing the zinc blende structure of the nanoparticles (inset).

of high quality, the surfactant composition was modified. Oleic acid (OA) was used to dissolve CdO and oleylamine (OLA) was introduced as a coordination solvent for cadmium ions instead of TOPO and HDA. The mixture was heated to 250°C upon vigorous stirring, then the heating was removed and the solution of Se in TOP was quickly injected. Aliquots were taken over time and dissolved in toluene, yielding CdSe quantum dots of different sizes. The lower injection temperature was used because of irreversible decomposition of Cd^{2+}/OLA complex above 250°C.

Introducing these changes to the protocol had a significant effect on the properties of the resulting CdSe nanoparticles. Compared to TOPO/HDA-stabilized quantum dots, the full width at half maximum ($FWHM$) of the emission peak of quantum dots prepared in OLA/OA mixture was broader, $FWHM_{PL}^{TOPO}$ = 25.1 nm and $FWHM_{PL}^{OLA}$ = 30.3 nm (Figures **8.1(A)** and **8.2(A)**). This effect can be explained by the better stabilization provided by TOPO [16], leading to a more homogenous growth of TOPO/HDA-stabilized nanoparticles. However, despite the lower injection temperature of Se and the use of less effective stabilizing agents, quantum dots prepared in OLA/OA displayed about a two-fold higher quantum yield (Φ = 24 – 26%) (Figure **8.2(A)**). This observation is in agreement with a previously published article by *Talapin et al.* [17], which reported that the photoluminescence efficiency of TOPO/HDA-coated CdSe quantum dots can be significantly increased by post-preparational treatment with dodecylamine (DDA), which is similar to oleylamine. On the other hand, the observed properties might also be the result of a different surface composition. Since TOPO has a high affinity to Cd, 70% of the nanoparticle surface is comprised of Cd atoms

[16]. However, amines are not known to display a specificity to either Cd or Se, which might lead to an equal Cd:Se surface composition.

For CdSe quantum dots prepared in OLA/OA, a zinc blende crystal structure was observed (Figure **8.2(B)** inset). The crystal structure is determined from the fact that the nearest neighbor distance between the atoms, d_n, in the observed structure was approximately $d_n = 0.23$ nm, which is similar to the parameter of bulk zinc blende at 300 K ($d_n = 0.26$ nm) [99]. The cubic structure can also be inferred from the absorption spectra of OLA-stabilized CdSe quantum dots presented in Figure **8.2(A)**. The secondary peaks present in the spectrum of wurtzite TOPO/HDA-stabilized quantum dots due to crystal field splitting are lacking for those stabilized with OLA (Figure **8.2(A)**). For a number of other semiconductors such as AlN, GaN and InN, bulk crystals revealed crystal-field splitting parameters $\Delta CF = 0$ for the zinc blende structure [100].

8.2 Capping of CdSe Quantum Dots

Overcoating (or capping) of quantum dots with ZnS was performed by combining methods developed by *Hines et al.* [26] and *Talapin et al.* [17]. Typically, a solution of CdSe quantum dots in toluene was heated with 5 g of an equimolar TOPO/HDA mixture to 120°C under argon flow. The mixture was left stirring for 1 h to evaporate toluene and degas the reaction volume. Then the temperature was increased to 165°C and calculated amounts of diethyl zinc and HMDST equivalent to 0.5 monolayer (ML) of ZnS dissolved in TOP were slowly injected by dripping. A small aliquot was taken for characterization and the next amount corresponding to 0.5 ML was added. When the desired amount of monolayers was reached, the reaction mixture was isolated from the flask and redispersed in cool toluene.

The optical properties of CdSe quantum dots, capped with a ZnS shell of various thickness is shown in Figure **8.3**. The sharp increase of the quantum yield with the second injection indicated effective surface passivation of the core by ZnS. By overcoating CdSe quantum dots with 2 – 2.5 ML of ZnS, the maximal photoluminescence efficiency was reached (30 – 35 %) (Figure **8.3(A)**). For a similar capping procedure at 220°C, *Talapin et al.* reported that the maximal photoluminescent efficiency for CdSe was reached upon capping with ∼1.6 ML of ZnS [17]. The quantum yield saturation at 2 – 2.5 ML of ZnS might indicate that this shell thickness was sufficient for total surface passivation or that no more surface area was sterically accessible for passivation. On the other hand, the quantum yield increase by surface passivation might be opposed by the growing contribution of CdSe - ZnS lattice mismatch above 2.5 ML, Figure **8.3(a)**. Lattice mismatches due to differences in bond lengths between Cd-Se and Zn-S (∼13 %) create strain at the core-shell interface, which reduces the quantum yield by providing additional non-radiative pathways [24, 25, 101].

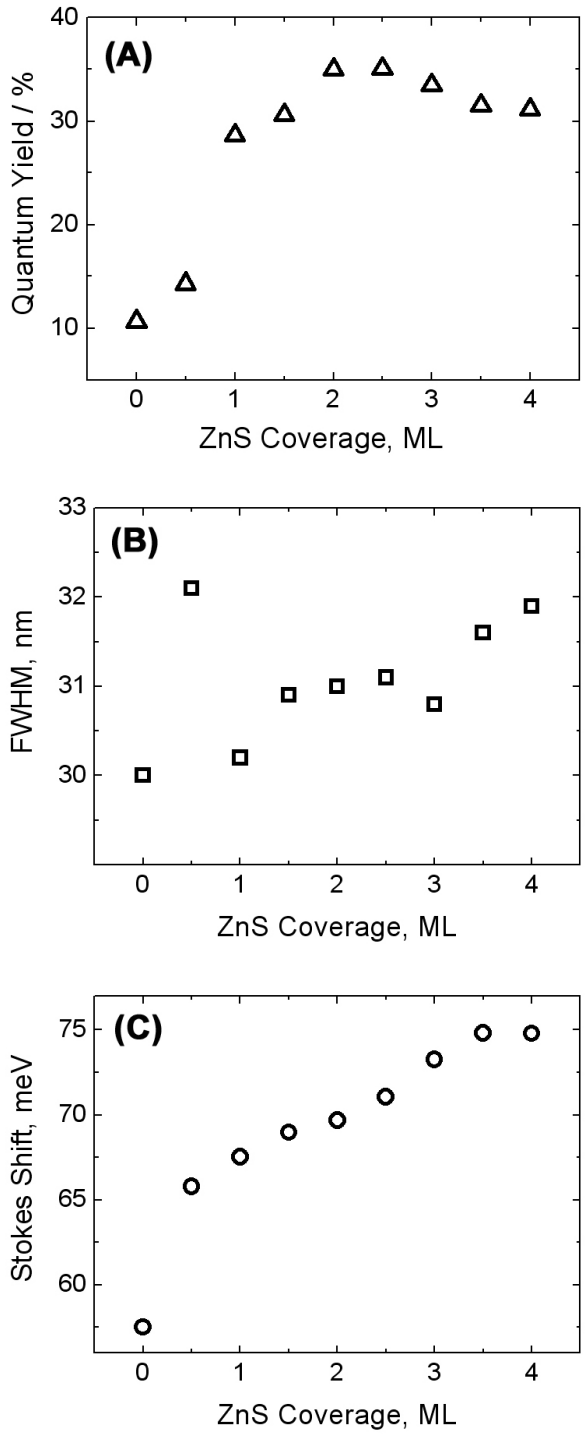

Figure 8.3: Capping CdSe quantum dots with ZnS in the TOPO/HDA system: (A) Increase of photoluminescence efficiency of CdSe quantum dots. A thickness of approximately 2 ML shows the maximum quantum yield. (B) FWHM of the emission showing the CdSe emission peak broadening. (C) Evolution of the Stokes shift of CdSe quantum dot.

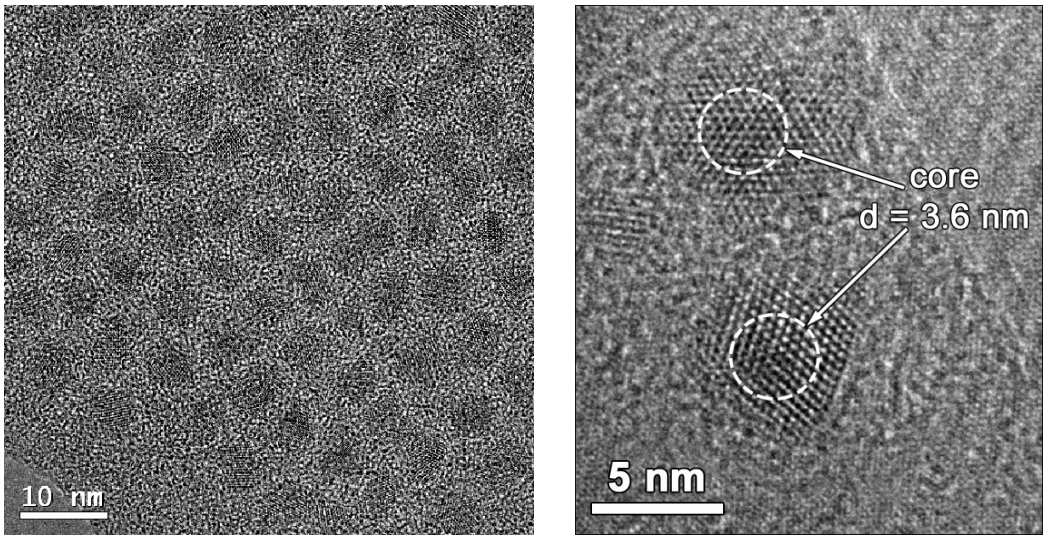

Figure 8.4: High resolution TEM images of CdSe quantum dots capped with 4 – 6 ML of ZnS in the TOPO/HDA system.

The change in the *FWHM* of the emission spectrum is plotted in Figure **8.3(B)**. A large broadening was observed following the first injection, corresponding to 0.5 monolayers of ZnS. This observation highlighted the presence of an uncapped fraction during the initial capping stage. However, the reported broadening during the whole capping process $\Delta FWHM$ = 0.2 – 2.1 nm was small, suggesting that the size distribution of quantum dots was not affected by capping (Figure **8.3(B)**).

Stokes shifts were calculated for each shell thickness as a difference between the first exciton absorption and emission energy maxima (Figure **8.3(C)**). The Stokes shift of uncapped quantum dots should remain constant if the structure of fluorophore is not affected by capping. However, already after the first injection, an increase of the Stokes shift was observed (Figure **8.3(C)**). Interestingly, during the range of shell thicknesses for which the increase in quantum yield is greatest, i.e., during effective surface passivation (0.5 – 2 ML), ZnS capping seemed to alter the structure of the core (Stokes shift ∼12 meV) more than during the range of shell thicknesses for which the lattice mismatch becomes prominent and the quantum yield begins to decrease (2.5 – 4 ML) (Stokes shift ∼4 meV) (Figure **8.3(c)**).

In order to investigate the effect of the CdSe - ZnS lattice mismatch on possible distortion of the wurtzite structure of the cores, we measured high resolution TEM micrographs presented in Figure **8.4**. It is evident that the wurtzite structure of the ZnS shell was templated by the CdSe core; no visible distortion of the core crystal lattice was observed (Figure **8.4**). Furthermore, it can be seen from Figure **8.4** that the distribution of the shell around the core had an irregular

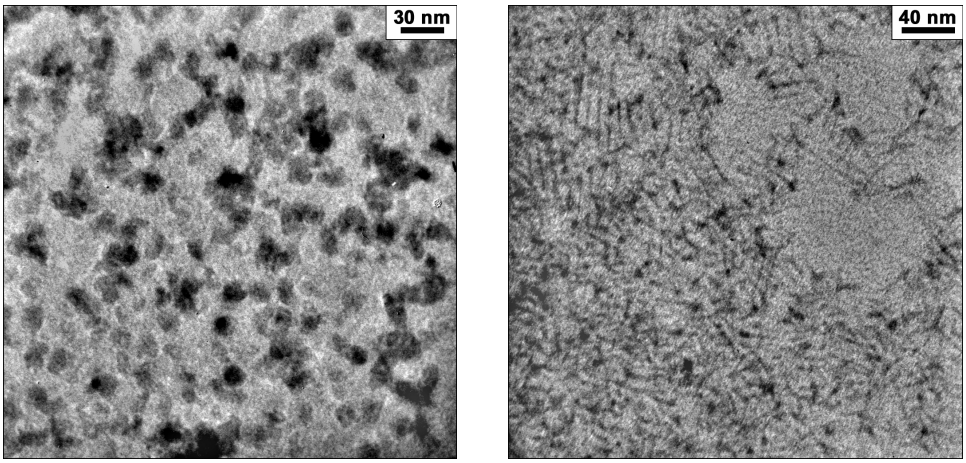

Figure 8.5: Disadvantages of the TOPO/HDA system for ZnS capping: Uncontrollable ripening (left) and unidirectional shell growth (right).

rather than uniform spherical shape. This observation was also reported by *Yu et al.* based on STEM analysis [102].

The capping method described above allows one to obtain high quality spherical core/shell CdSe/ZnS quantum dots, but has a number of disadvantages. The reaction is highly sensitive to even small amounts of impurities. It has very low reproducibility (about 5 – 10%) and may result in a number of by-products, such as individual Zn or ZnS nanoparticles. We attempted to control the formation of byproducts by the speed of injection of the ZnS precursors, addition of zinc and sulfur in an alternate fashion (SILAR method), and varying the temperature. However, most attempts resulted in imperfect particles. In some cases, the poor control over shell growth led to several inappropriate side-processes, such as ripening into larger particles and unidirectional growth of the shell (Figure **8.5**).

In order to improve the reproducibility and provide more control over shell growth, several modifications were made. Diethyl zinc and HMDST, which were used as the precursors of zinc and sulfur, were replaced by zinc stearate and elemental sulfur. Initially, oleic acid and 1-octadecene were used to dissolve the ZnS precursors, as proposed by *Li et al.* [28]. However, zinc stearate and sulfur were soluble in 1-octadecene only at low concentrations and at temperatures above 200°C. In further attempts, oleylamine was used as a solvent. A mixture of OA and OLA was able to solubilize high concentrations of zinc stearate upon stirring at 100°C, while sulfur was highly soluble in OLA even at room temperature.

In Figure **8.6**, the quantum yield, the *FWHM* of emission peak and the Stokes shift are presented as a function of ZnS shell thickness. The evolution of quantum yield during the capping procedure was almost identical to the earlier described capping method in TOPO/HDA solvent, but the absolute values were slightly higher for the OLA-stabilized core/shell quantum dots (Figures **8.3(a)**

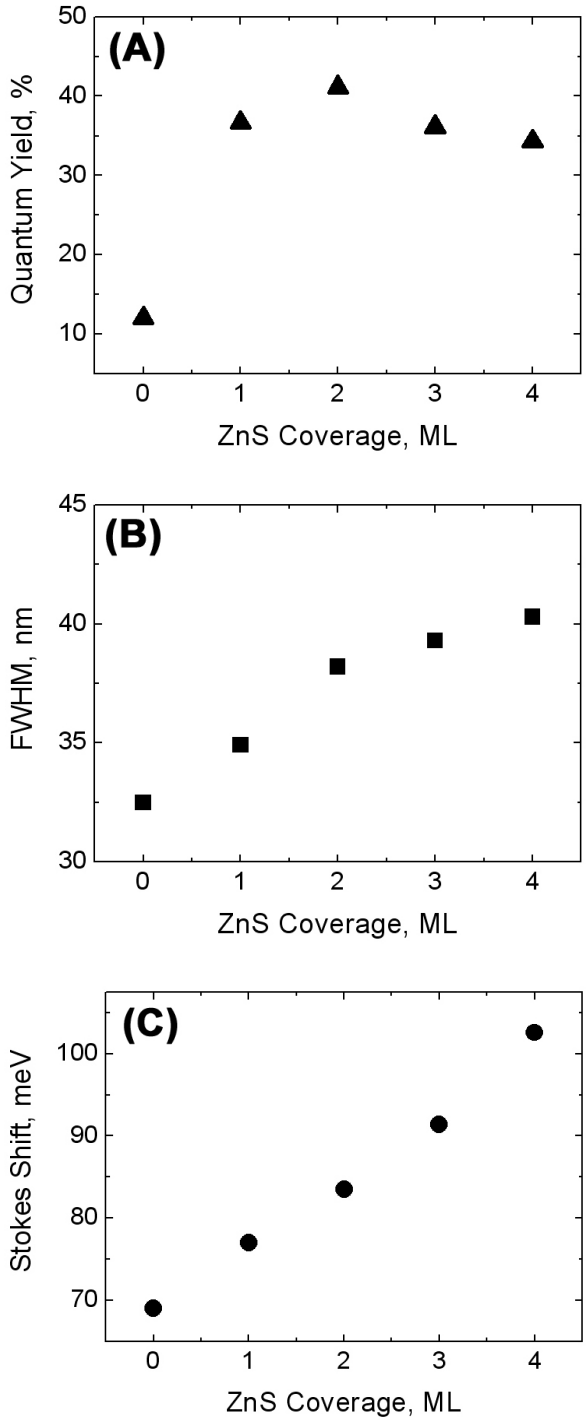

Figure 8.6: Capping CdSe quantum dots with ZnS in the OLA/OA system: (A) Increase of photoluminescence efficiency of CdSe quantum dots. The thickness of approximately 2 ML shows the maximum quantum yield. (B) *FWHM* of the emission showing the CdSe emission peak broadening. (C) Evolution of the Stokes shift of CdSe quantum dot.

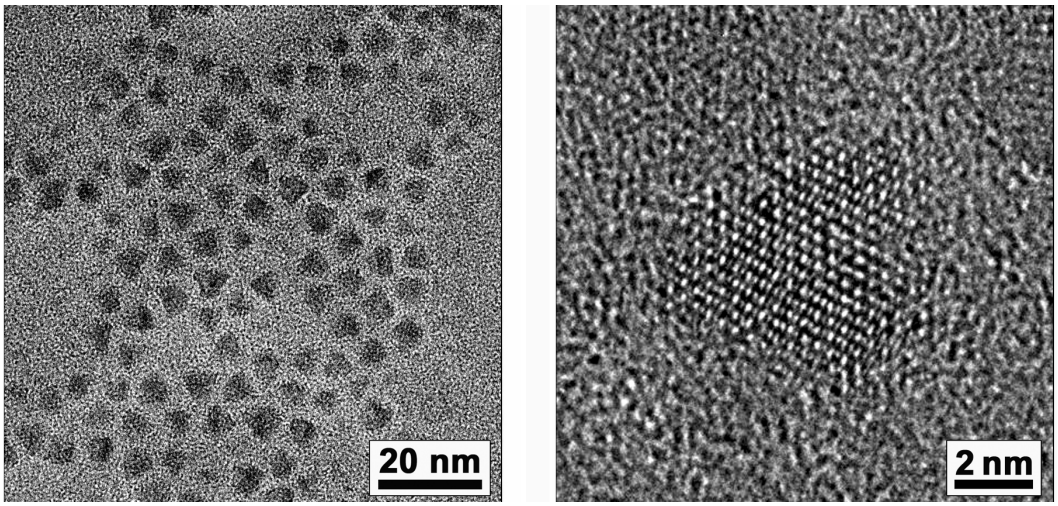

Figure 8.7: High resolution TEM images of CdSe quantum dots capped with ∼5 ML of ZnS in the OLA/OA system.

and **8.6(a)**). The growth of only 1 ML of ZnS in OLA increased the quantum yield from 12% to 37% (Figure **8.6(A)**). The observed increase might also be contributed to by the effect of amines on photoluminescence efficiency, as described earlier. Similar to capping in TOPO/HDA, the highest quantum yield was observed at 2 ML of ZnS, followed by a slight decrease (Figure **8.6(A)**).

Compared to TOPO/HDA, a considerable broadening of the emission peak was observed upon capping CdSe in OLA (Figure **8.6(B)**). The growth of 4 ML of ZnS on CdSe cores resulted in almost a 10-nm increase in the *FWHM* of the emission spectrum (Figure **8.6(B)**). Because of the weaker coordination of the primary alkylamine surfactant, OLA, compared to the branched alkylphosphine oxide, TOPO, faster and less-controlled shell growth occurred, resulting in a greater size distribution of the resulting core/shell quantum dots.

Finally, almost a 35-meV increase in the Stokes shift was observed for CdSe capped with 4 ML of ZnS using OLA (Figure **8.6(C)**). In contrast to using TOPO/HDA, no saturation of the Stokes shift was observed after 3 ML for OLA-stabilized core/shell quantum dots, the Stokes shift even seemed to increase slightly more at this shell thickness (Figure **8.6(C)**). Such a drastic increase could result from the different crystal structure of the shell. Like CdSe grown in OLA, ZnS shell also has a zinc blende crystal structure, which was confirmed by pyramidical shape of resulting core/shell nanocrystals as seen in the high resolution electron micrographs shown in Figure **8.7**. The ZnS shell clearly grew in a zinc blende symmetry, while the core retained its wurtzite crystal structure (Figure **8.7**). The considerably higher lattice mismatch between wurtzite CdSe and zinc blende ZnS may explain the large observed shell thickness effect on the Stokes shift.

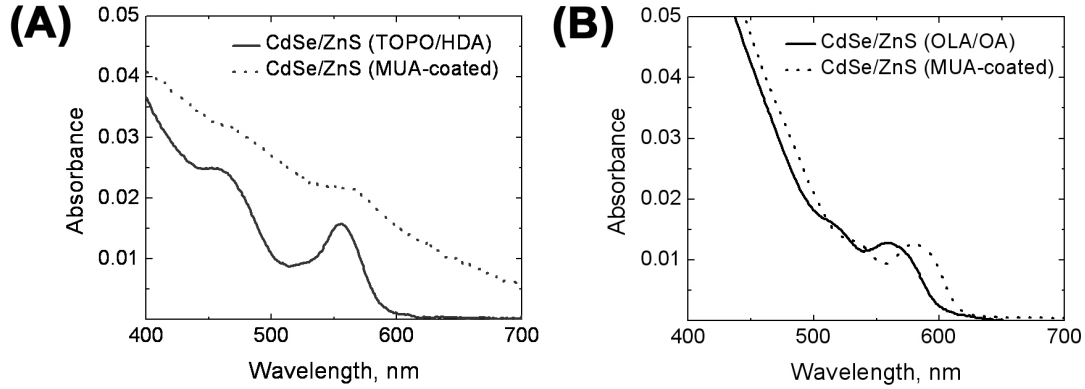

Figure 8.8: (A) Absorption spectra of CdSe quantum dots capped with ZnS in TOPO/HDA: in toluene (solid line) and in water after 18 h of exchange with MUA (dotted line). (B) Absorption spectra of CdSe quantum dots capped with ZnS in OLA/OA: in toluene (solid line) and in water after 10 min of exchange with MUA (dotted line).

Aside from the different crystal structure of the shell and the quantum yield enhancement effect described above, the use of OLA introduced an advantage for functionalization of the quantum dots. Typically, in order to obtain water-soluble nanoparticles stabilized by 11-mercaptoundecanoic acid from TOPO/HDA-coated CdSe/ZnS quantum dots, approximately 24 h of ligand exchange was needed (see Section **10.1.2**). If a shorter duration of exchange was used for the TOPO/HDA-coated quantum dots, it resulted in quantum dots that were only partially soluble in water containing aggregates and displayed large scattering in the absorption spectrum presented in Figure **8.8**. However, it took only 10 min to replace the OLA with mercaptoalkylacid molecules on the quantum dot surface and to produce highly water-soluble particles with a well-resolved absorption spectrum (Figure **8.8**). The observed effect can be explained by the stronger coordination of TOPO to the quantum dot surface [16] compared to OLA.

8.3 Conclusions

From several synthetic methods described in the literature [2, 30, 17], a combined technique was developed and optimized in order to reproducibly obtain monodisperse CdSe quantum dots with quantum yields $\Phi = 10 - 20\%$ using a TOPO-HDA surfactant system. By means of high resolution TEM the structure of the resulting nanoparticles was determined to be wurtzite with approximate lattice parameters $a_0 = 3.98$ Å and $c_0 = 6.93$ Å. The obtained values correspond with both computational and experimental data obtained for bulk CdSe crystals in wurtzite symmetry of about $a_0 = 4.3$ Å and $c_0 = 7.01$ Å [103, 104], providing

additional evidence of the high crystallinity of the quantum dots (Figure **8.1(B)**). Further modification of the synthesis, used an inexpensive and easy method to obtain zinc blende CdSe quantum dots simply by replacing the growth media. Introducing a new ligand, oleylamine, resulted in the growth of CdSe nanoparticles with zinc blende structure, confirmed by the lattice parameters obtained from TEM (nearest neighbor distance measured = 0.23 nm) and the lack of crystal field splitting in the absorption spectrum (Figure **8.2**). Compared to the TOPO/HDA system, the OLA-stabilized CdSe quantum dots displayed approximately two-fold higher photoluminescence efficiency.

In order to enhance the optical properties of the obtained CdSe nanoparticles, we have characterized and modified the conventional approach [26, 17]. The optimized method allows us to synthesize monodisperse core/shell CdSe/ZnS quantum dots with photoluminescence efficiencies of about 35%. Alternatively, an approach using OLA as a surfactant and the use of different reagents sources and injection solutions was developed and characterized. Using this technique it was possible to achieve almost 100% reproducibility in the capping process, eliminate side reactions, and enhance the photoluminescence quantum yield to ∼50%. Moreover, the lower affinity of OLA to the quantum dot surface facilitated a faster water-solubilization by shortening the ligand exchange reaction duration from 24 h to 10 min. High resolution transmission electron microscopy revealed a growth of the ZnS shell with zinc blende lattice structure in OLA, while the core retained its original hexagonal symmetry (Figure **8.7(B)**). Although it is generally assumed that the shell structure is determined by the core [25], the observed effect implies that the key factor of nanocrystal growth is stabilization by surfactants. A more detailed investigation of the electronic and optical properties of core/shell nanoparticles with mixed crystal structures would be of particular interest for physicists and physical chemists.

Chapter 9

Fluorescence Intermittency of Quantum Dots as a Function of Capping

Fluorescence blinking of single quantum dots under constant illumination has attracted a great deal of attention from both experimentalists and theoreticians. To explain the power-law behavior in the distribution of *"on"* and *"off"* times, several models have been proposed, in which the charge carrier is either ejected from the quantum dot to an external trap or is localized at a trapping site within the quantum dot. To gain insight into the blinking mechanism, it is necessary to investigate the role of the shell of CdSe/ZnS core/shell quantum dots [105].

9.1 Sample Characterization

Two sets of samples with different initial quantum yields of the core were taken for the experiment. The thickness of the shell was systematically varied for both samples and the blinking behavior of a statistically significant number of single quantum dots was analyzed and compared.

9.1.1 Capping CdSe Quantum Dots with ZnS

The increase in the ZnS shell upon capping was monitored by TEM and optical spectroscopy. In Figure **9.1**, example TEM images are shown, illustrating the spherical shape and excellent size homogeneity of the uncapped nanoparticles. The quantum dots retained their spherical shape after capping, indicating uniform growth of the shell around the cores. However, due to uncontrolled growth, the capped nanoparticles displayed a greater size dispersion that the uncapped particles (Figure **9.1**). From the magnified single particles in the insets, it is evident that the particle size clearly increased upon adding ZnS. Due to the low

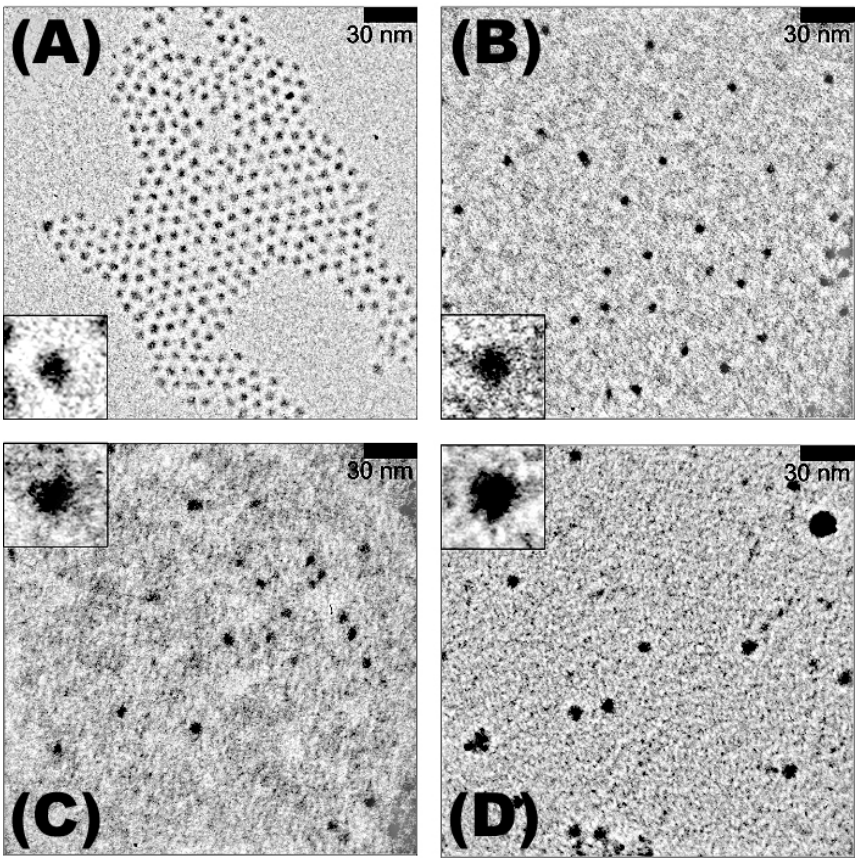

Figure 9.1: TEM images of (A) uncapped CdSe and (B) - (D) upon capping with increasing amounts of ZnS. For each image, the magnification is 190,000. The insets show a single particle in 4-fold magnification (inset size is 15 nm × 15 nm).

contrast of the TEM images of uncapped particles (Figure **9.1(A)**), the particle boundary was blurred and it was difficult to obtain an accurate average size. In order to characterize the diameters of uncapped quantum dots, we used the systematic calibration of CdSe sizes measured by high resolution TEM with their absorption and emission spectra published by *Peng et al.* [106]. The average size of the uncapped CdSe nanoparticles increased, upon capping with ZnS, from 2.9 nm to 4.6 nm in Figure **9.1(B)** (equal to 2.6 monolayers of ZnS), 5.0 nm in Figure **9.1(C)** (3.5 monolayers of ZnS) and 7.2 nm in Figure **9.1(D)** (7.0 monolayers of ZnS).

Capping of CdSe quantum dots with ZnS also altered their optical properties. The observed increase in the *FWHM* and the red shift (up to 8 nm) of the emission spectra, as well as the increase of the photoluminescence efficiency with the ZnS shell thickness, additionally confirmed the epitaxial growth of ZnS shell, as shown in Figure **9.2(A-D)**. Sample 1 had a quantum yield of 20% before capping, increasing to 44% after addition of 3.5 monolayers of ZnS and slightly decreasing

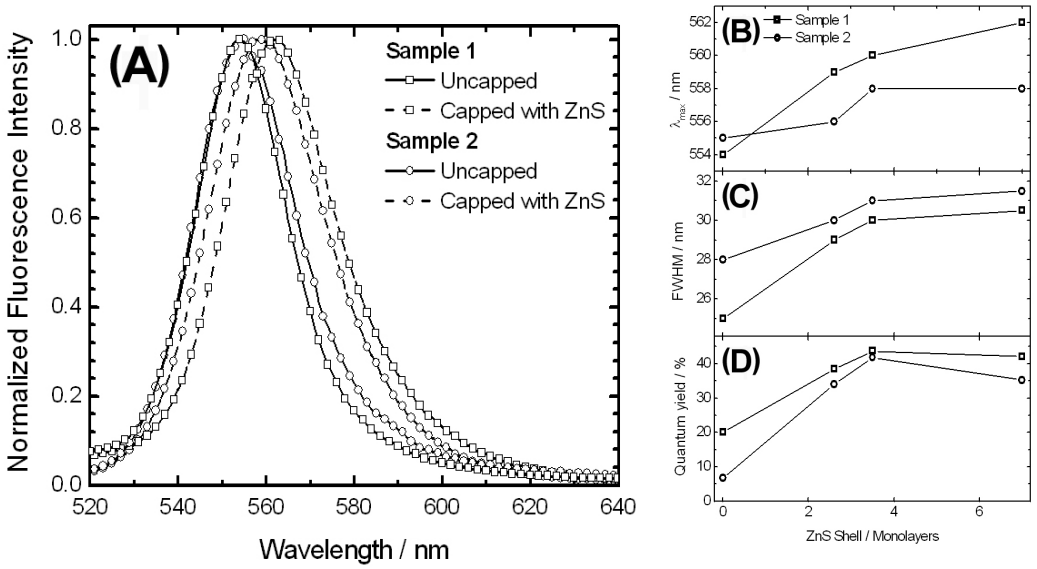

Figure 9.2: (A) Fluorescence spectra of two samples of uncapped and ZnS-capped CdSe QDs (after adding 7 monolayers of ZnS to the cores). (B), (C) and (D) fluorescence λ_{max}, FWHM and quantum yield, respectively, as a function of ZnS added to the CdSe cores.

upon introducing more ZnS. Sample 2 had a quantum yield of 7% before capping, reached 41% after adding 3.5 monolayers of ZnS and then decreased to 35% at 7 monolayers. The observed behavior was described in Section **8.2**. The key variables in our study were the core quality and the shell thickness, both of which were independently varied.

9.2 Data Analysis

9.2.1 *"on"*/*"off"* Times Distribution

The "*on*" and "*off*" times distributions were extracted for each quantum dot preparation at an excitation power of 400 W/cm^2. Figure **9.3** presents typical distributions of the "*on*" and "*off*" times. The total duration of the traces from which the distributions were extracted was 550 s at 100 ms resolution, allowing an analysis window between 300 ms and 50 s. Traces were also measured for 275 s with 50 ms resolution, allowing the window to be shifted to shorter times accordingly. The "*off*" times distributions can be fitted with a power law, as shown previously [44, 7, 49, 50, 51]

$$p_{off} = At^{\alpha}, \tag{9.1}$$

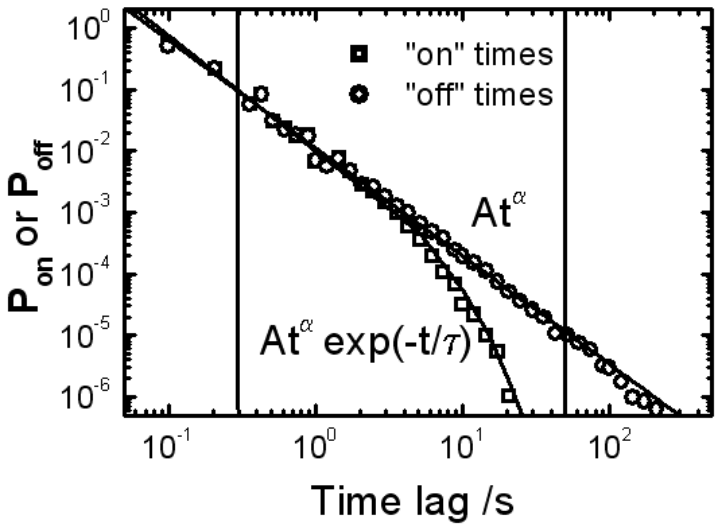

Figure 9.3: Typical "*on*" and "*off*" time distributions showing a power law behavior of the "*off*" times and a power law with exponential cut-off for "*on*" times. The vertical lines represent the analysis window based on the time binning and the trace length.

where α is the power law exponent, and A is a scaling coefficient. The "*on*" times were fitted with a power law with an exponentially decaying tail, thereby limiting very long "*on*" times [56, 57],

$$p_{on} = At^{\alpha} \exp\Big(-\frac{t}{\tau}\Big). \tag{9.2}$$

Here, τ is the relaxation time of the exponential tail.

The "*on*" and "*off*" times distributions for different capping thicknesses are compared in Figure **9.4**. Both samples show a slight scatter in the slopes and in the exponential tails, but no systematic variation with capping thicknesses up to 7 ML of ZnS (Figure **9.4**).

The power law slopes, α, for the "*on*" and "*off*" times and characteristic time τ, are plotted as a function of capping thickness in Figure **9.5**. The averages over all values of these parameters are shown as thick lines on the graphs, passing though the error bars for the majority of points (α_{ave}^{off} = -1.6 ± 0.1) and α_{ave}^{on} = -1.9 ± 0.1). For the "*on*" times, the exponential role-off was characterized by $\tau \approx 5.5 \pm 1.4$ s. Interestingly, these parameters were independent on both sample quality and shell thickness, and the slopes of linear least-squares fits to the extracted blinking data as a function of shell thickness were all close to zero (Figure **9.5**). Therefore, α and τ did not depend on the presence or thickness of the ZnS shell. The same power law exponent for uncapped and ZnS capped CdSe was also reported by *Shimizu et al.* [7], however, we have not observed an increase of the exponential cutoff tail characteristic time, τ, upon capping with

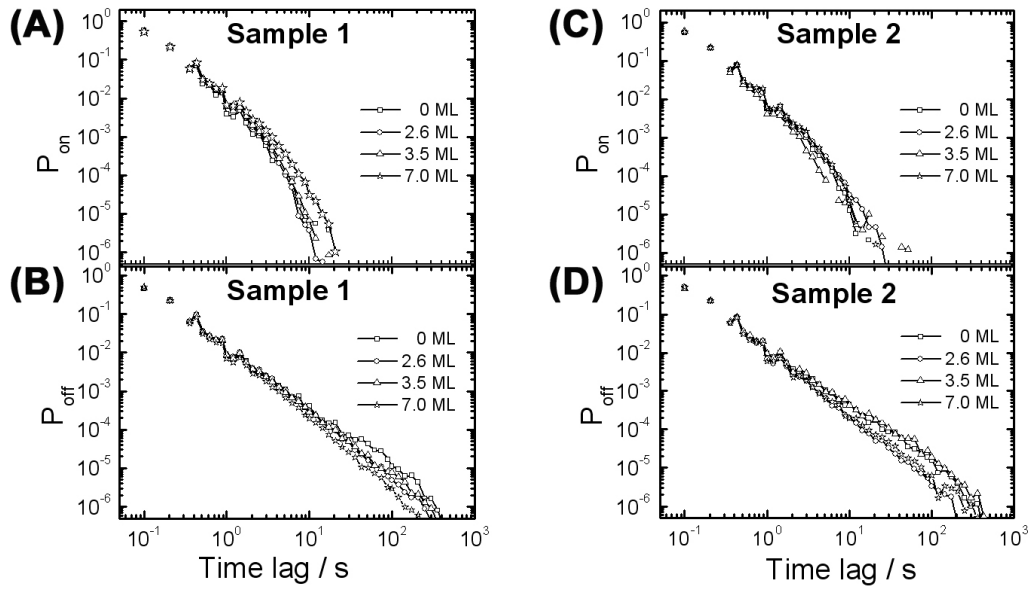

Figure 9.4: *"on"* and *"off"* times probability distributions for sample 1 (A, B) and sample 2 (C, D) with varying amounts of ZnS shell added to the CdSe cores.

ZnS.

Remarkably, the parameters α and τ for both samples were identical within the experimental uncertainty, suggesting that the overall quantum yield of the CdSe cores was not related to the blinking statistics. The increase in bulk quantum yield observed either with higher quality cores or upon shell growth must originate from an increase either in the fraction of bright particles or average quantum yield of the individual emitting particles. It has been noticed previously that single fluorescing quantum dots have much higher quantum yields than the ensemble quantum yield of the sample they were taken from [107], and that a quantum dot sample contains a fraction of non-emitting quantum dots [107, 108, 109]. A direct correlation between the observed bright fraction and ensemble quantum yield for commercially available streptavidin-coated polymer-encapsulated core-shell quantum dots was recently found [108]. We have calculated the average count rate of the ensemble of single quantum dots in the "on" state, $\langle I \rangle_{on}$, at constant laser excitation power (400 W/cm^2),

$$\langle I \rangle_{on} = \frac{\sum NI}{\sum N} \tag{9.3}$$

Here, I is the intensity of a given time bin above the threshold intensity of 70 Hz and N is the number of bins with that intensity integrated over all quantum dots investigated. In Figure **9.6**, $\langle I \rangle_{on}$ is plotted as a function of the ensemble

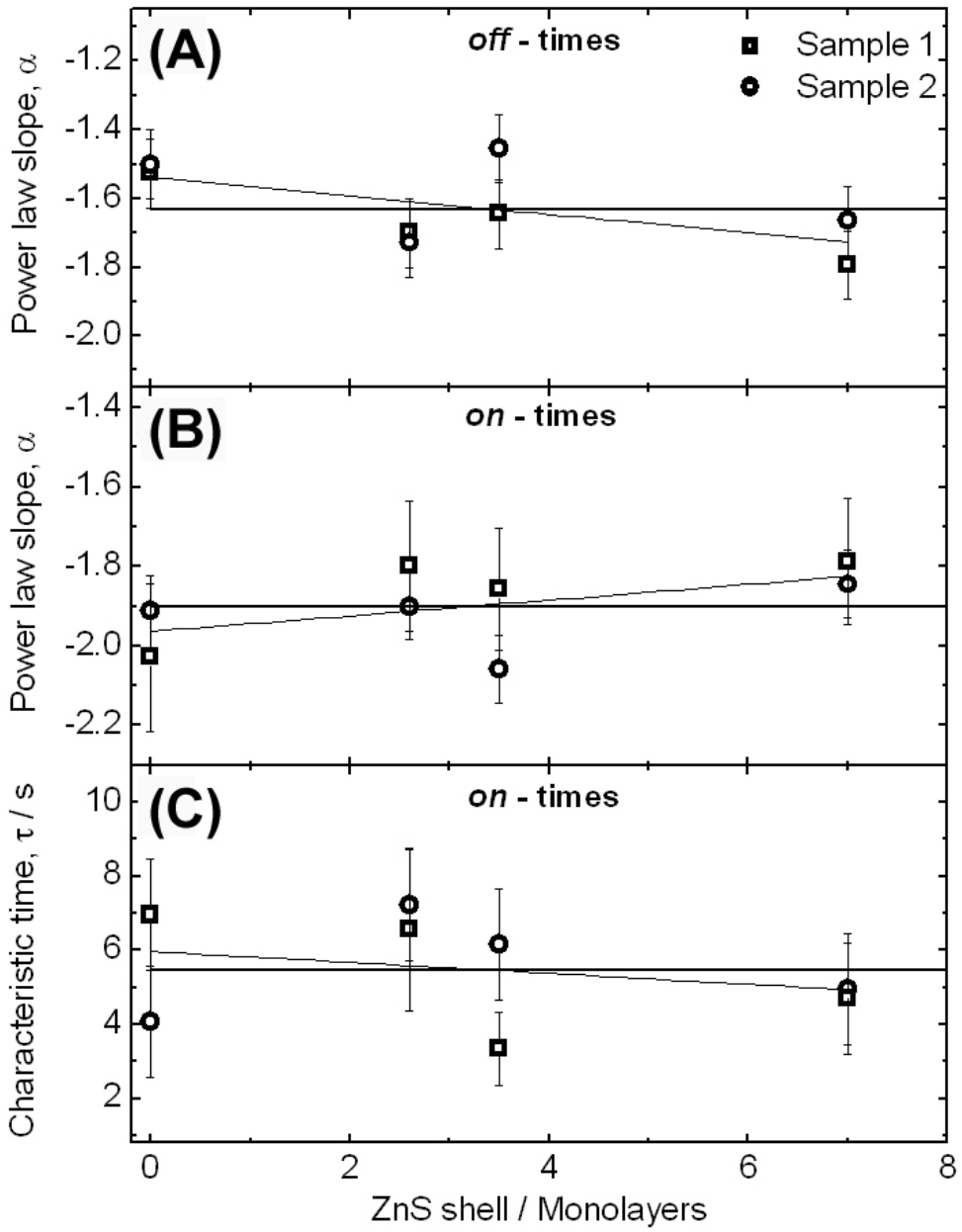

Figure 9.5: (A) Power law slope of the *"off"* times distribution, (B) power law slope of the *"on"* times distribution and (C) characteristic time of the exponential cut-off in the *"on"* times distribution with varying amounts of ZnS shell added to the CdSe cores. The thick lines show the average obtained from all data points. The thin lines are linear least-squares fits to the data. The slopes obtained from these fits are, for panel A: -0.0270 ± 0.0153, B: 0.02015 ± 0.0113 and C: -0.14760 ± 0.209173.

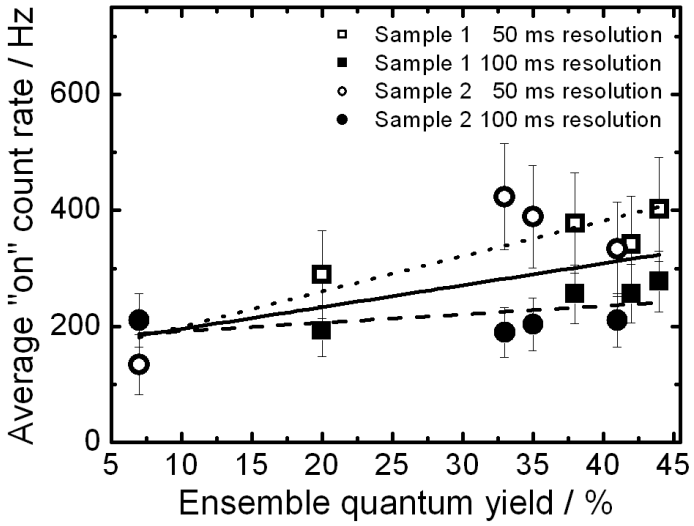

Figure 9.6: Dependence of the average "*on*" count rate, $\langle I \rangle_{on}$, on the ensemble quantum yield for traces measured with 50 ms resolution and 100 ms resolution. The solid line is the a of all points; the dashed and dotted lines are fits of only the 100- and 50-ms data, respectively.

quantum yield of the quantum dot preparation. A relatively large distribution of *"on"* intensities was caused by the random distribution of quantum dots within the 1 μm thick PMMA film, exposing them to varying strengths of the evanescent field. The average intensity of the *"on"* state was slightly dependent on the ensemble quantum yield, as seen from the Figure **9.6**. The slope of the average *"on"* intensity versus ensemble quantum yield was also dependent on the time binning, which was expected, since longer time binning averages out fast blinking events, reducing the average counts per second. However, even for the data binned in 50-ms intervals, a two-fold increase in quantum yield only increased the average "*on*" count rate by a factor of 1.4. These results lend further support to the claim that the ensemble quantum yield is correlated largely to changes in the ratio of radiant (bright) to non-radiant (dark) quantum dots in the sample and only slightly to the individual-particle quantum yield [107, 108].

9.2.2 Mechanism of Fluorescence Intermittency

For a blinking mechanism, based on electron tunneling through the shell to or from an external trap, an exponential decrease in the tunneling rate with shell thickness should be expected, leading to longer "*on*" and "*off*" times for the quantum dot emission [110]. However, the absence of systematic effects of the shell thickness on the quantum dot blinking statistics, presented in Figure **9.5**, suggest that electron tunneling is unlikely as a key mechanism for the intermittency in photon emission. This observation is in agreement with the reported

lack of sensitivity of blinking to the quantum dot environment [54]. By the same argument, we can argue that there is no tunneling to the external surface of the quantum dot shell.

The model proposed by *Shimizu et al.* [7] considers a random walk of a system in a dynamic phase space through a transition point separating dark and bright states. During the long "*off*" times, the system is too deep within the non-emitting, charged state of the phase space to reach the emitting neutral state, while, on the other hand, close to the transition point, the system can rapidly switch between the charged and neutral states [7]. Diffusion of the transition point, as deduced from spectral diffusion experiments [48], leads to power law statistics in the probability distributions. The exponential cut-off tail in the "*on*" times was suggested to be the result of a secondary mechanism, such as photoassisted charge ejection due to *Auger ionization* followed by external trapping, whereas the increase in the characteristic time of the exponential cut-off, τ, for capped quantum dots observed by *Shimizu et al.* [7] was proposed to originate from a reduction in the number of trap states by capping.

Developing this idea further without using external trap states, *Frantsuzov and Marcus* [57] recently introduced a model that we have applied to explain our data [105]. A principal constituent of the model is the presence of multiple hole trap states above the $1S_{3/2}$ valence band level, which have been previously observed by infrared absorption spectroscopy, even for ZnS-capped quantum dots [111] (Figure **9.7**). The width of the band associated with these hole states was found to be ∼200 meV, with the first trap state lying ∼300 meV above the $1S_{3/2}$ state [111] (Figure **9.7**). A 3 nm-diameter CdSe quantum dot consists of approximately 1000 Cd and Se atoms, with at least 200 Se atoms on the surface. *Frantsuzov and Marcus* assumed that there is one dangling bond per Se atom, since TOPO binds primarily to Cd [65, 112], resulting in ∼200 trap states, each separated by 1 meV, per quantum dot. Upon excitation, the hole can be trapped in one of these states, transferring the released energy to the excited electron, which is promoted from the $1S_e$ to $1P_e$ energy level by an Auger mechanism (Figure **9.7**). The $1P_e$-$1S_e$ energy gap, ε_0, was experimentally determined as ∼300 meV, with a width of ∼140 – 220 meV depending on quantum dot size [113].

In the model, the $1P_e$-$1S_e$ gap undergoes light-induced stochastic fluctuations, with a Gaussian probability distribution of the transition energy, ε, with time [57]. In Figure **9.7**, the fluctuating conduction band levels from which the transition energy fluctuations originate are depicted schematically. Evidence supporting such diffusive energy fluctuations is provided by measurements of the homogeneous linewidth of the band associated with the $1P_e$-$1S_e$ transition of ∼3 meV [114], whereas the observed width is ∼200 meV [113].

Auger-assisted hole trapping requires matching energy gaps for the electron and hole transitions, and so the rate of hole trapping strongly depends on the energy fluctuations. The expression for the hole-trapping rate, k_t, based on

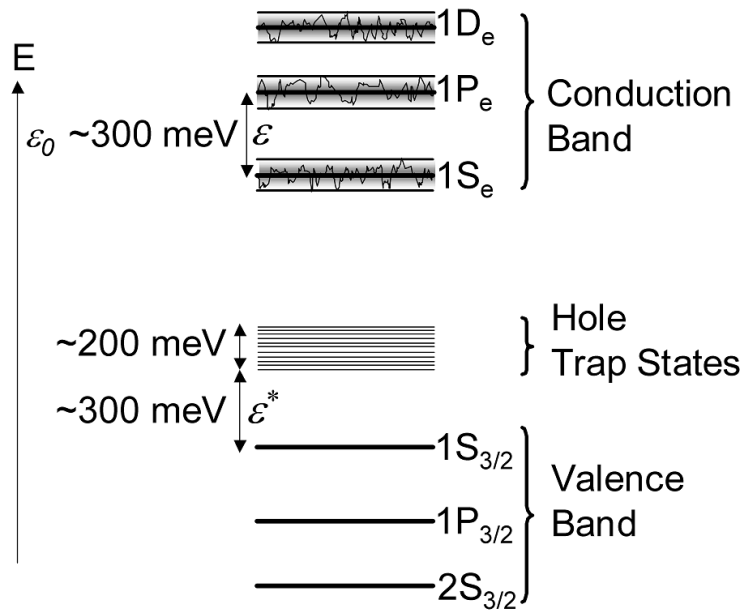

Figure 9.7: Energy level diagram of the CdSe states used in the model of *Frantsuzov and Marcus* [57] to explain power law blinking kinetics without external traps. Diffusion of the conduction band energy levels is represented as a band with its energy randomly fluctuating with time (thin jagged line within the shaded band).

Fermi's golden rule, is essentially a step function, as k_t increases over several orders of magnitude within a narrow range of energy, ε, for which the electron energy gap is sufficiently large to match the gap between the $1S_{3/2}$ and the hole trap states. A threshold value of the $1P_e$-$1S_e$ gap, ε^*, denotes the onset of high trapping rates (Figure **9.7**). If the fluctuating energy gap ε is below ε^*, the trapping rate is small and the quantum dot fluoresces. Conversely, if the gap fluctuation is above ε^*, the trapping rate is large, and the quantum dot is quenched. Assuming that the energy fluctuations obey the diffusion equation, the theory yields a power law dependence of both the "*on*" and "*off*" times distribution with $\alpha = -1.5$, with an exponential cut-off at times longer than the diffusional relaxation time, τ_D, given by [57]

$$\tau_D = \frac{\Delta^2}{D} \tag{9.4}$$

where Δ^2 is the variance of the distribution of ε (~50 meV), and D is the diffusion coefficient. *Chung et al.* reported the cut-off time of the power law distribution of the "*off*" times of ~1000 s [115], while our results indicated that the cut-off time for the "*on*" times is ~6 s, in agreement with data previously reported [7]. We have observed a power law exponent of –1.6 for the "*off*" times distribution, in excellent agreement with *Frantsuzov-Marcus* theory [57]. However, for the "*on*"

times distribution our exponent (–1.9) is significantly larger than the theoretical value of –1.5. It has been argued that the power law exponent of the "*on*" times may be sensitive to the quantum dot environment or sample preparation.

9.2.3 Blinking Statistics upon ZnS Capping

Our experimental results indicate that the power law exponents of both the "*on*" and "*off*" times, and the exponential cut-off of the "*on*" times are independent of ZnS capping and independent of the ensemble quantum yield of the CdSe core particles. This result can be explained as follows: The average number of trap states has been shown to decrease upon capping CdSe quantum dots with ZnS [24, 25, 26, 101]. However even for ZnS capped nanoparticles, infrared spectroscopy has revealed the presence of a relatively large number of surface trap states [111]. It is reasonable to assume that the number of trap states and the energy between the $1S_{3/2}$ level and the first trap state varies among quantum dots. If a quantum dot has its first trap state at a low energy, then the $1P_e$-$1S_e$ transition energy will always be in resonance with the $1S_{3/2}$ to hole trap transition, and therefore, Auger-assisted quenching will always occur, the quantum dot will be permanently dark. Capping with ZnS results in a larger fraction of quantum dots that have a reduced number of traps above this threshold, decreasing the dark fraction, but there is still a considerable number of hole trap states that can be populated if the $1P_e$-$1S_e$ energy gap crosses the threshold between the "*on*" and "*off*" states, ε^*, causing the quantum dots to blink. Hence, there are two populations of quantum dots in a given sample (1) dark quantum dots that are never "*on*" (dark fraction) and (2) quantum dots that are "*on*" and blinking (bright fraction). The ensemble quantum yield is mainly governed by this ratio.

A slight dependence of the ensemble quantum yield on the average "*on*" intensity was observed from Figure **9.6**, demonstrating that samples with higher overall quantum yield did contain particles with slightly higher individual quantum yield. This effect, however, was not large enough to account for the overall increase in the ensemble quantum yield. A similar result was also observed using correlated AFM and fluorescence microscopy measurements [107].

It may be possible that not all of the trap states in this model are, in fact, surface states. Lattice defects in the core CdSe crystal volume may also contribute to the number of trap states, as is suggested by the fact that quantum dots of the same size can have dramatically different ensemble quantum yields, depending on the method of synthesis. In general, synthesis at higher temperatures (or post-preparative annealing) results in higher quantum yield particles (see Section **8.1**). Reducing the surface defects by capping initially increases the bright fraction until lattice mismatch effects at the CdSe-ZnS interface increases the number of trap states to render the quantum dot dark again. This dependence may explain the observation that forming a ZnS shell thicker than $\sim$4 monolayers results in a slight reduction of the ensemble quantum yield (see Section **8.2**).

9.2.4 Cut-off Tail in the *"on"* Times Distribution

In contrast to our results, *Shimizu et al.* [7] reported a slight dependence of the exponential cut-off time upon capping CdSe with 6 ML of ZnS. However, from their experimental data the power law exponent for the uncapped and ZnS capped quantum dots were clearly identical, within experimental error, and only the cut-off time was affected by capping. Various explanations have been invoked to address why the cut-off time from power law statistics is much shorter (∼2 to 3 orders of magnitude) for the "*on*" times than the "*off*" times [7, 51, 56, 57]. Two arguments were derived from the model of *Frantsuzov* and *Marcus* [57]. One hypothesis is that the diffusion coefficient, D, of the stochastic motion of the $1P_e$-$1S_e$ transition in the "*on*" state is higher than in the "*off*" state, effectively leading to deviations from the idealized gaussian probability distribution function of ε. Based on the values of τ_D reported previously for the *"off"* times [115] and for the *"on"* times reported here, D ∼2.5 meV^2/s for the "*off*" state and ∼410 meV^2/s for the "*on*" state. This large difference may be the result of more pronounced rearrangements of atoms or bonds in the excited state relative to the ground state. Another possibility is that the $1D_e$-$1S_e$ transition (see Figure **9.7**) also undergoes stochastic diffusion. If the $1P_e$-$1S_e$ transition energy is significantly reduced, then the $1D_e$-$1S_e$ energy may come into resonance with the hole trap state energy, resulting in a second Auger-assisted trapping route, effectively reducing the probability of observing longer *"on"* times. The effect of the shell was not explored by *Frantsuzov* and *Marcus* [57]. The observed increase in the cut-off time of the *"on"* times in ZnS capped quantum dots reported by *Shimizu et al.* [7] could be a result of their capping procedure reducing the number of trap states to a low enough number that the first trap state is high enough above 300 meV that stochastic diffusion of ε with time crosses ε^* less frequently (i.e., ε^* is moved up in energy with respect to ε_0), whereas the quantum dots capped in our lab may still have many traps at the core-shell interface. However, the dependence of the displacement of ε^* from ε_0 on the power law exponent has not yet been investigated in the proposed model. In the model of *Shimizu et al.* [7], which contains the possibility of external trapping, limiting the amplitude of the diffusion of the transition point between bright and dark states would have a similar effect on the "*on*" times exponential cutoff as the model of *Frantsuzov* and *Marcus* [57]. It is interesting to note that *Kuno et al.* [51] found no exponential cutoff at all in the "*on*" times distribution of their CdSe particles under even higher excitation power densities than those used here and by *Shimizu et al.* [7]. The variation in power-law exponents and exponential cutoff behavior reported for the "*on*" times by different groups may reflect either a dependence on quantum dot preparation of the position of the first trap state (estimated at ∼300 meV above $1S_{3/2}$), effectively leading to a displacement of ε^* with respect to ε_0, or the position and diffusion of the $1D_e$ state offering a second Auger route to quench the fluorescence, as discussed above.

9.3 Conclusion

In summary, the lacking dependence of quantum dot blinking statistics on the shell thickness of CdSe-ZnS core-shell quantum dots observed is inconsistent with tunneling to an external trap. The recent model of *Frantsuzov and Marcus* [57] was used to explain the statistical behavior of quantum dot blinking. By extending the model to the idea of a threshold number of trap states rendering the quantum dot either "permanently dark" or "bright and blinking", it is possible to explain the correlation between ensemble quantum yield and bright fraction, including a microscopic description of the increase of ensemble quantum yield upon capping CdSe with ZnS. The exact physical mechanisms underlying the deviations from the power law exponent –1.5 and the cut-off time at which the power law behavior collapses to an exponential behavior have not yet been fully elucidated, although clues have arisen as to their origin, such as possible deviations of the probability density function from gaussian and/or differences in the position and bandwidth of trap states relative to the $1P_e$-$1S_e$ energy gap. By extending these present studies to other quantum dot systems and capping materials, further insight into the physical mechanism governing quantum dot intensity fluctuations will be gained. This knowledge may allow the design and production of non-blinking quantum dots, which are highly desirable for a wide spectrum of applications.

Chapter 10

Functionalization Of Quantum Dots

For applications of quantum dots in the life sciences, it is necessary to achieve biocompatibility of the particles. This is usually accomplished by modifying their surfaces by replacing the initial surfactant stabilizers with various bifunctional organic compounds containing desirable functional groups. Thiolated acids such as mercaptopropionic acid or 11-mercaptoundecanoic acid allow one to obtain water-soluble quantum dots with carboxylate functionality that can be conjugated to biomolecules. However such water-solubilization procedures are often irreproducible and the obtained quantum dots tend to aggregate due to desorption of ligands from the surface as a result of photochemical processes to the ligand. To obtain a stable coating, dense grafting of strongly bound ligands is needed. As a matter of fact, the hydrophobic chains of mercaptoalkylacids can retain a high degree of hydrophobicity to the particle if they are not densely packed on the surface. Therefore, a great deal of time and experience is needed to find reasonable conditions to obtain bright, chemically stable (non-aggregated) water-soluble quantum dots using mercaptoalkylacids. This section describes experiments aimed at gaining a more thorough understanding of the effects of the ligand exchange procedure on the chemical and optical properties of biocompatible quantum dots.

10.1 Carboxylated Biocompatible Quantum Dots

For the preparation of negatively charged, carboxylated water-soluble quantum dots, 11-mercaptoundecanoic acid (MUA) was used. The choice of ligand was based on its affinity to bind transition metals of the II-b group and the relatively long hydrocarbon chain which, if densely packed on the surface, should restrict access of potentially quenching solvent or solute molecules to the quantum dot

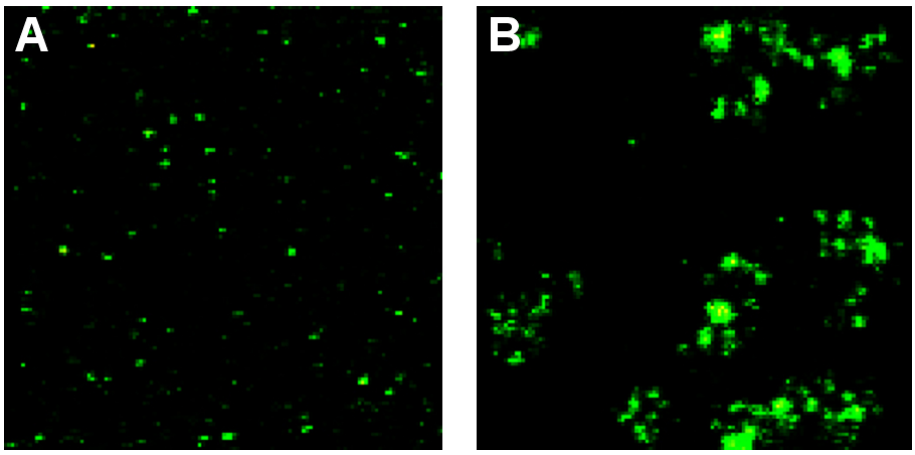

Figure 10.1: Scanning confocal fluorescence microscopy images of immobilized quantum dots solubilized with MUA ligands using (A) 1:1 methanol:dioxane or (B) methanol as the exchange solvent. Images are 18 μm $\times$ 18 μm.

surface. Several other compounds from the homologous series of mercaptoalkylacids, such as mercaptoacetic acid, mercaptopropionic acid, dihydrolipoic acid and mercaptobenzoic acid, have also been tested as possible ligands for the exchange reaction. The resulting water-soluble quantum dots obtained with various ligands had similar properties in terms of chemical stability. However, due to the fact that MUA contained the longest hydrocarbon chain, MUA-coated quantum dots retained maximal photoluminescence efficiency compared to the other ligands.

10.1.1 Conditions for Ligand Exchange

Initial attempts at ligand exchange were performed by refluxing MUA and TOPO/HDA-coated quantum dots in methanol as previously described [62]. However, since methanol is a poor solvent for the initial TOPO/HDA-coated quantum dots, the particles aggregated and only partially redissolved upon MUA exchange. Ultrasensitive scanning confocal fluorescence microscopy, with detection limits down to the single quantum dot level, of a dilute aqueous quantum solution after MUA exchange was performed by mixing the quantum dots with PVA and immobilizing them on a coverslip by spin coating, is shown in Figure **10.1**. It indicates that almost all quantum dots formed aggregates rather than individual, solubilized quantum dots when using methanol as the solvent (Figure **10.1(A)**). Subsequent attempts with a miscible co-solvent mixture of methanol and 1,4-dioxane allowed both the initial quantum dots and the MUA-exchanged quantum dots to remain soluble throughout the exchange. In the co-solvent system, the vast majority of quantum dots exist as single particles (Figure **10.1(B)**), evidenced by well-separated spots of size equal to the point spread function of the

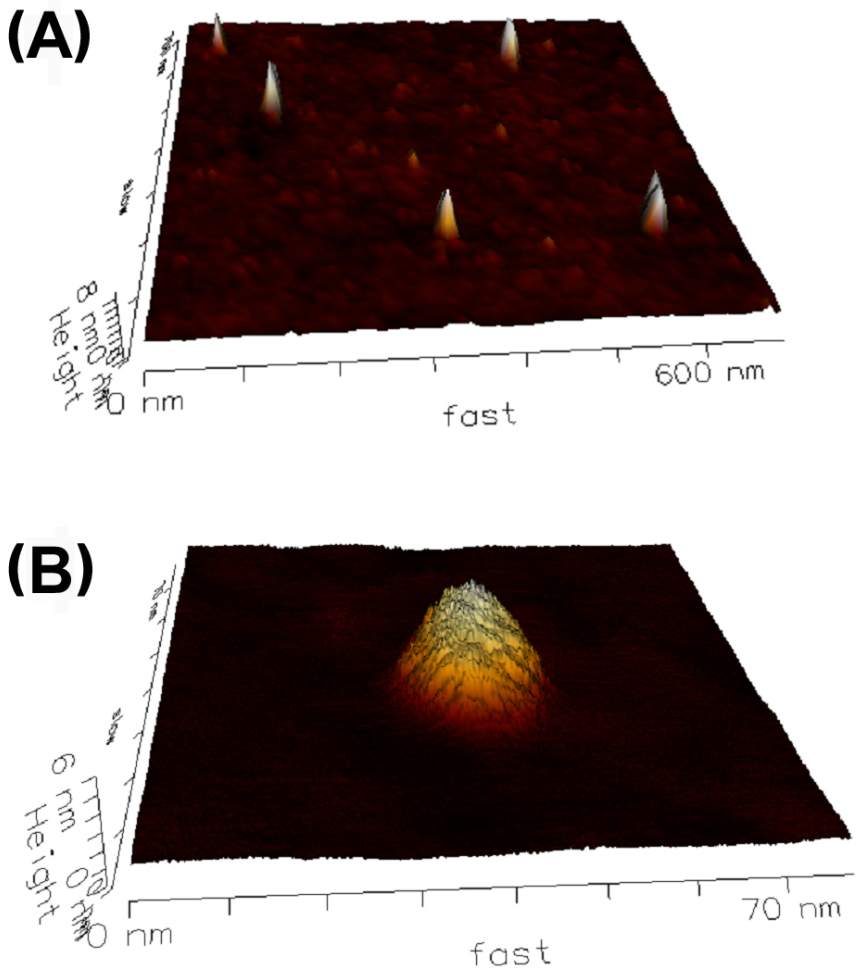

Figure 10.2: (A) 3D AFM topography image of MUA-coated CdSe/ZnS water-soluble quantum dots. (B) A single carboxyl-functionalized quantum dot on a glass surface.

confocal microscope. Due to the blinking of single quantum dots during the scan, spots do not always appear as circular, but often appear as half circles or even just as horizontal stripes [116]. The observation of blinking is additional evidence of single, isolated quantum dots. In support of the confocal fluorescence microscopy evidence, the aggregation of MUA-functionalized CdSe/ZnS quantum dots prepared in the co-solvent systems was also checked using atomic force microscopy (AFM), as shown in Figure **10.2**. The 3D topography images revealed heights of about 6 nm corresponding to single nanoparticles. It is worth noting that some of the aggregates formed in methanol solvent may be too small to precipitate out of solution, and may not be immediately and visibly obvious but are nevertheless useless for further conjugation to biomolecules. An additional purification step

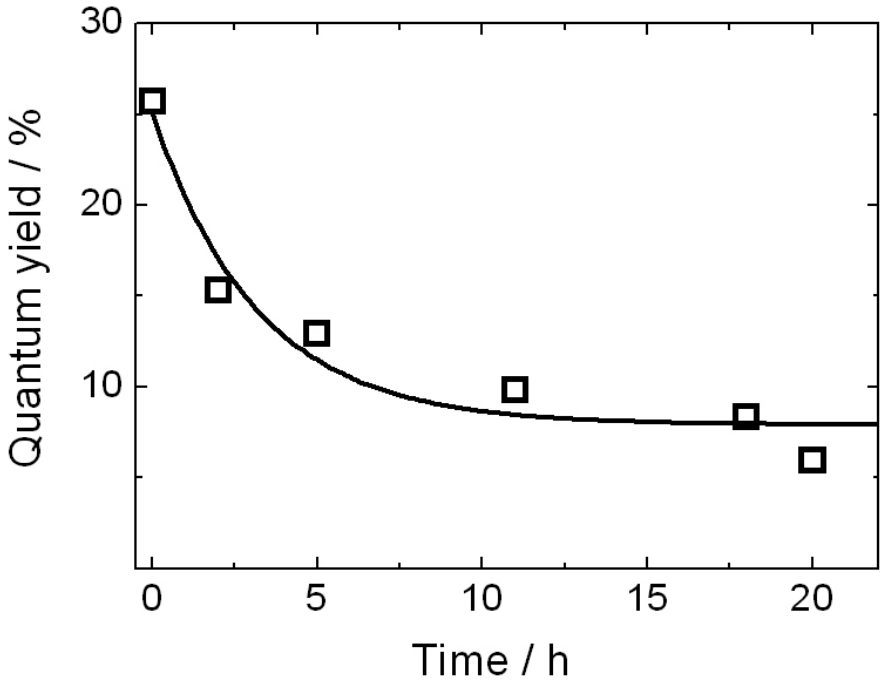

Figure 10.3: Quantum yield of MUA-quantum dots as a function of exchange time for CdSe capped with ZnS at a MUA:quantum dot ratio of 240:1. The data were fitted to an exponential function with a characteristic time of 3.2 ± 1.0 h.

using size exclusion chromatography would be necessary for these samples, which would significantly reduce the overall quantum dot ligand exchange reaction yield.

10.1.2 Kinetics of Ligand Exchange

The time dependence of quantum yield changes during the exchange process is plotted in Figure **10.3**. The quantum yield of the core-shell quantum dots in toluene was initially 25% and decreased exponentially with exchange time to 7% (in aqueous solution), with a characteristic time of 3.2 ± 1.0 h. First samples taken after 2 – 8 h of exchange demonstrated very low colloidal stability and precipitated within 15 – 30 min after dispersion in water. The aggregated flakes of quantum dots failed to redissolve upon heating to 70 – 90°C or increase of pH. Typically, 16 – 20 h was necessary to achieve longer-term stable solutions of water-soluble MUA-coated quantum dots. Similar results were found for other MUA:quantum dot ratios ranging from 80:1 to 240:1 (mass ratios). At ratios below 80:1, we found that quantum dots were insufficiently exchanged to impart water solubility, even after 36 h.

In order to compare the binding affinity of thiols to different surfaces, three different CdSe quantum dot samples with Cd-, Zn-, S-saturated surfaces (pre-

pared by the SILAR capping reaction in TOPO/HDA) (see Subsection **6.1.3**) and a standard CdSe/ZnS core/shell sample with both S and Zn on the surface were taken for ligand exchange. These preparations were functionalized with MUA under identical conditions. The use of Zn- and Cd-saturated surfaces allowed us to obtain stable water-soluble quantum dots after 24 – 32 h of exchange with 100% reproducibility for similarly prepared quantum dots. For S-saturated surfaces, the resulting quantum dots sometimes formed a slightly turbid solution upon transfer into water following 32 h of exchange. The aggregates were left to settle and the stable part was able to be decanted. However, it was difficult to accurately characterize these samples, since the shape of absorption spectra was altered by the addition of the sulfur layer to uncapped CdSe particles. since CdS has a higher bandgap than CdSe. Standard CdSe/ZnS quantum dots with mixed surface composition were successfully exchanged in 30 – 40% of attempts for similarly prepared quantum dots. The surface homogeneity of the Cd-, Zn-, and S-surface-saturated quantum dot samples enabled MUA molecules to bind to only a single type of ions on the surface of the quantum dot. Therefore, the observed difference in colloidal stability corresponded to the different affinities of thiol groups to the specific surface ions. These results indicated a weaker or slower interaction of thiolated molecules with surface sulfur atoms, as expected. Therefore, it is reasonable to conclude that the different affinities of the thiolated ligands to the surface of standard core/shell CdSe/ZnS quantum dots containing mixed surface atoms was responsible for the irreproducible water-solubilization ability of these quantum dots.

10.1.3 Quenching of MUA-coated Quantum Dots

Figure **10.4** presents Stern-Volmer plots of the quantum dots with various thiolated quenching agents. Significant quenching occurred; the quenching efficiency depends both on the size and functionality of the quenching molecule. The small mercaptoacetic acid (MAA) was the most efficient quencher, followed by the larger 3-mercaptobenzoic acid (MBA), then the neutral β-mercaptoethanol (BME) and finally the largest molecule, MUA, the same ligand that was used for the exchange.

From Figure **10.4**, it is clear that quenching is non-linear for MAA, MBA and BME quenchers. This non-linearity suggests that multiple quenching pathways with different quenching efficiencies exist. For two separate quenching sites present, the dependence of I_0/I on [Q] is given by

$$I_0/I = \Big[\frac{f_1}{(1 + K_{SV1}[Q])} + \frac{f_2}{(1 + K_{SV2}[Q])}\Big]^{-1}. \tag{10.1}$$

Here, f_1 and $f_2 = 1 - f_1$ are the fractional contributions of pathways 1 and 2, respectively. K_{SV1} and K_{SV2} are the Stern-Volmer coefficients for each pathway.

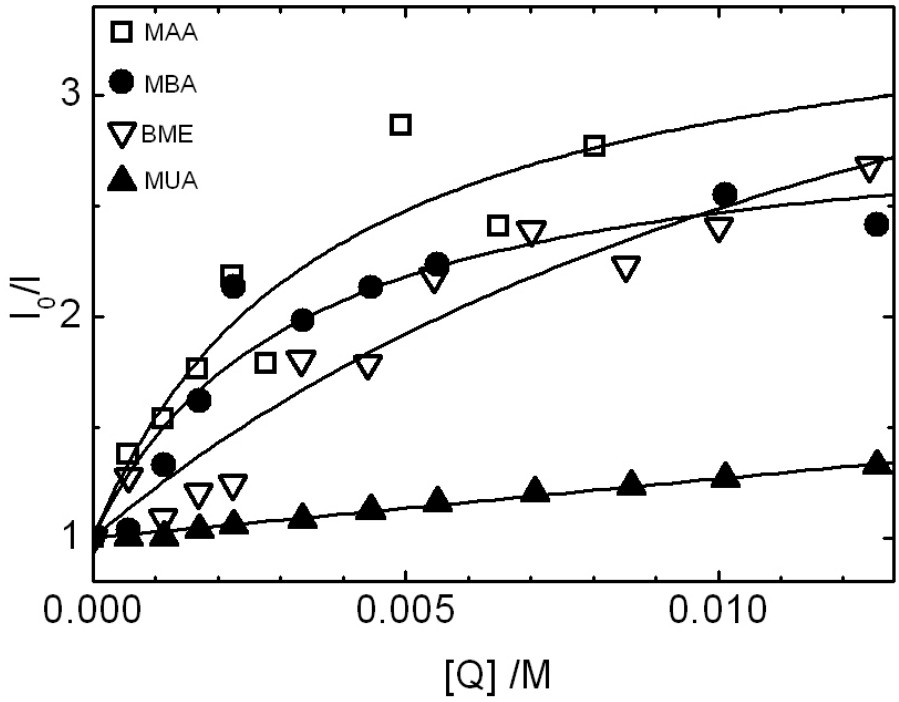

Figure 10.4: Quenching of MUA-quantum dots with various water-soluble thiolated quenchers. A fit of the data with equation **10.2** resulted in the following parameters: MAA: $K_{SV1} = 958$ M^{-1}, $f_1 = 0.72$; MBA: $K_{SV1} = 905$ M^{-1}, $f_1 = 0.66$; BME = $K_{SV1} = 303$ M^{-1}, $f_1 = 0.80$; MUA: $K_{SV1} = 29.1$ M^{-1}, $f_1 = 0.93$.

If one assumes that a single quenching pathway is stronger than the other ones [117], equation 10.1 may be recast as

$$I_0/I = \frac{1 + K_{SV1}[Q]}{(1 + K_{SV1}[Q])(1 - f_1) + f_1}, \tag{10.2}$$

which adequately fits the quenching data of quantum dots with MAA, MBA and BME in Figure **10.4**.

In order to determine the relative effects of the thiol, carboxyl and hydroxyl groups on quenching, the thiolated reagents were compared to their non-thiolated analogues. Figure **10.5(A)** depicts Stern-Volmer plots of MAA and acetic acid (AA) and Figure **10.5(B)** those of BME and ethanol (EtOH). Apparently, in both cases, the thiol group is the primary quenching moiety. However, the carboxylic acid group causes some quenching, whereas the alcohol group provides a negligible contribution. Furthermore, quenching by the carboxylic acid group (in the absence of a thiol group) appears to be linearly dependent on concentration in the range up to 10 mM, indicating a single quenching pathway. The observation of carboxylic acid quenching may explain why both MAA and MBA

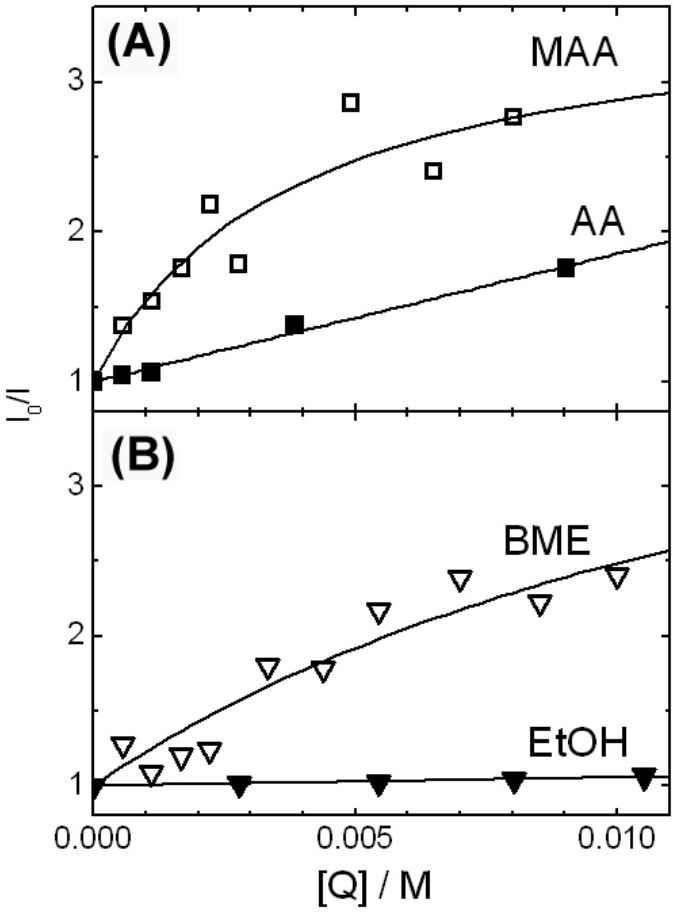

Figure 10.5: Contribution of (A) the carboxylic acid group and (B) the alcohol group to quenching of MUA-coated quantum dots. K_{SV} of AA = 85.5 M^{-1} and for EtOH = 5.62 M^{-1}.

are significantly stronger quenchers than BME, even though MBA is a larger molecule than BME.

Figure **10.6(A)** shows the luminescence lifetime of MUA-coated quantum dots with and without added 9 mM MAA. No change in the luminescence lifetime was evident upon quencher addition. Identical behavior was observed for all quenchers used. The average lifetime of the quantum dot sample as a function of quencher concentration is plotted for various quenchers in Figure **10.6(B)**. This result verifies that a static model rather than a collision model explains the quenching mechanism. Apparently, the quencher complexes to the quantum dot, most likely via the thiol bond, and possibly displaces either MUA ligands or any residual TOPO or HDA ligands.

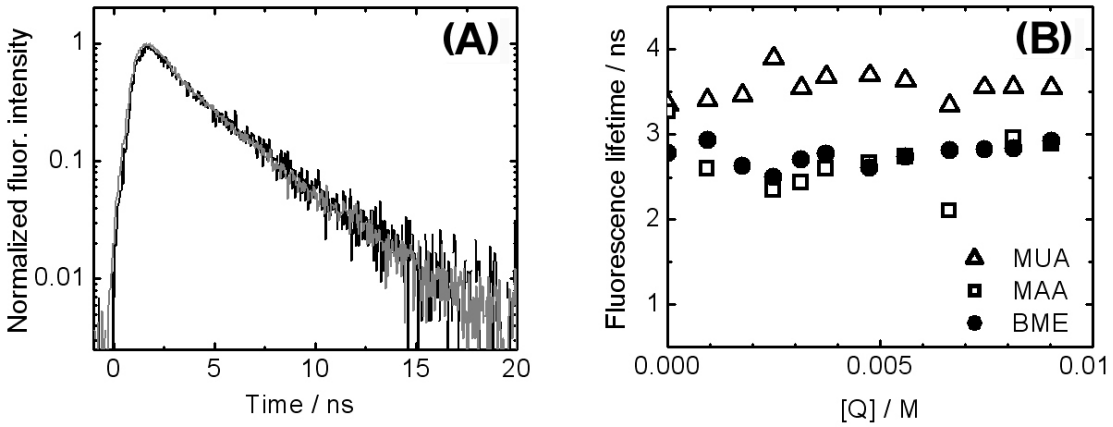

Figure 10.6: (A) Luminescence lifetime of MUA-coated quantum dots with and without 9 mM MAA. (B) Luminescence lifetime as a function of quencher concentration for MAA, BME and MUA.

10.1.4 Photochemical Stability of MUA-Quantum Dots

In order to determine the photochemical chemical stability of MUA-capped quantum dots, we followed the absorption spectra of dilute samples of quantum dots kept under light and dark conditions at room temperature. Precipitation of quantum dots caused them to settle to the bottom of the cuvette and a reduction in the absorption of the first exciton peak was observed. These data are presented in Figure **10.7**. Figure **10.7(A)** shows the changing absorption spectra of the light-exposed quantum dots, while Figure **10.7(B)** highlights that, under darkness, no precipitation occurred, even after 28 days. Figure **10.7(C)** represents the time dependence of the changes in the absorption of the first exciton peak at 565 nm upon exposure to room light or kept under darkness.

10.1.5 Discussion

For thiol-coordinated quantum dots, widely scattering values of quantum yields have been reported in the literature, ranging from less than 1% to more than 50% [8,10,16,27,28]. It has been also discussed that the chemical stability of thiolated alkyl acids is relatively low, and sensitive to storage conditions [62]. We hypothesized that these properties are dependent on the extent of ligand exchange and on the chemical properties of the thiolated ligand. Therefore, we have characterized these parameters by following the kinetics of ligand exchange and its effect on the quantum yield, the ability and mechanism of various water-soluble ligands to quench the emission of the water-soluble core-shell quantum dots, and the chemical stability of MUA-coated quantum dots stored under light or dark conditions.

Exchange of TOPO and HDA with MUA exponentially reduced the quantum

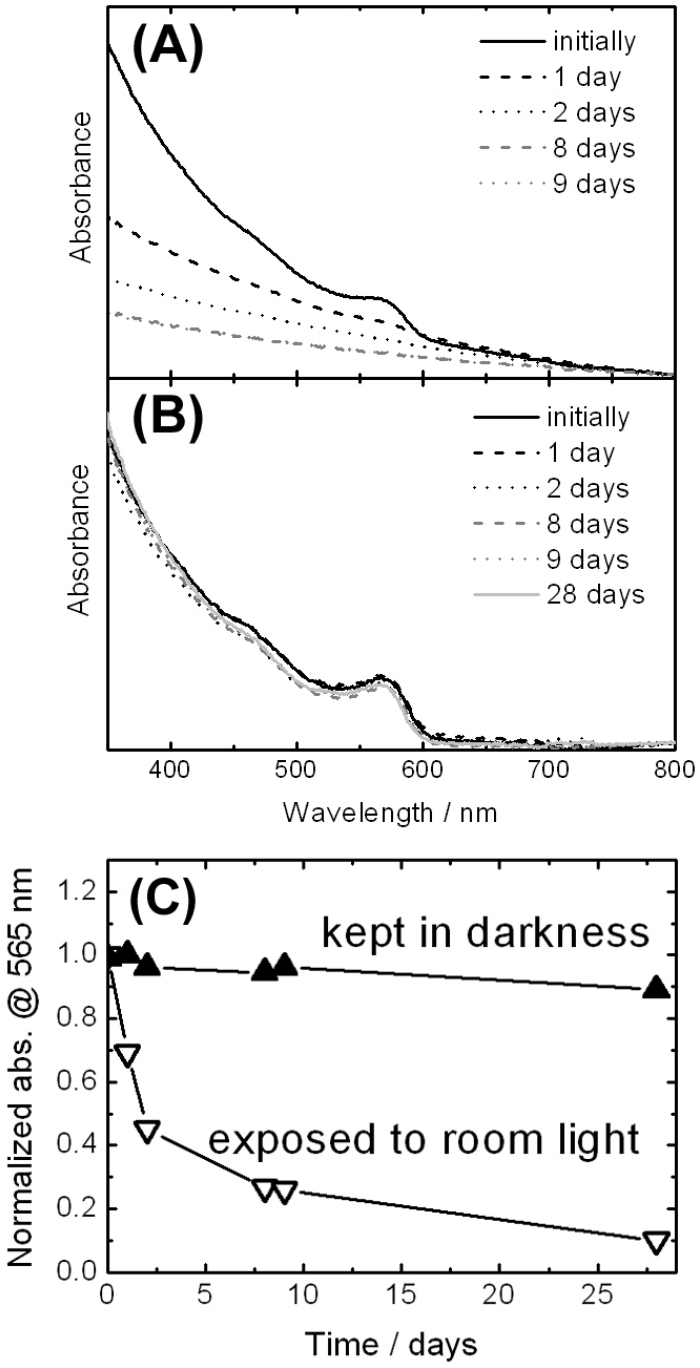

Figure 10.7: Absorption spectra of MUA-coated quantum dots as a function of time (A) exposed to room light and (B) stored in darkness. (C) Normalized absorbance at 565 nm as a function of time of the samples exposed to light and kept in darkness.

yield of the quantum dots over time from 25% to less than 10% over a 20-h period. Changing the ratio of MUA:quantum dot did not significantly alter the kinetics results, but a ratio of less than 80:1 MUA:quantum dot (mass ratio) was not sufficient to render quantum dots water soluble. Our interpretation of this result is that the limiting factor for the water solubilization exchange is steric constraints created by initial surfactants slowly desorbing from the surface, but that a minimum level of exchange must be reached to impart water solubility.

Adding water-soluble thiols to the aqueous quantum dot solution caused significant quenching. This result was expected based on the results of the exchange reaction (Figure **10.3**). However, we found that the quenching efficiency depended strongly on both the size and charge of the thiol. MAA had the strongest effect on quenching (Figure **10.5**), due to its small size allowing easier diffusion and subsequent binding to the quantum dot surface. BME is about the same size as MAA, but caused much less quenching. This difference is most likely due to the carboxylate group of the MAA offering an additional quenching pathway, whereas the alcohol group does not. This hypothesis is supported by the observation of non-linear Stern-Volmer plots indicating multiple quenching pathways with different efficiencies, which is in agreement with amine-quenching results on organic-soluble quantum dots [117], and the observation of quenching by AA but not ethanol. For this reason, MBA was a stronger quencher than BME even though it is larger. *Hoshino et al.* [63] also reported a difference in photoluminescence intensity between carboxyl functionalized and hydroxyl functionalized quantum dots. *Gill et al.* [118] recently found that tyrosine-coated quantum dots were quenched upon enzymatic oxidation of the tyrosine groups, which was assumed to result from electron transfer to the carboxylate group. This quenching effect was discussed as a basis for an optical biosensor to monitor oxidation states of biomolecules containing alcohol groups. Finally, we noticed that the large MUA barely quenched the luminescence. Most likely, steric constraints limit the access of more MUA to the quantum dot surface, already saturated with MUA molecules. Also, the distance from the quantum dot surface to the terminal carboxylate (11 carbons away) probably caused a reduced quenching effect. This suggestion is also supported by the fact that using MAA for water solubilization generally resulted in lower quantum yields than using MUA (results not shown). Luminescence lifetime analysis indicated that the mechanism of quenching was static rather than collisional, which is also in agreement with previous results on amine quenching of organic-soluble uncapped quantum dots [117]. Therefore, the thiol group binds non-reversibly to the quantum dot surface, probably displacing either residual TOPO/HDA ligands or MUA molecules. Quenching is only observed from these coordinated molecules, since the luminescence lifetime analysis showed no change in lifetime with quencher concentration. The source of the quenching could be electron or hole tunneling through the ZnS shell and/or defects in the shell to which the thiolated ligand binds. Previous quenching studies have been performed on uncapped CdSe in organic solvents

[117], but the observation of various quenching effects from different thiolated ligands on water-soluble core-shell quantum dots suggest that other factors than simple binding to the CdSe (or ZnS in the case of capped particles) surface play a significant role in quenching. However, simultaneous characterization of the shell homogeneity and quenching effects will be necessary to determine the relative contributions to the quenching mechanism.

Finally, we observed that the chemical stability of MUA-coated quantum dots depended on their exposure to light. Light-exposed quantum dots began to aggregate almost immediately; within a couple of days, the vast majority of quantum dots had precipitated. However, keeping MUA-coated quantum dots in darkness allowed them to remain stable for more than a month, even if stored at room temperature. Actually, we have found that samples can be stored in darkness for more than a year without precipitation of the quantum dots. This observation is in agreement with the photocatalytic formation of disulfide bonds from the surface-bound thiol groups proposed by Peng and coworkers [62].

The kinetics of ligand exchange and its effect on the quantum yield of core/shell quantum dots were characterized. We also studied the quenching mechanism of quantum dot emission with various water-soluble ligands and found multiple pathways arising from both the surface-binding thiol group and the water-soluble functional group of the ligand. The advantages of thiol-exchanged quantum dots over many other water-solubilization strategies are the relative ease and inexpensiveness of the procedure and the maintenance of a small total quantum dot size. However, understanding the various parameters such as the extent of ligand exchange with time and the properties of the ligand used for water-solubilization is important if the full advantages are to be realized.

10.2 Zwitterionic Biocompatible Water-Soluble Quantum Dots

The application of carboxyl-functionalized quantum dots in biological systems such as cells can be limited by their instability in buffers and cell culture media at neutral and acidic pH [77]. The narrow pH range can lead to aggregation of the water-soluble quantum dots in solution or inside a cell. This problem can potentially be solved by the use of thiolated, zwitterionic ligand alternatives, containing both positively and negatively charged functional groups. We hypothesize that, because the quantum dot remains charged over a wide range of pH values, the colloidal stability should be higher, while the compensation of charge at neutral pH should provide lower non-specific binding of the nanoparticles.

10.2.1 Ligand Exchange with *D*-Penicillamine

D-penicillamine (DPA) or (2S)-2-amino-3-methyl-3-sulfanyl-butanoic acid, a metabolite of penicillin, is a small trifunctional molecule used as a chelating agent. Unlike the mercaptoalkylacids conventionally used for water-solubilization of quantum dots, such as MUA, DPA is not toxic and, in fact, has pharmaceutical applications. *D*-penicillamine is applied in the treatment of copper metabolism disorders, cystinuria and mercury poisoning. Upon incorporation into the human body, DPA undergoes a hepatic metabolism with a biological half-life of 1 h and efficient renal excretion from the organism [119]. By exchanging the initial surfactants of quantum dots with DPA, we hope to extend these biological properties to the resulting water-soluble quantum dots. Therefore, DPA-coated nanoparticles could have potential applications in life science research, especially for *in vivo* experiments. Apart from the biocompatibility of DPA and its colloidal stability over a wide pH range, DPA enables the opportunity for selective bioconjugation via either its carboxylate group or its primary amino group. Once bound to quantum dots via the thiol group, DPA should maintain overall neutrality. However, by simply blocking one of its functional groups, it should be possible to obtain negatively or positively charged nanoparticles.

DPA is generally soluble in polar compounds, such as short-chain alcohols and water. Because of the poor solubility of DPA in 1,4-dioxane, the dioxane/methanol co-solvent system used for the preparation of MUA-coated quantum dots was not applicable for functionalization with DPA. As was the case of MUA-coated quantum dots, performing the DPA exchange reaction in methanol resulted in quantum dots that were only partially soluble in water, again due to the insolubility of the initial quantum dots in methanol. In subsequent efforts, 2-isopropanol was implemented as an alternative medium for the ligand exchange reaction. 2-isopropanol was used as a compromise between the need for a hydrophobic solvent for the unexchanged quantum dots and a hydrophilic solvent for DPA, providing adequate solubility for both the ligand and the nanoparticle. Since the reactivity of DPA is enhanced under conditions in which the proton can more effectively leave the sulfhydryl group, we performed the reaction at pH 9 – 10. The ligand exchange reaction with DPA was performed at 70 – 80°C under a nitrogen atmosphere and was found to have similar kinetics as the exchange reaction of MUA-coated quantum dots. Typically, an exchange reaction time of 32 h was sufficient to replace the initial surfactants in the case of TOPO/HDA-coated quantum dots and 10 min for the case of quantum dots stabilized with OLA.

The resulting DPA-functionalized quantum dots retained about 40 – 60% of their initial photoluminescence efficiency. The nanoparticle solution was clear and contained no precipitates. In Figure **10.8**, we compare the absorption spectra of DPA- and MUA-functionalized capped CdSe/ZnS quantum dots aqueous solutions, prepared from the same sample. The absorption spectrum of MUA-

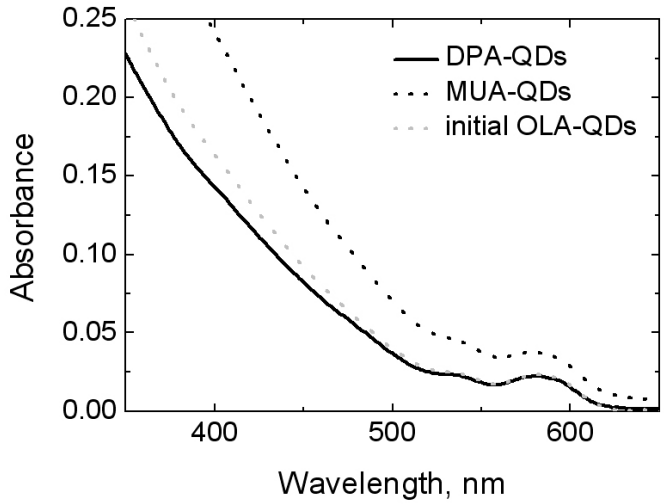

Figure 10.8: Absorption spectra of CdSe/ZnS quantum dots exchanged with DPA (solid line), exchanged with MUA (dotted black line), and as-prepared in OLA (dotted gray line).

coated quantum dots showed a significant scattering profile, evidenced as a sloping baseline offset underneath the absorption spectrum, as a result of forming small aggregates at pH close to neutral. However, the spectrum of DPA-coated quantum dots were even better resolved than the initial OLA-capped quantum dot preparation (in toluene), showing a much lower aggregation tendency of the particles (Figure **10.8**). The observed effect can be explained by improved purity of the DPA-coated quantum dots, since most of organic impurities were not soluble in water at neutral pH, as well as the higher solubility of DPA in water compared to OLA in toluene.

10.3 Comparative Characterization of Biocompatible Quantum Dots

10.3.1 Colloidal Stability of Water-Soluble Quantum Dots

Figure **10.9** highlights the difference in colloidal stability between DPA-coated quantum dots and MUA-coated quantum dots in aqueous solution at different pH. In Figure **10.9(A-C)**, typical ultrasensitive fluorescence microscopy images with single molecule sensitivity of DPA-coated quantum dots immobilized onto a poly-L-lysine-coated glass surface at pH 5.0, 7.0, and 9.2 are shown. Most of the spots were equal in size to the point spread function of the microscope for this wavelength ($\sim$0.3 μm) and were well separated, showing that the quantum dots did not aggregate in this pH range. In contrast, the images of MUA-coated

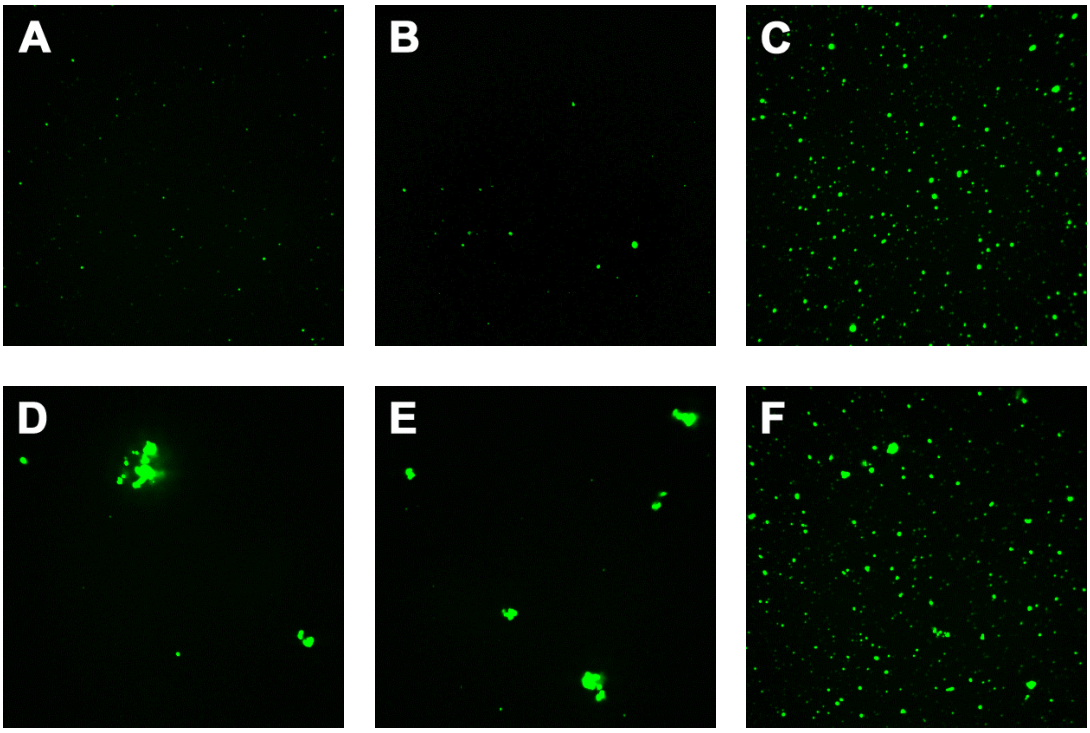

Figure 10.9: Colloidal stability of (A-C) DPA- and (D-F) MUA-functionalized quantum dots immobilized onto a poly-L-lysine-coated glass surface at pH 5.0 (A, D), 7.0 (B, E), and 9.2 (C, F).

quantum dots on the same surfaces showed significant aggregation at pH 5 – 7, Figure **10.9(D-F)**. Only at pH 9.2 did the majority of MUA-coated quantum dots become less aggregated and more spatially separated. However, some of the nanoparticles still existed as aggregates, probably as a result of the incomplete solubility of MUA in water compared to DPA (Figure **10.9(F)**).

Figure **10.10** highlights the non-specific attraction of 1 nM DPA-coated quantum dot and MUA-coated quantum dot solutions to plasma-cleaned glass surfaces. Figure **10.10(A-B)** shows that DPA-coated quantum dots exposed to clean glass surfaces initially adhered to the glass as single, isolated particles, but were easily removed upon flushing the surface with buffer solution. In contrast, Figure **10.10(C-D)** shows that MUA-coated quantum dots were strongly attracted to the glass surfaces, were more aggregated than DPA-coated quantum dots and were not washed away even after extensive flushing with buffer solution. This result highlights the contrast in the attractive forces of the different functionalized quantum dots to charged surfaces.

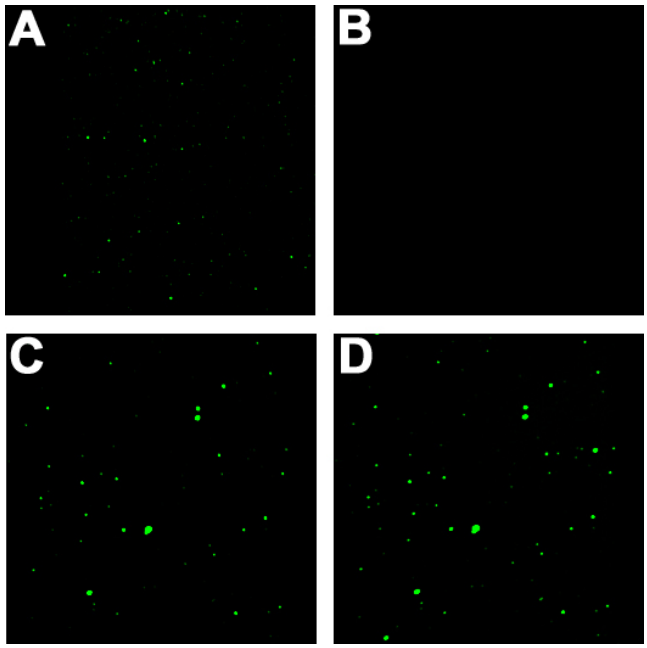

Figure 10.10: Adhesion of water-soluble quantum dots onto plasma-cleaned glass surfaces: (A) 1-nM DPA-coated quantum dot solution added and (B) flushed ×3 with water; (C) 1-nM MUA-coated quantum dot solution added and (D) flushed ×7 with water. Each image is an average of 64 scans.

10.3.2 Non-specific Interaction of Water-Soluble Quantum Dots with Mono Mac 6 Cells

In order to investigate the non-specific interaction of different preparations of water-soluble quantum dots with cells, we chose Mono Mac 6 (Monocytes Macrophages clone 6) cells. Mono Mac 6 is a monocytic cell line, isolated from the peripheral blood of a patient with monoblastic leukemia [120]. Mono Mac 6 is the only established cell line to almost completely retain the phenotypic and functional features of mature monocytes, which are responsible for the ingestion of pathogens and foreign substances into the human body [120]. Therefore, we hypothesized that quantum dots would be more efficiently internalized into Mono Mac 6 cells compared to other cell lines, but that the optimized zwitterionic quantum dots should display a higher resistance to interaction with the cells than those with highly charged and less stable coatings such as MUA-coated quantum dots. To test this hypothesis, we obtained a series of scanning confocal fluorescence microscopy images of Mono Mac 6 cells which had been mixed with DPA-coated quantum dots and MUA-coated quantum dots at various concentrations.

Figure **10.11** illustrates the exposure of Mono Mac 6 to 1-nM and 10-nM DPA-coated quantum dot solutions for 60 min. The cells were subsequently rinsed with clean buffer, and propidium iodide (PI) solution was added at the

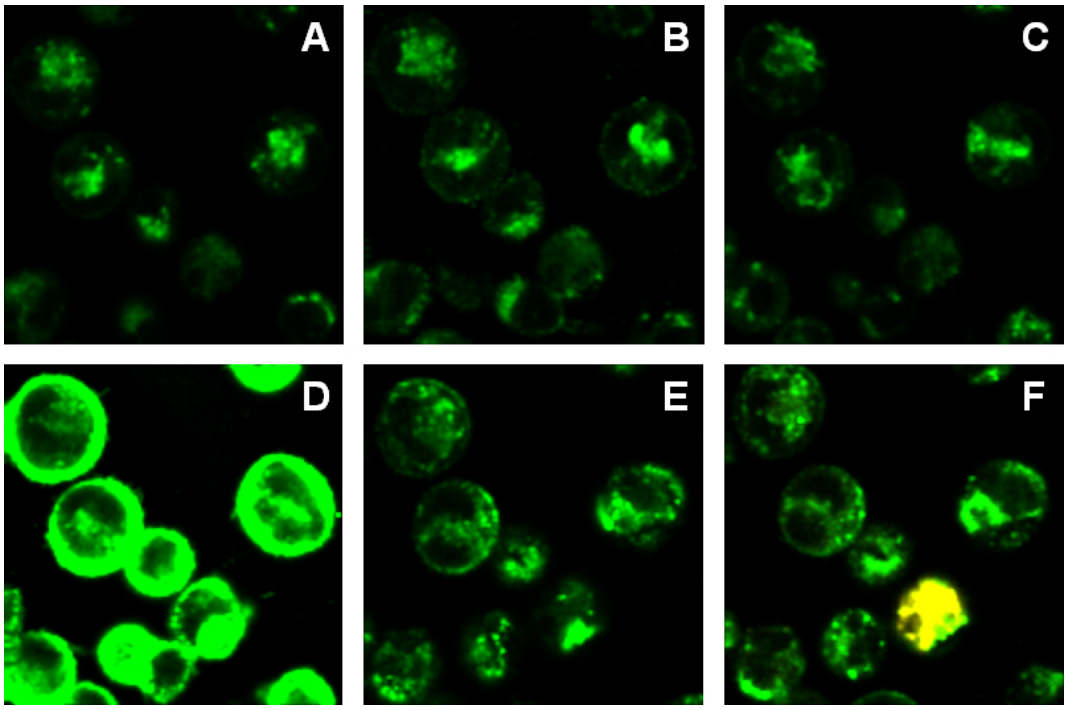

Figure 10.11: Mono Mac 6 cells at pH 7.4 (A) attached to plasma-cleaned glass slide from PBS buffer, showing the cellular autofluorescence in the absence of quantum dots, (B) exposed to 1 nM DPA-coated quantum dots for 30 min, (C) rinsed with PBS buffer after 60 min of exposure, (D) exposed to 10 nM DPA-coated quantum dots for 30 min, (E) rinsed with PBS buffer after 60 min of exposure, (F) propidium iodide added.

end of the experiment in order to test cell viability. At 1-nM concentration, a very slight non-specific interaction between the DPA-coated quantum dots and the cell membrane was observed (Figure **10.11(B)**), but upon flushing with buffer, practically all DPA-coated quantum dots were washed away from the cell membrane (Figure **10.11(C)**). At 10 nM concentration, significant non-specific interaction of the DPA-coated quantum dots with the cell membrane occurred, which appeared as a homogeneous fluorescence ring (Figure **10.11(D-E)**). Upon rinsing with buffer, the quantum dots that had interacted with cells were almost completely washed away, leaving a very small fraction still attached to the membrane (Figure **10.11(E)**). At the end of the experiment, the addition of PI to the cells indicated that practically all cell membranes were still intact, verifying that the quantum dots were not harmful to them at these concentrations (Figure **10.11(F)**).

The corresponding images of Mono Mac 6 cells upon exposure to MUA-coated quantum dot solutions are shown on Figure **10.12**. MUA-coated quantum dots show very different behavior when exposed to the cells. At 1 nM, no quantum dots attached to the cells during 1 h of exposure (Figure **10.12(A-C)**), while at

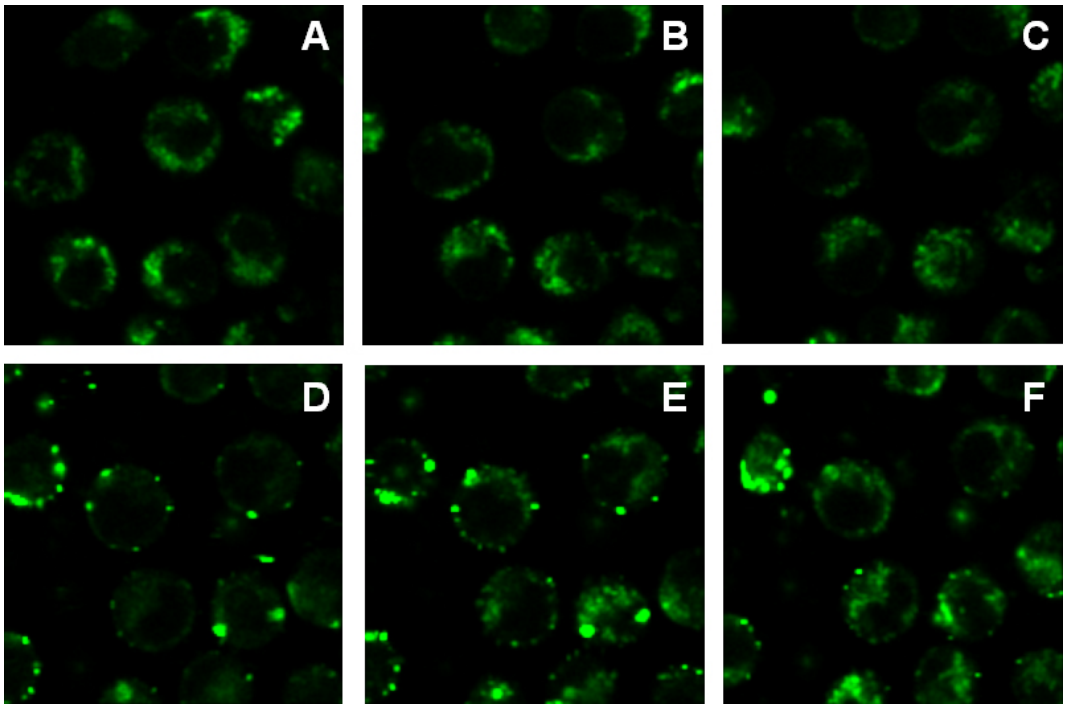

Figure 10.12: Mono Mac 6 cells at pH 7.4 (A) attached to a plasma-cleaned glass slide from PBS buffer, (B) exposed to 1 nM MUA-coated quantum dots for 30 min, (C) rinsed with PBS buffer after 60 min of exposure, (D) exposed to 10 nM MUA-coated quantum dots for 30 min, (E) rinsed with PBS buffer after 60 min of exposure, (F) propidium iodide added.

10-nM, the quantum dots aggregated onto the cell membrane surface, labeling them inhomogeneously (Figure **10.12(D)**). Flushing the cells with clean buffer did not remove the quantum dot aggregates from the cell membrane (Figure **10.12(E)**).

The concentrations of both MUA-coated quantum dots and DPA-coated quantum dots used in the experiments were derived from absorption spectra of bulk solutions using an empirical formula that relates the quantum dot size to the molar absorptivity, ε [94]. However, since MUA-coated quantum dots were partially aggregated at neutral pH, the number of single MUA-coated quantum dots at pH 7.4 was effectively reduced compared to DPA-coated quantum dots. In order to more accurately estimate the effective concentration of MUA-coated quantum dots in the solution, we positioned the focus of the scanning confocal microscope into the solution above the cells and collected fluorescence traces. From the traces, photon counting histograms (PCH) were extracted to determine the aggregation state (Figure **10.13**). At 1-nM concentration only one quantum dot on average is within the 1 fl confocal volume at any given time, each with an intensity of about 8 – 10 counts/ms (the typical intensity of a single surface-immobilized

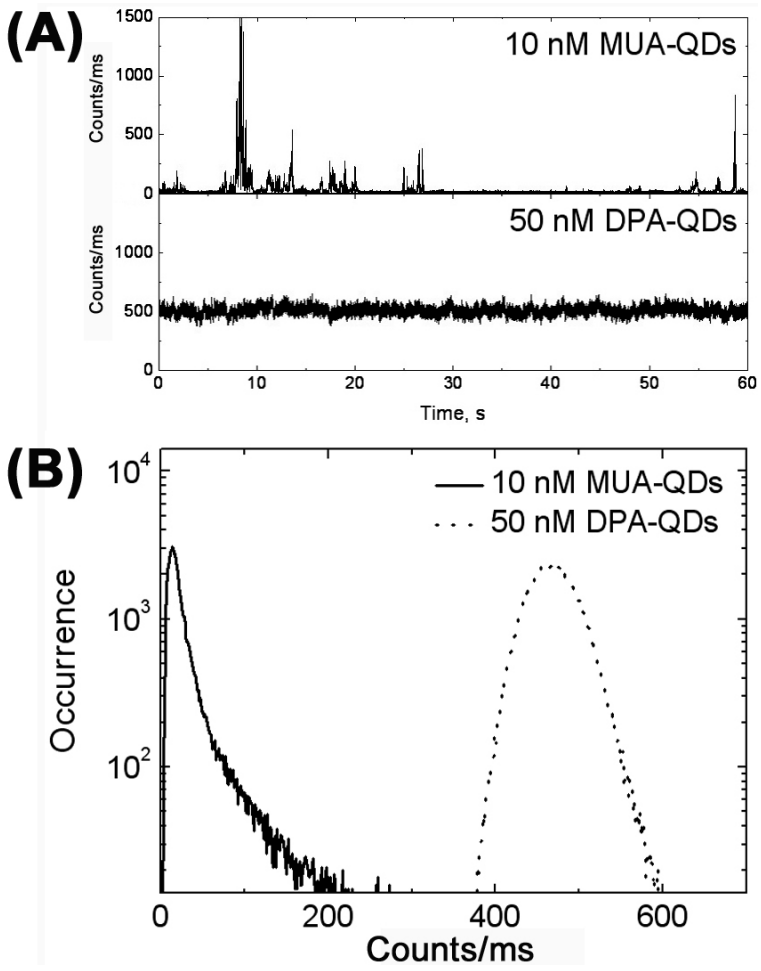

Figure 10.13: Fluorescence traces and the corresponding photon counting histograms (PCH) for 10 nM MUA-coated quantum dots and 50 nM DPA-coated quantum dots.

quantum dot). Therefore a 10-nM quantum dot concentration should have an average intensity of about 80 – 100 counts/ms. However, for 10-nM MUA-coated quantum dot solutions in PBS, PCH analysis showed the most probable intensity occurrence at 20 – 30 counts/ms, much smaller than expected (Figure **10.13**). The elongated tail at higher count rates in the PCH as well as the observation of sharp, intense spikes in the fluorescence traces additionally underlined the high aggregation state for 10-nM MUA-coated quantum dots, while even 50-nM DPA-coated quantum dots solution showed constant intensity over the whole 60-s trace. For DPA-coated quantum dots, the most probable intensity was approximately 450 – 500 counts/ms (Figure **10.13**). This intensity corresponds to a rate of ∼9.5 counts/ms (kHz) per 1 nM, as would be expected for a single DPA-coated quantum dot.

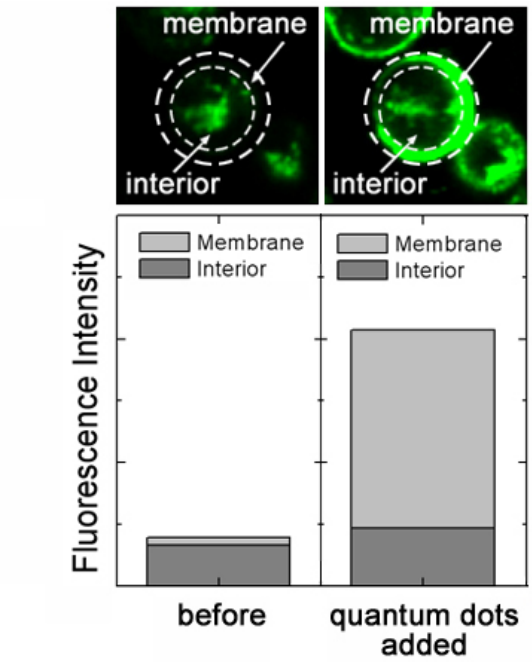

Figure 10.14: Sample data analysis of scanning confocal microscope image: Fluorescence intensity integrated over the whole cell and the interior region with the corresponding bar chart.

This aggregation effect explains the lower observed fluorescence intensity of MUA-coated quantum dots on the membrane of Mono Mac 6 cells (Figure **10.12**). At both 1- and 10-nM MUA-coated quantum dot concentrations, a considerably higher fraction of aggregated quantum dots is observed, effectively reducing the number of species in solution that interact with the cell membrane.

In order to determine the fate of quantum dots that did interact with the cells, we analyzed the confocal scans of Figures **10.11** and **10.12** as follows. For each cell the fluorescence intensities integrated over the entire cell (circular area with diameter d_1) and integrated over the interior area (circular area with diameter $0.75d_1$) were determined in order to estimate the intracellular quantum dot uptake, as depicted in Figure **10.14**. In the resulting Figure **10.15**, we show the average fluorescence intensity of a cell, separated into the contributions from the membrane and the cellular interior. The data represent the three points of interaction kinetics that were shown in Figure **10.11** and **10.12**, i.e., the cellular autofluorescence before the addition of quantum dots, after 30 min of exposure, and after rinsing with buffer at the end of experiment.

For 1-nM DPA-coated quantum dots, the slight increase in the overall intensity of the cell upon addition of quantum dots seemed to arise primarily from membrane-quantum dot interactions. This uptake was effectively removed by rinsing (Figure **10.15(A)**). No quantum dots were found inside the cells following

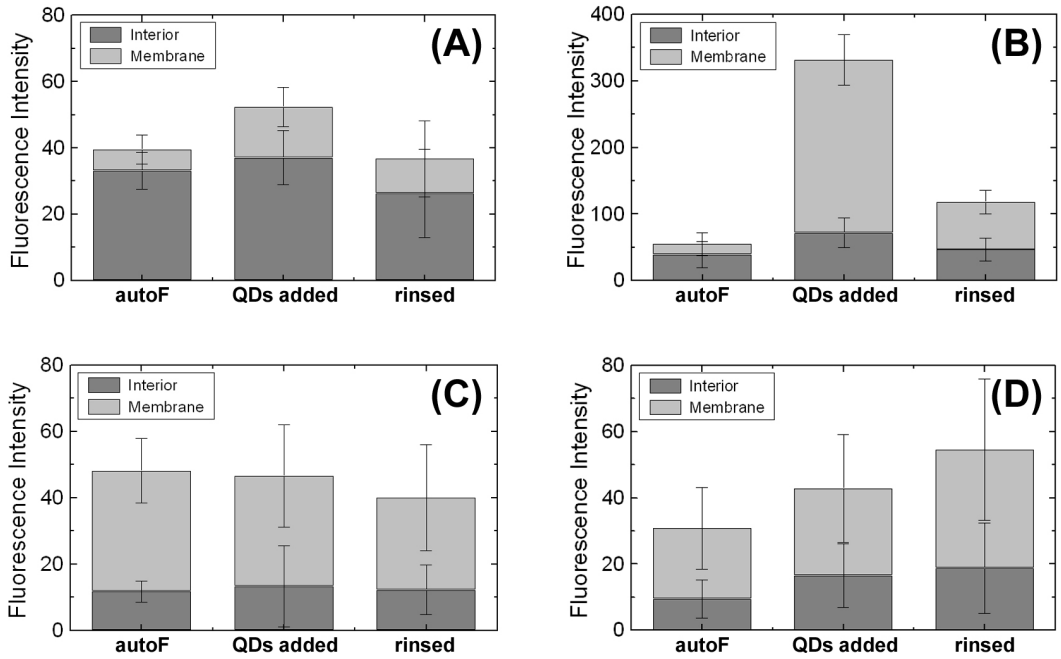

Figure 10.15: Non-specific interaction of Mono Mac 6 cells with (A) 1-nM and (B) 10-nM DPA-coated quantum dots, (C) 1-nM and (D) 10-nM MUA-coated quantum dots. Columns represent integrated fluorescence intensity averaged over several cells, with highlighted contributions from the edges (membrane) and the center (nucleus) of the cell in light and dark gray, respectively. The intensity was measured before addition of quantum dots (autofluorescence of cells), after 30 min of interaction, and after thorough rinsing of the channel with buffer.

60 min of exposure or after rinsing with buffer (Figure **10.15(A)**). The addition of 1-nM MUA-coated quantum dot solution to Mono Mac 6 cells did not cause any detectable fluorescence increase either inside the cell or on the membrane (Figure **10.15(C)**). Apparently, the effective concentration of interacting species in solution was dramatically reduced by quantum dot aggregation, as discussed above. The decrease in cell fluorescence over time is due to photobleaching of naturally-occurring fluorescent species from the cell (Figure **10.15(C)**).

Upon exposure of Mono Mac 6 cells to 10-nM DPA-coated quantum dots, the overall fluorescence intensity increased by 5 – 6 fold, mostly from an increase in the membrane fluorescence, along with a slight increase in the cell interior, which was found in some cells (Figure **10.15(B)**). Some quantum dots (about 15 – 20% of the overall fluorescence intensity increment) remained on the membrane even after flushing (Figure **10.15(B)**). For 10-nM MUA-coated quantum dots, the overall quantum dot uptake, both on the membrane and inside the cell, constantly increased over the 1 h period of exposure. The fluorescence could not be removed by flushing (Figure **10.15(D)**). Apparently, MUA-coated quantum

dots were more strongly attracted to the cellular membrane, possibly as a result of hydrophobic interactions between the long hydrocarbon MUA chains on the quantum dots and the hydrophobic domains of the lipids within the membrane, or from strong electrostatic interactions between the highly charged MUA-coated quantum dots and the charged phospholipid headgroups of the membrane lipids (similar to the way that MUA-coated quantum dots interact with bare glass surfaces).

10.3.3 Discussion and Conclusions

Because of the presence of positively and negatively charged functional groups on the surface of DPA-coated quantum dots, they showed high solubility in water, illustrated by a high ratio of well-resolved absorbance to scattering background (Figure **10.8**). For MUA-coated quantum dots, light scattering due to nanoparticle aggregation was observed in the absorption spectrum (Figure **10.8**). At pH values close to neutral, the carboxylic groups on the surface of MUA-coated quantum dots remained only partially deprotonated, thus a strong base (typically TMAHP) was added in order to obtain optically clear solutions. In a previous report by *Reiss et al.* [22], transferring MUA-coated quantum dots into water after ligand exchange, ammonium hydroxide solution was used. Similarly, quantum dots exchanged with dihydrolipoic acid, deprotonation of the resulting nanoparticles with potassium-tert-butoxide was reported to be a crucial step to provide solubility in aqueous solutions [69]. Therefore, MUA-coated quantum dots were unable to maintain colloidal stability in buffer solutions at pH 5 – 7, whereas DPA-coated quantum dots showed no aggregation over the pH range of 5 – 9.2 (Figure **10.9**). The deprotonated MUA-coated quantum dots also showed little aggregation. However, due to the large negative surface charge of MUA-coated quantum dots, a strong attraction of MUA-coated quantum dots to plasma-cleaned glass slides was observed (Figure **10.10**). The high surface charge of MUA-coated quantum dots might increase non-specific interaction with other charged entities in biological systems.

The observed differences in charge and stability resulted in a different non-specific interaction nature of MUA-coated quantum dots and DPA-coated quantum dots with Mono Mac 6 cells. Unlike 10-nM MUA-coated quantum dots, which were mostly aggregated in solution and accumulated on the plasma membrane or inside the cell, 10-nM DPA-coated quantum dots were observed for homogeneous interaction with the cellular membrane. The majority of quantum dot interaction with the cells was removed by flushing with buffer, showing that the interaction is rather weak. However, a small fraction of quantum dots was retained on the membrane. At lower concentrations, few single DPA-coated quantum dots were observed at the surface of Mono Mac 6 cells, but were not internalized by the cells. Long exposure of the cells to high concentrations of DPA-coated quantum dots ($\geq$10 nM) may increase the probability of some nanoparticles to

penetrate deeper into the plasma membrane so that they could not be washed away by the buffer upon flushing. In those cases in which a small number of DPA-coated quantum dots penetrated into the cellular interior, the majority of cells were left intact, suggesting a low toxicity of the nanoparticles to the cells.

Labeling of cells with functionalized quantum dots has potential limitations in non-specific binding of the particles to the cells, which will lower the detection limits of and the confidence in the experiment. At low concentrations (e.g., those used for single particle tracking experiments), one must be certain that the label is specifically bound to the biomolecule of interest, while at high concentrations, high non-specific binding will increase the overall fluorescence background. The observed low non-specific binding of DPA-coated quantum dots and lack of aggregation, confirmed by PCH, show that they are extremely promising tools for cell-based assays. The chemical properties of DPA-coated quantum dots are useful for specific labeling inside the cell, where the pH may vary from neutral to acidic, depending on the cellular compartment of interest. Therefore, strategies of bioconjugation of DPA-coated quantum dots to proteins and antibodies should be further developed.

Outlook

The development of colloidal quantum dots has opened a new dimension for single-molecule applications. The advantages of quantum dots as fluorescent labels over conventional labeling tools, such as organic dyes and autofluorescent proteins, enable long-time imaging experiments at low labeling levels, which is particularly beneficial for many applications in biophysics and the life sciences [3, 4, 6]. Current published experimental techniques allow one to produce highly luminescent photostable core/shell quantum dot structures, but the reported water-solubilization and biofunctionalization strategies lack a general solution to achieve maximal biocompatibility, high luminescence efficiency and minimally overall size [77]. Thus, research towards the development of biocompatible coatings for quantum dots is an extremely challenging task.

Fluorescence intermittency of quantum dots is another major drawback for biophysical application at the single molecule level [57]. The high complexity of quantum dots, variations from particle to particle even within the same batch and heterogeneous surface composition, together with a number of other factors, induce entangled behavior which is impossible to thoroughly explain without a single-particle insight. The investigation of the underlying principles of quantum dots blinking is a subject of major importance and a necessary step towards the optimization of quantum dots for biological application.

The fabrication of quantum dot structures with different structural properties, enabled by simply varying the ligand composition, is helpful not only for chemists and materials scientists for the development of new nanomaterials, but also provides a deeper understanding in the role of surfactants in the growth of nanoparticles.

Bibliography

[1] R. Dingle, W. Wiegmann, and C. H. Henry. Quantum states of confined carriers in very thin $Al_xGa_{1-x}As$-GaAs-$Al_xGa_{1-x}As$ heterostructures. *Physical Review Letters*, 33:827–830, 1974.

[2] C. B. Murray, D. J. Norris, and M. G. Bawendi. Synthesis and characterization of nearly monodisperse CdE (E = S and Se and Te) semiconductor nanocrystallites. *Journal of the American Chemical Society*, 115:8706–8715, 1993.

[3] W. C. W. Chan and S. Nie. Quantum dot bioconjugates for ultrasensitive nonisotopic detection. *Science*, 281:2016–2018, 1998.

[4] M. Bruchez, Jr., M. Moronne, P. Gin, S. Weiss, and A. P. Alivisatos. Semiconductor nanocrystals as fluorescent biological labels. *Science*, 281:2013–2016, 1998.

[5] A. M. Derfus, W. C. W. Chan, and S. N. Bhatia. Probing the cytotoxicity of semiconductor quantum dots. *Nano Letters*, 4:11–18, 2004.

[6] X. Michalet, F. F. Pinaud, L. A. Bentolila, J. M. Tsay, S. Doose, J. J. Li, G. Sundaresan, A. M. Wu, S. S. Gambhir, and S. Weiss. Quantum dots for live cells and in vivo imaging and diagnostics. *Science*, 307:538–544, 2005.

[7] K. T. Shimizu, R. G. Neuhauser, C. A. Leatherdale, S. A. Empedocles, W. K. Woo, and M. G. Bawendi. Blinking statistics in single semiconductor nanocrystal quantum dots. *Physical Review B*, 63:205316(1–5), 2001.

[8] M. Kuno, D. P. Fromm, H. F. Hamann, A. Gallagher, and D. J. Nesbitt. "On"/"Off" fluorescence intermittency of single semiconductor quantum dots. *The Journal of Chemical Physics*, 115:1028–1040, 2001.

[9] A. L. Efros and M. Rosen. Random telegraph signal in the photoluminescence intensity of a single quantum dot. *Physical Review Letters*, 78:1110 – 1113, 1997.

[10] L. Brus. Electronic wave functions in semiconductor clusters: Experiment and theory. *Journal of Physical Chemistry*, 90:2555–2560, 1986.

[11] V. I. Klimov and D. W. McBranch. Femtosecond 1P-to-1S electron relaxation in strongly confined semiconductor nanocrystals. *Physical Review Letters*, 80:4028–4031, 1998.

[12] M. A. Hines and G. D. Scholes. Colloidal PbS nanocrystals with size-tunable near-infrared emission: Observation of post-synthesis self-narrowing of the particle size distribution. *Advanced Materials*, 15:1844–1849, 2003.

[13] M. Miyamura, K. Tachibana, and Y. Arakawa. UV photoluminescence from size-controlled GaN quantum dots grown by MOCVD. *Physica Status Solidi (a)*, 192:33–38, 2002.

[14] V. A. Fonoberov and A. A. Balandin. Origin of ultraviolet photoluminescence in ZnO quantum dots: Confined excitons versus surface-bound impurity exciton complexes. *Applied Physics Letters*, 85:5971–5973, 2004.

[15] M. G. Berrettini, G. Braun, J. G. Hu, and G. F. Strouse. NMR analysis of surface and interfaces in 2-nm CdSe. *Journal of the American Chemical Society*, 126:7063–7070, 2004.

[16] J. Taylor, T. Kippeny, and S.J.Rosenthal. Surface stoichiometry of CdSe nanocrystals determined by rutherford backscattering spectroscopy. *Journal of Cluster Science*, 12:571–582, 2001.

[17] D. V. Talapin, A. L. Rogach, A. Kornowski, M. Haase, and H. Weller. Highly luminescent monodisperse CdSe and CdSe/ZnS nanocrystals synthesized in a hexadecylamine-trioctylphosphine oxide-trioctylphospine mixture. *Nano Letters*, 1:207–211, 2001.

[18] S. H. Tolbert and A. P. Alivisatos. Size dependence of a first order solid-solid phase transition: The wurtzite to rock salt transformation in CdSe nanocrystals. *Science*, 265:373–376, 1994.

[19] J. J. Shiang, A. V. Kadavanich, R. K. Grubbs, and A. P. Alivisatos. Symmetry of annealed wurtzite CdSe nanocrystals: Assignment to the C3v point group. *Journal of Physical Chemistry*, 99:17417–17422, 1995.

[20] Q. Wang and D.-K. Seo. Synthesis of deep-red-emitting CdSe quantum dots and general non-inverse-square behavior of quantum confinement in CdSe quantum dots. *Chemistry of Materials*, 18:5764–5767, 2006.

[21] J. E. Bowen Katari, V. L. Colvin, and A. P. Alivisatos. X-ray photoelectron spectroscopy of CdSe nanocrystals with applications to studies of the nanocrystal surface. *Journal of Physical Chemistry*, 98:4109–4117, 1994.

[22] P. Reiss, J. Bleuse, and A. Pron. Highly luminescent CdSe/ZnSe core/shell nanocrystals of low size dispersion. *Nano Letters*, 2:781–784, 2002.

[23] R. He and H. Gu. Synthesis and characterization of mondispersed CdSe nanocrystals at lower temperature. *Colloids and Surfaces A: Physicochemical and Engineering Aspects*, 272:111–116, 2006.

[24] X. Peng, M. C. Schlamp, A. V. Kadavanich, and A. P. Alivisatos. Epitaxial growth of highly luminescent CdSe/CdS core/shell nanocrystals with photostability and electronic accessibility. *Journal of the American Chemical Society*, 119:7019–7029, 1997.

[25] B. O. Dabbousi, J. Rodriguez-Viejo, F. V. Mikulec, J. R. Heine, H. Mattoussi, R. Ober, K. F. Jensen, and M. G. Bawendi. (CdSe)ZnS core-shell quantum dots: Synthesis and characterization of a size series of highly luminescent nanocrystallites. *Journal of Physical Chemistry B*, 101:9463–9475, 1997.

[26] M. A. Hines and P. Guyot-Sionnest. Synthesis and characterization of strongly luminescing ZnS-capped CdSe nanocrystals. *Journal of Physical Chemistry*, 100:468–471, 1996.

[27] L. Qu, A. Peng, and X. Peng. Alternative routes toward high quality CdSe nanocrystals. *Nano Letters*, 1:333–337, 2001.

[28] J.J. Li, Y.A. Wang, W. Guo, J.C. Keay, T.D. Mishima, M.B. Johnson, and X. Peng. Large-scale synthesis of nearly monodisperse CdSe/CdS core/shell nanocrystals using air-stable reagents via successive ion layer adsorption and reaction. *Journal of the American Chemical Society*, 125:12567–12575, 2003.

[29] V. K. La Mer and R. H. Dinegar. Theory and production and mechanism of formation of monodispersed hydrosols. *Journal of the American Chemical Society*, 72:4847–4854, 1950.

[30] Z. A. Peng and X. Peng. Formation of high-quality CdTe and CdSe and CdS nanocrystals using CdO as precursor. *Journal of the American Chemical Society*, 123:183–184, 2001.

[31] C. de Mello Donega, S. G. Hickey, S. F. Wuister, D. Vanmaekelbergh, and A. Meijerink. Single-step synthesis to control the photoluminescence quantum yield and size dispersion of CdSe nanocrystals. *Journal of Physical Chemistry B*, 107:489–496, 2003.

[32] C. B. Murray, C. R. Kagan, and M. G. Bawendi. Synthesis and characterization of monodisperse nanocrystals and close-packed nanocrystal assemblies. *Annual Review of Material Science*, 30:545–610, 2000.

[33] L. Qu, W. W. Yu, and X. Peng. In situ observation of the nucleation and growth of CdSe nanocrystals. *Nano Letters*, 4:465–469, 2004.

[34] Y. De Smet, L. Deriemaeker, and R. Finsy. A simple computer simulation of ostwald ripening. *Langmuir*, 13:6884–6888, 1997.

[35] H. Graetz. Ostwald ripening: New relations between particle growth and particle size distribution. *Scripta Materialia*, 37:9–16, 1997.

[36] Z. Zhelev, R. Bakalova, H. Ohba, R. Jose, Y. Imai, and Y. Baba. Uncoated and broad fluorescent and size-homogenous CdSe quantum dots for ultrasensitive bioanalyses. *Analytical Chemistry*, 78:321–330, 2006.

[37] Y-W. Lin, M-M. Hsieh, C-P. Liu, and H-T. Chang. Photoassisted synthesis of CdSe and core-shell CdSe/CdS quantum dots. *Langmuir*, 21:728–734, 2004.

[38] A. L. Rogach, A. Kornowski, M. Gao, A. Eychmueller, and H. Weller. Synthesis and characterization of a size series of extremely small thiol-stabilized CdSe nanocrystals. *Journal of Physical Chemistry B*, 103:3065–3069, 1999.

[39] M. J. Murcia, D. L. Shaw, H. Woodruff, C. A. Naumann, B. A. Young, and E. C. Long. Facile sonochemical synthesis of highly-luminescent ZnS-shelled CdSe quantum dots. *Chemistry of Materials*, 18:2219 – 2225, 2006.

[40] D. V. Talapin, I. Mekis, S. Goetzinger, and A. Kornowski. CdSe/CdS/ZnS and CdSe/ZnSe/ZnS core-shell-shell nanocrystals. *Journal of Physical Chemistry B*, 108:18826–18831, 2004.

[41] H. Peter Lu and X. Sunney Xie. Single-molecule spectral fluctuations at room temperature. *Nature*, 385:143–146, 1997.

[42] R. M. Dickson, A. B. Cubitt, R. Y. Tsien, and W. E. Moerner. "On"/"Off" blinking and switching behaviour of single molecules of green fluorescent protein. *Nature*, 388:355–358, 1997.

[43] A. Schenk, S. Ivanchenko, C. Röcker, J. Wiedenmann, and G. U. Nienhaus. Photodynamics of red fluorescent proteins studied by fluorescence correlation spectroscopy. *Biophysical Journal*, 86:384–394, 2004.

[44] M. Nirmal, B. O. Dabbousi, M. G. Bawendi, J. J. Macklin, J. K. Trautman, T. D. Harris, and L. E. Brus. Fluorescence intermittency in single cadmium selenide nanocrystals. *Nature*, 383:802–804, 1996.

[45] V. I. Klimov. Optical nonlinearities and ultrafast carrier dynamics in semiconductor nanocrystals. *Journal of Physical Chemistry B*, 104:6112–6123, 2000.

[46] T. D. Krauss and L. E. Brus. Charge and polarizability and photoionization of single semiconductor nanocrystals. *Physical Review Letters*, 83:4840–4843, 1999.

[47] T. D. Krauss, S. O'Brien, and L: E. Brus. Charge and photoionization properties of single semiconductor nanocrystals. *Journal of Physical Chemistry B*, 105:1725–1733, 2001.

[48] R. G. Neuhauser, K. T. Shimizu, W. K. Woo, S. A. Empedocles, and M. G. Bawendi. Correlation between fluorescence intermittency and spectral diffusion in single semiconductor quantum dots. *Physical Review Letters*, 85:3301 – 3304, 2000.

[49] S. A. Empedocles, R. Neuhauser, K. Shimizu, and M. G. Bawendi. Photoluminescence from single semiconductor nanostructures. *Advanced Materials*, 11:1243–1316, 1999.

[50] M. Kuno, D. P. Fromm, H. F. Hamann, A. Gallagher, and D. J. Nesbitt. Nonexponential "blinking" kinetics of single CdSe quantum dots: A universal power law behavior. *The Journal of Chemical Physics*, 112:3117–3120, 2000.

[51] M. Kuno, D. P. Fromm, S. T. Johnson, A. Gallagher, and D. J. Nesbitt. Modeling distributed kinetics in isolated semiconductor quantum dots. *Physical Review B*, 67:125304(1–15), 2003.

[52] R. Verberk, A. M. van Oijen, and M. Orrit. Simple model for the power-law blinking of single semiconductor nanocrystals. *Physical Review B*, 66:233202(1–4), 2002.

[53] K. Zhang, H. Chang, A. Fu, A. P. Alivisatos, and H. Yang. Continuous distribution of emission states from single CdSe/ZnS quantum dots. *Nano Letters*, 6:843–847, 2006.

[54] M. Pelton, D. G. Grier, and P. Guyot-Sionnest. Characterizing quantum-dot blinking using noise power spectra. *Applied Physics Letters*, 85:819–821, 2004.

[55] I. S. Osadko. Power-law statistics of intermittent photoluminescence in single semiconductor nanocrystals. *JETP Letters*, 79:416–419, 2004.

[56] J. Tang and R. A. Marcus. Single particle versus ensemble average: From power-law intermittency of a single quantum dot to quasistretched exponential fluorescence decay of an ensemble. *The Journal of Chemical Physics*, 123:204511(1–6), 2005.

[57] P. A. Frantsuzov and R. A. Marcus. Explanation of quantum dot blinking without the long-lived trap hypothesis. *Physical Review B*, 72:155321(1–10), 2005.

[58] L. Qu and X. Peng. Control of photoluminescence properties of CdSe nanocrystals in growth. *Journal of the American Chemical Society*, 124:2049–2055, 2002.

[59] X. Wu, H. Liu, J. Liu, K. N. Haley, J. A. Treadway, J. P. Larson, N. Ge, F. Peale, and M. P. Bruchez. Immunofluorescent labeling of cancer marker Her2 and other cellular targets with semiconductor quantum dots. *Nature Biotechnology*, 21:41–46, 2003.

[60] Wang, Y. A.; Li, J. J.; Chen, H.; Peng, and X. Stabilization of inorganic nanocrystals by organic dendrons. *Journal of the American Chemical Society*, 124:2293–2298, 2002.

[61] B. Dubertret, P. Skourides, D. J. Norris, V. Noireaux, A. H. Brivanlou, and A. Libchaber. In vivo imaging of quantum dots encapsulated in phospholipid micelles. *Science*, 298:1759–1762, 2002.

[62] J. Aldana, Y. A. Wang, and X. Peng. Photochemical instability of CdSe nanocrystals coated by hydrophilic thiols. *Journal of the American Chemical Society*, 123:8844–8850, 2001.

[63] A. Hoshino, K. Fujioka, T. Oku, M. Suga, Y. F. Sasaki, T. Ohta, M. Yasuhara, K. Suzuki, and K. Yamamoto. Physicochemical properties and cellular toxicity of nanocrystal quantum dots depend on their surface modification. *Nano Letters*, 4:2163–2169, 2004.

[64] S.-W. Kim, S. Kim, J. B. Tracy, A. Jasanoff, and M. G. Bawendi. Phosphine oxide polymer for water-soluble nanoparticles. *Journal of the American Chemical Society*, 127:4556–4557, 2005.

[65] M. Kuno, J. K. Lee, B. O. Dabbousi, F. V. Mikulec, and M. G. Bawendi. The band edge luminescence of surface modified CdSe nanocrystallites: Probing the luminescing state. *Journal of Chemical Physics*, 106:9869–9882, 1997.

[66] D. Gerion, F. Pinaud, S. C. Williams, W. J. Parak, D. Zanchet, S. Weiss, and A. P. Alivisatos. Synthesis and properties of biocompatible water-soluble silica-coated CdSe/ZnS semiconductor quantum dots. *Journal of Physical Chemistry B*, 105:8861–8871, 2001.

[67] C. Bullen and P. Mulvaney. The effects of chemisorption on the luminescence of CdSe quantum dots. *Langmuir*, 22:3007–3013, 2006.

[68] J. R. Lakowicz. *Topics In Fluorescence Spectroscopy*, volume 2. Plenum Press, 1991.

[69] H. Mattoussi, J. M. Mauro, E. R. Goldman, G. P. Anderson, V. C. Sundar, F. V. Mikulec, and M. G. Bawendi. Self-assembly of CdSe-ZnS quantum dot bioconjugates using an engineered recombinant protein. *Journal of the American Chemical Society*, 122:12142–12150, 2000.

[70] V. L. Colvin, M. C. Schlamp, and A. P. Alivisatos. Light-emitting diodes made from cadmium selenide nanocrystals and a semiconducting polymer. *Nature*, 370:354 – 357, 1994.

[71] M. C. Schlamp, Xiaogang Peng, and A. P. Alivisatos. Improved efficiencies in light emitting diodes made with CdSe(CdS) core/shell type nanocrystals and a semiconducting polymer. *Journal of Applied Physics*, 82:5837–5842, 1997.

[72] D. C. Sun, S. R. Friberg, K. Watanabe, S. Machida, Y. Horikoshi, and Y. Yamamoto. High power and high efficiency vertical cavity surface emitting GaAs laser. *Applied Physics Letters*, 61:1502–1503, 1992.

[73] I. L. Medintz, H. T. Uyeda, E. R. Goldman, and H. Mattoussi. Quantum dot bioconjugates for imaging and labelling and sensing. *Nature Materials*, 4:435–446, 2006.

[74] G. T. Hermanson. *Bioconjugate Techniques*. Elsevier Science, 1996.

[75] F. Pinaud, D. King, H-P. Moore, and S. Weiss. Bioactivation and cell targeting of semiconductor CdSe/ZnS nanocrystals with phytochelatin-related peptides. *Journal of the American Chemical Society*, 126:6115–6123, 2004.

[76] J. Aldana, N. Lavelle, Y. Wang, and X. Peng. Size-dependent dissociation pH of thiolate ligands from cadmium chalcogenide nanocrystals. *Journal of the American Chemical Society*, 127:2496–2504, 2005.

[77] Wolfgang J. Parak, Teresa Pellegrino, and Christian Plank. Labelling of cells with quantum dots. *Nanotechnology*, 16:R9R25, 2005.

[78] S. Weiss. Measuring conformational dynamics of biomolecules by single molecule fluorescence spectroscopy. *Nature Structural Biology*, 7:724–729, 2000.

[79] A. A. Deniz, T. A. Laurence, G. S. Beligere, M. Dahan, A. B. Martin, D. S. Chemla, P. E. Dawson, P. G. Schultz, and S. Weiss. Single-molecule protein folding: Diffusion fluorescence resonance energy transfer studies of the denaturation of chymotrypsin inhibitor 2. *Proceedings of the National Academy of Sciences*, 97:5179–5184, 2000.

[80] D. C. Daniel, M. Thompson, and N. W. Woodbury. Fluorescence intensity fluctuations of individual labeled DNA fragments and a DNA binding protein in solution at the single molecule level: A comparison of photobleaching and diffusion and binding dynamics. *Journal of Physical Chemistry B*, 104:1382–1390, 2000.

[81] D. S. Talaga, W. Leung Lau, H. Roder, J. Tang, Y. Jia, W. F. DeGrado, and R. M. Hochstrasser. Dynamics and folding of single two-stranded coiled-coil peptides studied by fluorescent energy transfer confocal microscopy. *Proceedings of the National Academy of Sciences*, 97:13021–13026, 2000.

[82] E. Rhoades, E. Gussakovsky, and G. Haran. Watching proteins fold one molecule at a time. *Proceedings of the National Academy of Sciences*, 100:3197–3202, 2003.

[83] D. M. Willard, L. L. Carillo, J. Jung, and A. Van Orden. CdSe-ZnS quantum dots as resonance energy transfer donors in a model protein-protein binding assay. *Nano Letters*, 1:469–474, 2001.

[84] A. R. Clapp, I. L. Medintz, J. M. Mauro, B. R. Fisher, M. G. Bawendi, and H. Mattoussi. Fluorescence resonance energy transfer between quantum dot donors and dye-labeled protein acceptors. *Journal of the American Chemical Society*, 126(1):301–310, 2004.

[85] I. L. Medintz, S. A. Trammell, H. Mattoussi, and J. M. Mauro. Reversible modulation of quantum dot photoluminescence using a protein bound photochromic fluorescence resonance energy transfer acceptor. *Journal of the American Chemical Society*, 126:30–31, 2004.

[86] P. H. M. Lommerse, B. E. Snaar-Jagalska, H. P. Spaink, and T. Schmidt. Single-molecule diffusion measurements of H-Ras at the plasma membrane of live cells reveal microdomain localization upon activation. *Journal of Cell Science*, 118:1799–1809, 2005.

[87] M. Dahan, S. Lvi, C. Luccardini, P. Rostaing, B. Riveau, and A. Triller. Diffusion dynamics of glycine receptors revealed by single-quantum dot tracking. *Science*, 302:442–445, 2003.

[88] P. M. Haggie, J. K. Kim, G. L. Lukacs, and A. S. Verkman. Tracking of quantum dot-labeled CFTR shows near immobilization by C-terminal PDZ interactions. *Molecular Biology of the Cell*, 17:4937–4945, 2006.

[89] W. J. Parak, R. Boudreau, M. Le Gros, D. Gerion, D. Zanchet, C. M. Micheel, S. C. Williams, A. P. Alivisatos, and C. Larabell. Cell motility and metastatic potential studies based on quantum dots imaging of phagokinetic tracks. *Advanced Materials*, 14:882–885, 2002.

[90] M. Dahan, T. Laurence, F. Pinaud, D. S. Chemla, A. P. Alivisatos, M. Sauer, and S. Weiss. Time-gated biological imaging by use of colloidal quantum dots. *Optic Letters*, 26:825–827, 2001.

[91] J. K. Jaiswal, H. Mattoussi, J. M. Mauro, and S. M. Simon. Long-term multiple color imaging of live cells using quantum dot bioconjugates. *Nature Biotechnology*, 21:47 – 51, 2003.

[92] S. Ju Cho, D. Maysinger, M. Jain, B. Roder, S. Hackbarth, and F. M. Winnik. Long-term exposure to CdTe quantum dots causes functional impairments in live cells. *Langmuir*, 23:1974–1980, 2007.

[93] M. E. Akerman, W. C. W. Chan, P. Laakkonen, S. N. Bhatia, and E. Ruoslahti. Nanocrystal targeting in vivo. *Proceedings of the National Academy of Science*, 99:12617–12621, 2002.

[94] W. W. Yu, L. Qu, W. Guo, and X. Peng. Experimental determination of the extinction coefficient of CdTe and CdSe and CdS nanocrystals. *Chemistry of Materials*, 15:2854–2860, 2003.

[95] A. T. R. Williams, S. A. Winfield, and J. N. Miller. Relative fluorescence quantum yields using a computer controlled luminescence spectrometer. *Analyst*, 108:1067 – 1071, 1983.

[96] D. Axelrod. Cell-substrate contacts illuminated by total internal reflection fluorescence. *The Journal of Cell Biology*, 89:141–145, 1981.

[97] M. Minsky. Microscopy apparatus, December 1961. U.S. Patent 301467.

[98] Y. Masumoto and K. Sonobe. Size-dependent energy levels of CdTe quantum dots. *Physical Review B*, 56:9734–9737, 1997.

[99] R. W. G. Wykoff. Crystal structures, vol. 1. *John Wiley and Sons N.Y.*, 1971.

[100] S.-H. Wei and A. Zunger. Valence band splittings and band offsets of AlN and GaN and InN. *Applied Physics Letters*, 69:2719–2721, 1996.

[101] X. Chen, Y. Lou, A. C. Samia, and C. Burda. Coherency strain effects on the optical response of core/shell heteronanostructures. *Nano Letters*, 3:799–803, 2003.

[102] Z. Yu, L. Guo, H. Du, T. Krauss, and J. Silcox. Shell distribution on colloidal CdSe/ZnS quantum dots. *Nano Letters*, 5:565–570, 2005.

[103] M. Yu, G. W. Fernando, R. Li, F. Papadimitrakopoulos, N. Shi, and R. Ramprasad. First principles study of CdSe quantum dots: Stability and surface unsaturations and experimental validation. *Applied Physics Letters*, 88:231910(1–3), 2006.

[104] O. Zakharov, A. Rubio, X. Blase, M. L. Cohen, and S. G. Louie. Quasiparticle band structures of six II-VI compounds: ZnS and ZnSe and ZnTe and CdS and CdSe and CdTe. *Physical Review B*, 50:10780 – 10787, 1994.

[105] C. D. Heyes, A. Yu. Kobitski, V. V. Breus, and G. U. Nienhaus. Effect of the shell on the blinking statistics of core-shell quantum dots: A single-particle fluorescence study. *Physical Review B*, 75:125431(1–8), 2007.

[106] X. Peng, J. Wickham, and A. P. Alivisatos. Kinetics of II-VI and III-V colloidal semiconductor nanocrystal growth: focusing of size distributions. *Journal the American Chemical Society*, 120:5343–5344, 1998.

[107] Y. Ebenstein, T. Mokari, and U. Banin. Fluorescence quantum yield of CdSe/ZnS nanocrystals investigated by correlated atomic-force and single-particle fluorescence microscopy. *Applied Physics Letters*, 80:4033–4035, 2002.

[108] J. Yao, D. R. Larson, H. D. Vishwasrao, W. R. Zipfel, and W. W. Webb. Blinking and nonradiant dark fraction of water-soluble quantum dots in aqueous solution. *Proceedings of the National Academy of Sciences*, 102:14284–14289, 2005.

[109] R. J. Owen, C. D. Heyes, D. Knebel, C. Röcker, and G. U. Nienhaus. An integrated instrumental setup for the combination of atomic force microscopy with optical spectroscopy. *Biopolymers*, 82:410–414, 2006.

[110] R. A. Marcus and N. Sutin. Electron transfer in chemistry and biology. *Biochimica et Biophysica Acta*, 811:265–322, 1985.

[111] M. Shim, S. V. Shilov, M. S. Braiman, and P. Guyot-Sionnest. Long-lived delocalized electron states in quantum dots: A step-scan fourier transform infrared study. *Journal of Physical Chemistry B*, 104:1494 –1496, 2000.

[112] G. Kalyuzhny and R. W. Murray. Ligand effects on optical properties of CdSe nanocrystals. *Journal of Physical Chemistry B*, 109:7012 –7021, 2005.

[113] M. Shim and P. Guyot-Sionnest. n-Type colloidal semiconductor nanocrystals. *Nature*, 407:981–983, 2000.

[114] M. Shim and P. Guyot-Sionnest. Intraband hole burning of colloidal quantum dots. *Physical Review B*, 64:245342(1–4), 2001.

[115] I. Chung and M. G. Bawendi. Relationship between single quantum-dot intermittency and fluorescence intensity decays from collections of dots. *Physical Review B*, 70:165304(1–5), 2004.

[116] P. Michler, A. Imamoglu, M. D. Mason, P. J. Carson, G. F. Strouse, and S. K. Buratto. Quantum correlation among photons from a single quantum dot at room temperature. *Nature*, 406:968–970, 2000.

[117] C. F. Landes, M. Braun, and M. A. El-Sayed. On the nanoparticle to molecular size transition: Fluorescence quenching studies. *Journal of Physical Chemistry B*, 105:10554–10558, 2001.

[118] R. Gill, R. Freeman, J.-P. Xu, I. Willner, S. Winograd, I. Shweky, and U. Banin. Probing biocatalytic transformations with CdSe-ZnS quantum dots. *Journal of the American Chemical Society*, 128:15376–15377, 2006.

[119] J. M. Walshe. The story of penicillamine: A difficult birth. *Movent Disorder*, 18:853–859, 2003.

[120] H. W. L. Ziegler-Heitbroc, E. Thiel, A. Futterer, V. Herzog, A. Wirtz, and G. Riethmuller. Establishment of a human cell line (Mono Mac 6) with characteristics of mature monocytes. *International Journal of Cancer*, 41:456–461, 1988.

Summary

Quantum dots are promising fluorescent tools for many applications in the life sciences. They are bright, easily tunable in color, and extremely stable against photobleaching. However, rendering these nanomaterials water-soluble and biocompatible, while maintaining their advantageous optical properties, small size and chemical stability, is not a trivial task.

The presented thesis is devoted to the design, synthesis, modification and characterization of different quantum dot preparations and to the optimization of their properties towards biocompatibility. Moreover, the fundamental principles of fluorescence intermittency and the quenching of quantum dot luminescence by various thiolated ligands were investigated and discussed.

The synthesis of semiconductor CdSe quantum dots was modified in order to increase reproducibility in their synthesis and obtain as high a photoluminescence efficiency as possible. The optical properties of the nanocrystals were further improved by overcoating with several monolayers of a ZnS shell, a wider-bandgap semiconductor. The capping reaction performed under established conditions [17] was studied and characterized by transmission electron microscopy, which revealed wurtzite lattice structures in both the core and the shell. It was found that the surfactant composition governs lattice type of the core. Quantum dots synthesized in oleylamine/oleic acid surfactant system instead of the traditionally used trioctylphosphine oxide and hexadecylamine surfactants grew with the zinc blende lattice structure. It was previously assumed that the shell lattice structure was controlled by the core lattice. However, results presented here show that the shell lattice structure is, rather, also controlled by the surfactant composition, irrespective of the core lattice. This thesis gives evidence that a zinc blende ZnS shell grows on a wurtzite CdSe core when using the oleylamine/oleic acid surfactant system for the shell growth. An amine-induced increase in the photoluminescence efficiency is observed for quantum dots stabilized by oleylamine, in agreement with earlier reports [17, 67].

Fluorescence intermittency of single quantum dots under constant illumination has attracted a great deal of attention from both experimentalists and theoreticians. Blinking of quantum dots may limit their applications in nanotechnology and the life sciences. In order to reduce this effect, it is important to more thoroughly understand its mechanism.

The fluorescence blinking statistics of different quantum dot preparations was studied using total internal reflection fluorescence microscopy (TIRFM). For each sample intensity traces from hundreds of quantum dots immobilized in a polymer matrix were measured. From the traces, the duration of *"on"*- and *"off"*- phases were extracted and the probability distributions were plotted. Interestingly, for all observed *"off"*- times, the probability distributions showed power-law behavior, whereas *"on"*- times displayed power-law behavior with an exponential cutoff tail at longer durations. These distribution behaviors were consistent with many earlier reports for the *"off"*- times [7, 44, 49, 50, 51], whereas the probability densities of the *"on"*- times have been more varied in the literature: some reported similar behavior to our quantum dots [7], while others reported only a power-law behavior of the *"on"*-times [8, 51]. To further investigate this mechanism and in order to determine the effect of shell on the fluorescence blinking of core/shell quantum dots, we also studied CdSe nanoparticles capped with 2.6, 3.5 and 7 monolayers of ZnS. Data analysis showed no significant effect of the shell thickness on the distributions of *"on"*- and *"off"*- times, suggesting that electron or hole tunneling through the shell is not a prevalent mechanism for blinking in core-shell quantum dots.

To explain our experimental findings we applied a theoretical model recently introduced by *Frantsuzov and Marcus* [57]. Unlike other interpretations [55, 56], this model does not involve external trap states, but rather hole trapping at surface states. After electronic excitation of the quantum dot, the hole can be trapped in a deep surface state of the CdSe core, transferring its excess energy to the excited electron, which is promoted from the $1S_e$ to the $1P_e$ state by an Auger mechanism. The $1S_e$-$1P_e$ gap is assumed to undergo light-induced stochastic fluctuations, so that it can be either in resonance or out of resonance with the energy gap between the hole states. This model explains the power-law behavior of the *"on"*- and *"off"*-times distribution, the exponential cutoff in the power-law dependence at long *"on"*-times and the lacking dependence of the shell thickness on the blinking statistics. Extending this model to the idea of a threshold number of trap states resulting in a dark quantum dot was used to show that the overall quantum yield of an ensemble is mainly governed by the fraction of non-emitting particles in the sample, thus relating the macroscopic observation of quantum yield to a microscopic mechanism.

Water-solubilization is a critical step towards the application of quantum dots in the life sciences. It has been shown that the choice of ligand for the functionalization determines the resulting optical properties [3, 59, 62, 69], photochemical stability [62, 64], colloidal stability [77] and even cytotoxicity [63]. Therefore, for the attainment of biocompatibility of quantum dots, certain key factors need to be established and compromised. Bifunctional thiolated molecules are among the most commonly used ligands to render quantum dots water-soluble. These ligands maintain a relatively small total size of the quantum dot, which is beneficial for many biological applications, but often cause a decrease in the photoluminescence

efficiency, with the extent of reduction varying significantly between different reports. We have investigated the quenching effect of various commonly-used thiolated ligands. A strong quenching effect related to the size and charge of the quenching molecule was observed. Nonlinear Stern-Volmer plots suggested multiple quenching pathways. We proposed that these pathways were related to the various functional groups. By comparing the quenching effects of the thiolated ligands with their non-thiolated analogues, the relative contributions of the thiol group, carboxyl group, and alcohol group to the quenching behavior were assessed. Furthermore, luminescence lifetime analysis revealed that the mechanism of the quenching was static rather than collisional, indicating that it arises from ligands coordinated to the quantum dot surface. Moreover, we observed that the chemical stability of MUA-coated quantum dots depended on their exposure to light, suggesting photocatalytic disulfide bridge formation, eventually resulting in quantum dot aggregation.

The limited solubility of MUA-coated quantum dots in aqueous solutions of pH below 8 – 9 resulted in the aggregation of quantum dots in solution. The negatively-charged MUA-functionalized quantum dots also resulted in high non-specific binding to cell membranes, considerably limiting experiments in which membrane components can be specifically labeled. We found that the use of *D*-penicillamine (DPA) for water-solubilization of quantum dots improved these properties. DPA contains a thiol group for complexing to the surface of quantum dot and both a carboxylic acid and an amine group and is thus zwitterionic at neutral pH. The overall neutrality of DPA-coated quantum dots resulted in low non-specific binding to both glass surfaces and cell membranes over the pH range of 5.0 – 9.2, which should provide improved opportunities to study cell membrane processes such as lipid domain dynamics, membrane-protein interactions and cell signaling.

Zusammenfassung

Quantenpunkte sind vielversprechende Werkzeuge für viele Fluoreszenz-Anwendungen in den Lebenswissenschaften. Sie sind stark fluoreszent, können in verschiedenen Farben hergestellt werden und sind extrem photostabil. Es ist jedoch nicht trivial, diese Nanomaterialien wasserlöslich und biokompatibel zu machen und gleichzeitig ihre vorteilhaften Eigenschaften, geringe Größe und chemische Stabilität, zu erhalten.

Diese Arbeit beschäftigt sich mit dem Design, der Synthese, Modifikation und Charakterisierung verschiedener Quantenpunkt-Präparationen und mit der Optimierung ihrer Eigenschaften in Bezug auf Biokompatibilität. Ferner werden die fundamentalen Prinzipien des Fluorezenzblinkens und der Fluoreszenzlöschung von Quantenpunkten durch verschiedene Thiol-Liganden untersucht und diskutiert.

Die Synthese von CdSe Halbleiter-Quantenpunkten wurde modifiziert, um die Reproduzierbarkeit bei der Synthese zu verbessern und um die Quantenausbeute der Photolumineszenz zu optimieren. Die optischen Eigenschaften der Nanokristalle wurden durch Überschichtung mit mehreren Monolagen aus ZnS, einem Halbleitermaterial mit größerer Bandlücke, weiter verbessert. Die unter etablierten Bedingungen [17] durchgeführte Beschichtung wurde mittels Transmissions-Elektronenmikroskopie charakterisiert und zeigte eine Wurtzit-Gitterstruktur sowohl für den Kern als auch für die Schale. Bisher wurde angenommen, dass die Gitterstruktur der Schale durch die Gitterstruktur des Kerns kontrolliert wird. Die hier beschriebenen Resultate zeigen jedoch, dass die Gitterstruktur der Schale, unabhängig von der Gitterstruktur des Kerns, auch durch die Tensidzusammensetzung kontrolliert wird. Quantenpunkte, die in Oleylamin/Oleinsäure synthetisiert wurden anstelle des traditionellen Tensidsystems Trioctylphosphinoxid/Hexadecylamin, wuchsen in der Zinkblende-Gitterstruktur. Diese Arbeit belegt, dass eine ZnS Schale in Zinkblende-Struktur auf einem Wurtzit CdS Kern wächst, wenn Oleylamin/Oleinsäure als Tensidsystem für das Schalenwachstum eingesetzt wird. Für oleylamin-stabilisierte Quantenpunkte wird, in Übereinstimmung mit früheren Arbeiten [17, 67], eine amininduzierte Erhöhung der Photolumineszenz-Quantenausbeute beobachtet.

Die zeitlichen Schwankungen des Fluoreszenzsignals einzelner Quantenpunkte bei konstanter Beleuchtung hat erhebliche Aufmerksamkeit bei Theoretikern und

Experimentalisten erregt. Das Blinken der Quantenpunkte schränkt ihre Einsetzbarkeit in der Nanotechnologie und den Lebenswissenschaften ein. Es ist daher wichtig, die Mechanismen dieses Effekts zu verstehen, um ihn reduzieren zu können.

Die Statistik des Fluoreszenzblinkens verschiedener Quantenpunkt-Präparationen wurde mittels Totalreflexions-Fluoreszenzmikroskopie (TIRFM) untersucht. Für jede Probe wurden Fluoreszenzsignale von einigen hundert in einer Polymermatrix immobilisierten Quantenpunkten aufgenommen. Aus dem Signalverlauf wurde jeweils die Dauer der "an" und "aus" Phasen bestimmt und in Form einer Wahrscheinlichkeitsverteilung aufgetragen. Interessanterweise ergab sich für die Wahrscheinlichkeitsverteilung der "aus"-Zeiten ein reines Potenzgesetz, während die Verteilung für die "an"-Zeiten ein Potenzgesetz mit einem exponentiellen Abfall für lange Zeitdauern zeigt. Dieses Verhalten ist konsistent mit vielen früheren Untersuchungen für die "aus"-Zeiten [7, 44, 49, 50, 51], während für die "an"-Zeiten sehr unterschiedliche Ergebnisse dokumentiert sind: Zum Teil entsprechen diese unseren Resultaten [7], teilweise wurde aber auch ein reines Potenzgesetz für die Wahrscheinlichkeitsverteilung der "aus"-Zeiten gefunden [8, 51]. Um den Mechanismus besser zu verstehen und um den Einfluß der Schale auf das Fluoreszenzblinken von Kern/Schale Quantenpunkten zu bestimmen, wurden auch CdSe Nanopartikel, die mit 2.6, 3.5 und 7 Monolayern ZnS überschichten waren, untersucht. Es zeigte sich kein signifikanter Einfluß der Schalendicke auf die Verteilungen der "an"- und "aus"- Zeiten, was nahe legt, dass Tunneln von Elektronen oder Löchern durch die Schale nicht der vorherrschende Mechanismus für das Blinken von Kern/Schale Quantenpunkten ist.

Zur Interpretation unserer Ergebnisse wurde ein Modell, welches kürzlich von Frantsuzov und Marcus [57] eingeführt wurde, verwendet. Im Gegensatz zu anderen Interpretationen [55, 56] enthält dieses Modell keine externen Rekombinationsstörstellen (Traps), stattdessen aber den Einfang von Löchern durch Oberflächenzustände. Nach der elektronischen Anregung des Quantenpunkts kann das Loch in einem tiefen Oberflächenzustand des CdSe-Kerns gefangen werden und seine überschüssige Energie auf das angeregte Elektron übertragen, welches dann durch einen Auger-Mechanismus vom $1S_e$ in den $1P_e$ Zustand angehoben wird. Es wird wird angenommen, dass die $1S_e$-$1P_e$ Energielücke lichtinduzierten stochastischen Fluktuationen ausgesetzt ist, sodass sie sowohl in Resonanz als auch aus der Resonanz mit der Energielücke zwischen den Lochzuständen sein kann. Dieses Modell erklärt das Potenzgesetz für die Verteilung der "an"- und "aus"-Zeiten, das exponentielle Abschneiden des Potenzgesetztes für lange "an"-Zeiten, sowie die nicht vorhandene Abhängigkeit der Blinkstatistik von der Schalendicke. Durch die Erweiterung dieses Modells um die Vorstellung, dass das Überschreiten einer Mindestanzahl von "Trap"-Zuständen zu einem dunklen Quantenpunkt führt, wurde gezeigt, dass die gesamte Quantenausbeute eines Ensembles wesentlich durch den Anteil nicht emittierender Partikel bestimmt ist. Somit wird eine Beziehung zwischen der makroskopisch beobachteten Quan-

tenausbeute und einem mikroskopischen Mechanismus hergestellt.

Die Solubilisierung von Quantenpunkten in Wasser ist ein wichtiger Schritt für deren Anwendbarkeit in den Lebenswissenschaften. Es wurde gezeigt, dass die Wahl des Liganden für die Funktionalisierung ausschlaggebend ist für die optischen Eigenschaften [3, 59, 62, 69], die photochemische Stabilität [62, 64], die kolloidale Stabilität [77] und sogar für die Zytotoxizität [63]. Für die Biokompatibilität von Quantenpunkten müssen deshalb bestimmte Schlüsselfaktoren berücksichtigt werden. Häufig werden bifunktionale Thiol-Moleküle als Liganden eingesetzt, um wasserlösliche Quantenpunkten herzustellen.Mit diesen Liganden kann die Ausdehnung der Quantenpunkte relativ klein gehalten werden, was für viele biologische Anwendungen wesentlich ist. Oft ist dies aber mit einer Verringerung der Photolumineszenz-Quantenausbeute verbunden, wobei das Ausmaß dieser Reduktion zwischen den verschiedenen Untersuchungen stark variiert. Wir haben den Effekt der Löschung durch verschiedene Thiol-Liganden, die häufig eingesetzt werden, untersucht. Es wurde ein starker Einfluß der Größe und der Ladung des Liganden auf die Löschung festgestellt. Nichtlinearitäten in der Stern-Vollmer Auftragung weisen auf die Existenz mehrerer Lösch-Mechanismen hin, die nach unsrer Ansicht mit den verschiedenen funktioneller Gruppen zusammenhängen. Durch den Vergleich der Löscheigenschaften von Thiol-Liganden mit ihren nicht-thiolerhaltigen Gegenstücken konnten die relativen Beiträge der Thiolgruppe, der Carboxylgruppe und der Alkoholgruppe zur Löschung zugeordnet werden. Ferner deuten Untersuchungen der Lumineszenzlebensdauer auf einen statischen Löschmechanismus, was darauf hinweist, dass die Löschung durch Liganden erfolgt, die an die Oberfläche der Quantenpunkte koordiniert sind. Weiterhin beobachteten wir, dass die chemische Stabilität von MUA-beschichteten Quantenpunkten von ihrer Belichtung abhängt, was eine photokatalytische Bildung von Disulfid-Brücken nahe legt, die zur Aggregation der Quantenpunkte führt.

Die begrenzte Löslichkeit MUA-beschichteter Quantenpunkte in wässriger Lösung unterhalb pH 8 – 9 führte zur Aggregation der Quantenpunkte in Lösung. Die negativ geladenen MUA-funktionalisierten Quantenpunkte zeigten auch eine starke unspezifische Bindung an Zellmembranen, was ihre Anwendbarkeit zur spezifischen Markierung von Membrankomponenten stark einschränkt. Wir zeigen, dass die Verwendung von *D*-Penicillamin (DPA) zur Solubilisierung von Quantenpunkten in Wasser diese Eigenschaften verbessert. DPA enthält neben der Thiolgruppe zur Komplexierung mit der Quantenpunkt-Oberfläche noch eine Carboxyl- sowie eine Aminogruppe und ist damit zwitterionisch bei neutralem pH. Dies bewirkte eine nur geringe unspezifische Bindung von DPA-beschichteten Quantenpunkten, sowohl an Glasoberflächen als auch an Zellmembranen im pH-Bereich von 5.0 bis 9.2. Somit eröffnen sich verbesserte Perspektiven für Untersuchungen der Dynamik von Lipiddomänen, Membran-Protein Wechselwirkung, zellulären Signaltransduktion und anderer Vorgänge an der Zellmembran.

Achievements

Publications

1. C. D. Heyes, A. Yu. Kobitski, V. V. Breus, and G. U. Nienhaus. Effect of the shell on the blinking statistics of core-shell quantum dots: A single-particle fluorescence study, *Phys. Rev. B*, 75:125431(1-8), 2007.

2. V. V. Breus, C. D. Heyes, and G. U. Nienhaus. Quenching of CdSe-ZnS core-shell quantum dot luminescence by water-soluble thiolated ligands *J. Phys Chem. C*, 111:18589-18594, 2007.

3. V. V. Breus, C. D. Heyes, K. Tron, and G. U. Nienhaus. Thiolated Zwitterionic Ligands for Water-Soluble Quantum Dots with Low Unspecific Binding, *Manuscript In Preparation,* 2008.

Posters

1. Frühjahrstagung Jahrestagung der Deutsche Physikalische Gesellschaft (DPG), March 08-12, 2004, Regensburg;

2. Jahrestagung der Deutschen Gesselschaft für Biophysik, September 12-15, 2004 Freiburg;

3. Trends in Nanoscience 2005, October 8-12, 2005, Kloster Irsee;

4. Jahrestagung der Deutschen Gesselschaft für Biophysik, September 24-27, 2006 Mainz;

5. Trends in Nanoscience 2007, February 24-28, 2007, Kloster Irsee;

Workshops

1. Common Workshop GRK 328 & SFP 569 October 12-14, 2003, Heinrich-Fabri-Institut, Blaubeuren;

2. Workshop GRK 328 & SFP 569 "Towards Molecular Electronics", November 26-27, 2004, Ulm.

Attended Lectures

1. Biophysik I and Biophysik II, 2003 – 2004;

2. SFB569 Colloquium.

Awards and Honors:

1. Posterpreis, Jahrestagung der Deutschen Gesellschaft für Biophysik, September 24-27, 2006 Mainz.

Curriculum Vitae

Vladimir V. Breus

Personal data

Born:	December 15, 1981
Place of Birth:	Kazan, Russian Federation
Nationality:	Russian
Marital status:	Single

Schooling

1988-1998	School Nr. 122, Kazan, Russian Federation

Education and Research

1998-2003	Department of Physical Chemistry, Kazan State University, Russian Federation.
1999-2002	Research Student in Laboratory of Supramolecular Chemistry, headed by Prof. V. V. Gorbatchuk.
2001-2002	Course Thesis (excellent).
2002-2003	Diploma in Chemistry (with Honors), Diploma Thesis: "Effects of Hydration, Lipids and Temperature on the Binding of the Volatile Aroma Terpenes by Dried β-Lactoglobulin".
2003-present	PhD student at the Institute of Biophysics, headed by Prof. G. U. Nienhaus, University of Ulm, Germany.

Acknowledgments

First of all, I would like to thank my supervisor Prof. G. U. Nienhaus, who gave me an opportunity to work at the Institute of Biophysics in Ulm. I am very grateful to him for introducing me into the challenging field of biophysics with its innovative research techniques and intradisciplinary approaches. I highly appreciate the biophysical knowledge and plentiful supply of helpful advice I obtained from him during my time as a PhD student.

I would like to gratefully acknowledge Dr. Colin D. Heyes, who shared with me a lot of his expertise and research insight, for bringing me into the fluorescent (yet still blinking) world of quantum dots. I thank Colin for teaching me the lost art of data analysis, for supporting and criticizing my ideas and for the enormous amount of helpful advice.

Many thanks to Dr. Carlheinz Röcker for all the guidance and help over these years.

I am indebted to Dr. Andrei Kobitski for providing a great deal of help with programming and for sharing his microscopy skills.

It is a pleasure to thank Dr. Kyrylo Tron for his supreme knowledge of cell biology and for help with the cell preparation.

A great thank you goes to Dr. Sergey Ivanchenko for many fruitful scientific discussions and useful advice.

I would also like to thank all current and previous members of the Institute of Biophysics, for creating a stimulating and very friendly environment.

I wish to also acknowledge Prof. Ute Kaiser and Dr. Zaoli Zhang for help with providing HRTEM characterizations of my quantum dots.

I thank my sister Katya for her help and support and my parents for developing my interest for science and for supporting me my whole life through.

On a different note, I wish to thank the coffee producers of Germany for keeping my mind focused all these years, the university food vending machines for saving me from starvation during a number of all-night measurement sessions, and over 1,300 German breweries (so many brands, so little time) for being there for me.

Finally, I would like to thank Lena, my fiancée, for her love and support.

Ulm, den 28.01.2008

Vladimir Breus